Summer 2018

Enhanced Coupling Strength Gratings for Outcouplers in Optical Waveguides

Ruo-Hua He
rhe@smu.edu

ENHANCED COUPLING STRENGTH GRATINGS FOR OUTCOUPLERS

IN OPTICAL WAVEGUIDES

Approved by:

Dr. Gary A. Evans, Professor

Dr. Jerome K. Butler, Professor

Dr. Ralph Johnson, Photon Sciences, Inc

Dr. Duncan MacFarlane, Professor

Dr. Johannes Tausch, Professor

ENHANCED COUPLING STRENGTH GRATINGS FOR OUTCOUPLERS IN OPTICAL WAVEGUIDES

A Dissertation Presented to the Graduate Faculty of

Lyle School of Engineering

Southern Methodist University

in

Partial Fulfillment of the Requirements

for the degree of

Doctor of Philosophy

with a

Major in Electrical Engineering

by

Ruo-Hua He

(B.S., Tunghai University, Taichung, Taiwan)

(M.S., Southern Methodist University, Dallas, Texas)

August 7, 2018

He, Ruo-Hua B.S., Tunghai University, Taichung, Taiwan
M.S., Southern Methodist University, Dallas, Texas

Enhanced Coupling Strength Gratings for Outcouplers in Optical Waveguides

Advisor: Dr. Gary A. Evans

Doctor of Philosophy conferred August 7, 2018

Dissertation completed May 11, 2018

Gratings used for silicon photonic waveguides were demonstrated with outcoupling efficiency greater than 60% in a short grating length of 13 μm at a wavelength of 1550 nm. Due to problems of generating light from silicon, light has to be generated by either growing III-V material, wafer bonding III-V material to silicon, or externally generated light has to be coupled into and out of silicon photonic waveguides. Gratings have been used in semiconductor lasers to obtain single frequency operation. Some applications such as telecommunications require a narrow and single spectral line. And such single frequency lasers are typically distributed Bragg reflector (DBR) lasers or distributed feedback (DFB) lasers. Gratings used for both DBR and DFB lasers in III-V materials are generally hundreds of micrometers long due to a low index contrast at the grating interface, a low grating confinement factor, or a low value of the electric field at the grating interface. If the short gratings demonstrated in silicon photonic waveguides could be obtained in III-V semiconductor waveguides, lasers could incorporate such short gratings to couple light into silicon photonic circuits.

Addition of a thin, low-index liner layer over a surface grating combined with a high-index layer can result in short, efficient couplers for III-V waveguides with

performance similar to grating couplers in silicon photonic waveguides. The same low-index liner and high index cover layer can also minimize reflections at transitions between sections of photonic integrated circuits or between a laser region and a DBR or grating coupler region. A detailed design of an enhanced coupling strength (ECS) grating integrated with a 9-QW and 5-QW laser structure emitting at a wavelength near 1550 nm has been presented. Both designs allow outcoupling of greater than 70% of the emitted light in a distance of about 20 μm in a single pass, which is a reduction of outcoupler grating length in such III-V waveguides by a factor of 50 or more compared to conventional grating outcouplers. Moreover, the ECS approach also allows designing a second-order grating that has near 100% reflection with insignificant outcoupling. Such a grating can provide equivalent performance at twice the grating period as a first order DBR grating, allowing the holographic fabrication of low-loss reflective gratings to laser wavelengths below 400 nm from the previous limit of about 800 nm.

TABLE OF CONTENTS

LIST OF FIGURES

LIST OF TABLES

LIST OF ABBREVIATIONS AND SYMBOLS

E	Electric field
g_{th}	Threshold gain
G_{mat}	Material gain
k_0	Wave number in free space
K	Grating wave number
n	Index of refraction
n_{eff}	Effective index
R	Reflectivity
α	Attenuation coefficient
β	Longitudinal propagation constant
α_{int}	Internal loss
α_m	Modal loss
ε_o	Permittivity in free space
ε_{rel}	Relative permittivity
Γ	Confinement factor
λ_0	Wavelength in free space

Λ	Grating period
Λ_B	Grating period at Bragg condition
ω	Angular wavelength
a-Si	Amorphous silicon
BA	Broad area
DBR	Distributed Bragg reflector grating
DFB	Distributed feedback laser
DR	Distributed reflector
EAM	Electroabsorption modulator
ECS	Enhanced coupling strength grating
FDTD	Finite-difference time-domain
FP	Fabry-Perot
FreD	Frequency doubled lasers
HR	High reflection
LASER	Light amplification by stimulated emission of radiation
LED	Light-emitting diode
LI	Light-current
LR	Low reflection
IV	Current-voltage
ICP	Inductively coupled plasma
OC	Outcoupler
QW	Quantum well

RIE	Reactive ion etch
RG	Ridge guide
SCH	Separate confinement heterostructure
SEM	Scanning electron microscope
Si_3N_4	Silicon nitride
SiO_2	Silicon dioxide
TIR	Total internal reflection
VCSEL	Vertical cavity surface emitting laser
WZI	Imaginary part of effective index
WZR	Real part of effective index

ACKNOWLEDGEMENT

It has been a period of intense journey for me, not only in the scientific field, but also on a personal level. This dissertation would never be completed without many assistances, and I would like to reflect on the people who have supported and helped me so much throughout this period.

First and foremost, I would like to express my deepest gratitude and appreciation to my advisor Dr. Gray A. Evans for his guidance, inspiration feedback and gracious support throughout my study and work. I am also grateful to SMU lab manager Jay B. Kirk for his patient guidance on fabrication of semiconductor lasers and gratings in SMU cleanroom. I would like to thank Dr. Jerome K. Butler for introducing the grating theory and guiding his Floquet-Bloch grating software to me and Dr. Nai-Hsiang Sun for numerous discussions on grating simulations.

The further thank goes to Freddie Castillo for providing numerous help in fabrication processing and characterization in Photodigm Inc. I am thankful to Duy Phan and Lan Nguyen from Photodigm Inc. for depositing silicon nitride on wafers and technical discussions on laser and grating fabrication. I would like to thank Scott McWilliams for editing and polishing my dissertation. Special thanks to Kent Liu, Jin Huang, Reyhane Oztekin and Maryam Dezfuli for their assistance in my graduate study. I would also like

to thank Min-Heng Hsieh and my sister Ruo-Tsz He for their encouragement and mental support.

I am also grateful to my dissertation committee members: Dr. Gray A. Evans, Dr. Jerome K. Butler, Dr. Ralph Johnson, Dr. Johannes Tausch and Dr. Duncan MacFarlane for their discussions and invaluable feedback.

The work in this dissertation was supported in part by DARPA under Agreements HR0011-08-09-0001, in part by NASA contract NNX16CA20P, and in part by the National Science Foundation grant 66531000.

Chapter 1

INTRODUCTION

In this dissertation, a new method to enhance the performance of a grating outcoupler embedded in a semiconductor laser waveguide is developed. A complete design of such a device at silicon photonics wavelengths near 1550 nm is provided. By inserting a thin low-index liner layer between the conventional grating and a high-index cover layer, grating efficiency is dramatically increased. This "Enhanced Coupling Strength" (ECS) approach allows an outcoupler grating in compound semiconductor waveguides to radiate about 80% of the incident waveguide light in a distance of about 10 μm, compared to distances of many hundreds or thousands of μm [1] previously required for conventional outcoupler gratings in compound semiconductor waveguides. The ECS process has the additional advantage of providing higher optical field overlaps that result in smaller losses in the transition regions between active, passive and grating waveguide regions.

This chapter discusses some important concepts related to semiconductor materials, lasers, and gratings, and the relevance of ECS gratings to silicon photonics and DBR lasers.

1.1. Laser Waveguides

1.1.1. Semiconductor Materials

Semiconductor light-emitting diodes (LEDs) and semiconductor lasers, which efficiently convert electrical power to optical power, are made from III-V compounds, such as alloys of GaAs and InP or from II-VI compounds. The numbers III-V and II-VI refer to columns of the periodic table. The choice of semiconductor materials used to make laser devices depends on the desired wavelength (or equivalently, frequency) of emitted light. The wavelength is determined primarily by the band gap energy (E_g) of the active region material. The band gap is an intrinsic property of materials which is defined as the difference between the lowest level of the conduction band and the highest level of the valence band. For direct bandgap semiconductors, an electron in the conduction band can combine with a hole in the valence band and emit a photon with an energy that is approximately equal to the band gap energy. Therefore, the wavelength and frequency *f* of the photon is related to the bandgap by

$$E_g = E_{photon} = \mathrm{h}f = \frac{hc}{\lambda} \tag{1}$$

where *h* is Planck constant and *c* is the speed of light in vacuum, so the wavelength of light is given by

$$\lambda = \frac{hc}{E_g} \tag{2}$$

If the energy has units of electron volts (eV), the wavelength of light in μm is given by

$$\lambda\ (\mu m) \simeq \frac{1.24}{E_g\ (eV)} \tag{3}$$

The original motivation for this work was to couple an optical gain region with a "short" (10 to 20 μm long) grating outcoupler monolithically integrated with an InGaAsP/InP laser into a second grating outcoupler of similar length located on a silicon photonics optical waveguide as shown in Figure 1. The InGaAsP/InP material contains another distributed Bragg reflector (DBR) grating that reflects light in-plane (no outcoupling). The DBR grating serves as one mirror of a laser cavity. The second mirror of the laser cavity, located in the silicon photonics waveguide, provides the second mirror.

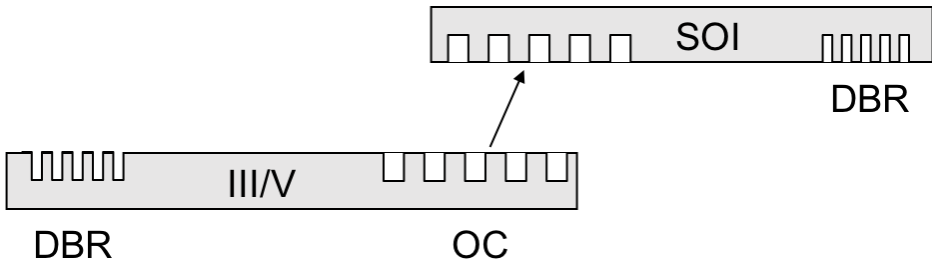

Figure 1. III-V Si hybrid laser structure.

Conventional grating outcouplers in silicon photonic waveguides that consist of a thin (0.2 to 0.4 μm) silicon core surrounded by silicon dioxide cladding layers first demonstrated high efficiency (> 80% total light outcoupled) coupling distances of only 10 to 20 μm [2]. Unlike direct bandgap light emitting semiconductor materials (many III-V and II-VI compounds), silicon has an indirect band gap, so electrons and holes cannot recombine radiatively to efficiently produce light. The integrated laser and ECS outcoupler is one method to couple light into silicon photonic waveguides.

Several InGaAsP/InP epitaxial structures that emit in the 1.2 to 1.7 μm wavelength range are shown in detail in chapter 3. In addition to the "hybrid" InGaAsP/InP – Si

photonics laser configuration, a complete laser (using two DBR gratings) can be integrated with an ECS outcoupler to make a surface emitting semiconductor laser. Although vertical cavity surface emitting lasers (VCSELs) are made in high volume for applications including data telecom and more recently facial and gesture recognition in smart phones and for virtual reality, they are limited to lower powers and near infrared wavelengths (less than about 1.1 μm), where silicon has high optical losses [3], [4]. An integrated laser with ECS outcoupler can provide very high power levels with wavelengths ranging from 0.36 μm (blue lasers in GaN) to beyond 10 μm (quantum cascade and interband cascade lasers) [5]- [8].

For silicon photonics waveguides, the wavelength of the propagating light must be greater than about 940 nm to avoid strong band to band absorption. Common wavelengths used in silicon photonics are about 1310 nm and 1550 nm because of the extensive development of photonic components at these telecom wavelengths. The semiconductor material used in the laser active region for this work is InGaAsP to obtain a wavelength of 1.55 μm in this research. The wavelength of $In_{1-x}Ga_xAs_yP_{1-y}$ is variable from 1.1 to 2 (InGaAs with strain) μm by adjusting the mole fraction of x and y. As indicated in Figure 2, the wavelength of a material is a function of composition and lattice constant. The lattice constant is the crystal dimension of a unit cell of the crystalline material, so each material has its own lattice constant. Matching lattice constants of two materials is important for the quality of heterostructure lasers (as discussed in section 1.1.3) to decrease crystal lattice defects. The combination of $In_{1-x}Ga_xAs_yP_{1-y}$ and InP can be lattice-matched at the lattice constant of the InP substrate (5.87 angstroms) as shown in Figure 2. Therefore, In_{1-}

$_xGa_xAs_yP_{1-y}$ layers grown on an InP substrate make up the laser and main waveguide structures considered for the grating outcouplers in this thesis.

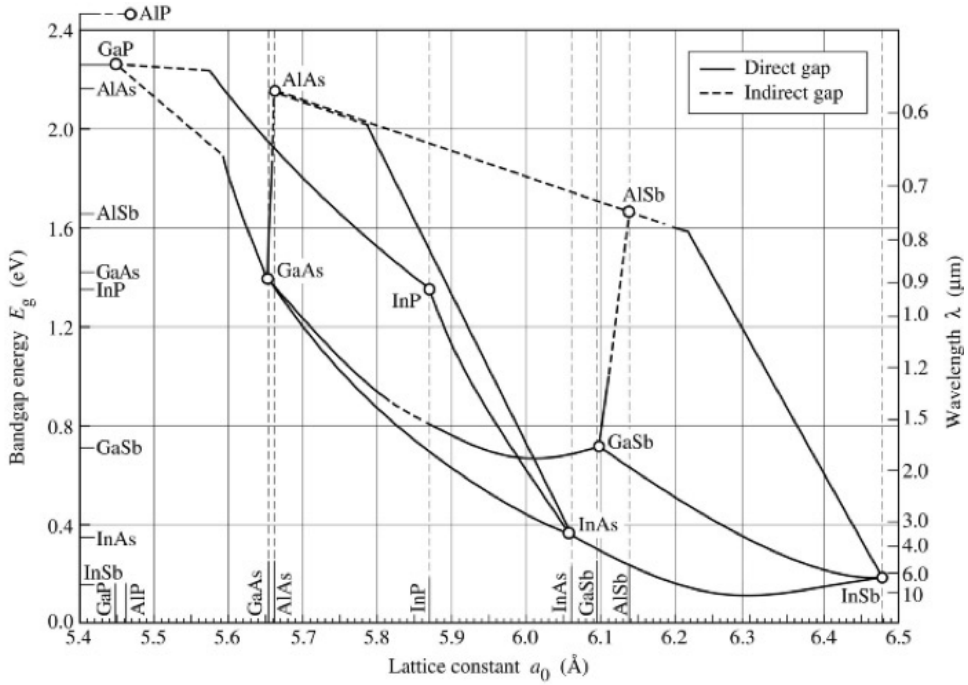

Figure 2. Band gap and lattice constant for semiconductor compounds [9].

1.1.2. Laser Components

Semiconductor lasers generate ultraviolet, visible and infrared light with a narrow wavelength spectrum depending on the chosen material system. The word laser is an acronym for Light Amplification by Stimulated Emission of Radiation. Although lasers require an amplifying region, they are also light oscillators, and all oscillators require both an amplifier and feedback. In a semiconductor laser [10], [11]: the amplifier is a region with an inverted (compared to equilibrium) population of electrons, allowing stimulated

radiation. The feedback is provided by discrete mirrors (cleaved facets of the semiconductor laser in horizontal cavity lasers) or distributed mirrors (such as a grating).

The light amplifying gain medium is made of semiconductor materials with a direct band gap as discussed in the previous section. The population inversion that results in gain occurs by optical pumping or, more commonly in semiconductor lasers, current injection.

At low current levels in a semiconductor laser, electrons flow into the conduction band on the n-side and holes flow into the valence band on the p-side. In the narrow bandgap active region, electrons in the conduction band recombine with holes in the valence band and emit photons. Such recombination of an electron and hole is called "spontaneous emission". Spontaneous emission, which is emitted by LEDs, produces photons with a relatively broad wavelength spectrum propagating in random directions (incoherent light). An electron and hole can also recombine and emit a photon by stimulated emission. In this case the emitted photon has exactly the same wavelength, phase and direction of propagation as that of the photon that stimulated the emission. This stimulated emission process produces highly coherent light.

Stimulated and spontaneous emission equals the absorption of light at equilibrium, which led Einstein to derive the well-known A and B coefficients [12]. For a material to become transparent, the injected laser current (called the transparency current) has result in the difference between the quasi Fermi levels of the conduction band (E_{fc}) and the valence band (E_{fv}) being equal to the bandgap [13]. With increasing current, the material has net gain. The number of photons emitted increase (or are amplified) with increasing current.

$$E_{fc} - E_{fv} > E_g \tag{4}$$

In a simple semiconductor laser, two mirrors, typically cleaved facets of the crystal, reflect photons back and forth along the axis of the gain medium, forming a Fabry Perot cavity. If the facets are cleaved with no coatings, equal power is emitted from both ends. The reflectivity of each mirror can be changed by applying high reflection (HR) coating or a low reflection (LR) coating on the mirrors. Using an HR and LR coating allows most of the photons to be emitted from one end of the laser. If the round trip power gain in the cavity is equal to the internal losses plus the loss of photons out of the end mirrors (mirror losses), the amount of gain g_{th} required for lasing is obtained.

$$g_{th} = \Gamma_{active} G_{mat} = \alpha_{int} + \frac{1}{2L} ln \frac{1}{R_1 R_2} \quad (5)$$

Above threshold, the round trip gain is "pinned," and each additional electron injected into the semiconductor results in generation of a photon emitted by stimulated emission if the internal quantum efficiency is 100%. As a result, a linear increase in current provides a linear increase in the output power of the laser [11], [14], [15]. In materials such as alloys of GaAs and InP, internal quantum efficiencies of 80 to 90% and higher are obtained, making semiconductor lasers the most efficient way to convert electrical power to optical power. The mirror power loss is due to the reflectivity of the two mirror facets (R_1 and R_2) and the cavity length is L. The internal loss (α_{int}) is related to band to band absorption, layer interface roughness, slight material composition inhomogeneity (variation), layer thickness variations, and doping. Γ_{active} the confinement factor in the active region is the fraction of the mode power in the active region. It is equal to the quantum well (QW) confinement factor for a quantum well laser. G_{mat} represents the material gain—the gain of the bulk material or the quantum well material as appropriate.

1.1.3. Heterostructure Waveguide

The first laser diodes demonstrated in 1962 [11] were homojunction devices, composed of two identical semiconductor materials with the same band gap energy but different doping types. To increase the optical gain and confine the photons, a heterostructure waveguide was introduced that consists of an active region (Figure 3) with a low-energy band gap sandwiched by two cladding layers that have a relatively high-energy band gap as illustrated in Figure 4. The typical thickness of early active regions was hundreds of nanometers. The difference in energy band gap between the active and cladding layers confine electrons in the conduction band and holes in the valence band to the active layer, increasing the gain of the active layer for a fixed current.

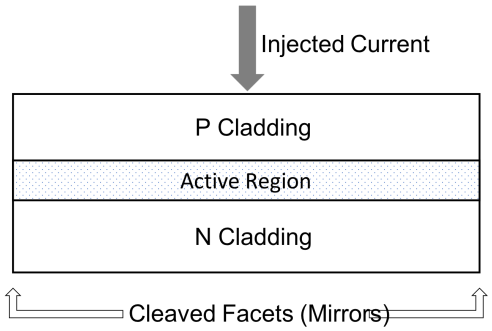

Figure 3. A semiconductor laser illustration with the narrow active region in the cavity.

Moreover, the low energy band gap corresponds to a higher index of refraction of the active region, while the high energy band gap has a lower index of refraction, resulting in the index profile shown in Figure 4. The difference in the refractive index between the active and cladding layer provides total internal reflection (TIR) so that light is confined to

the vicinity of the active layer. The fraction of light confined to the gain region is the confinement factor Γ_{active} in Equation (5).

The double heterojunction laser provides both carrier confinement and optical confinement, an advancement that allowed continuous operation of semiconductor lasers when the active layer thickness was reduced to about 100 nm [16].

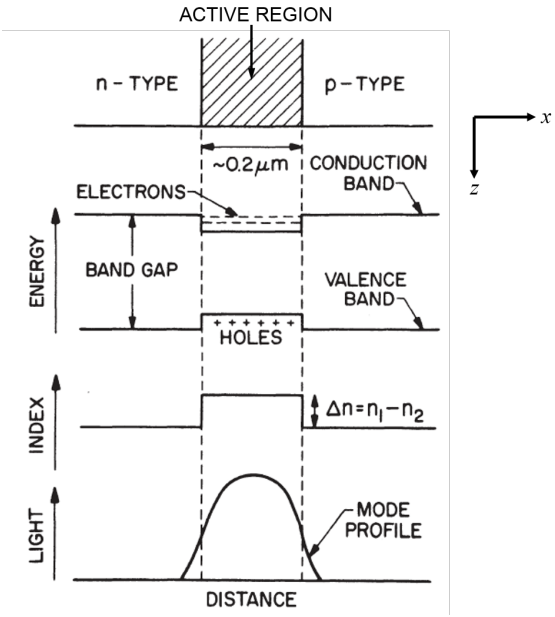

Figure 4. Sketch of a double-heterostructure, corresponding energy band diagram (to provide carrier confinement), index profile (to provide optical confinement), and electric field profile [11].

1.1.4. Types of Semiconductor Lasers and Characteristics

Once the epitaxial layers are designed and the laser wafer is grown, Broad-Area (BA) lasers and Ridge-Guide (RG) lasers can be fabricated and the devices can be tested. The highly doped, low bandgap InGaAs cap layer of a BA laser is etched to limit the current through a 100 μm wide contact stripe. Ti/Pt/Au is then deposited on the top of the laser stripe and the substrate is thinned to about 100 μm (for ease of cleaving facets) for a

Ni/Au/Ge contact. RG lasers have a deeply etched narrow ridge stripe, typically in the range of 2 to 5 μm, to provide lateral mode control. Both the high doped InGaAs layer and the InP cladding layer are etched to provide the lateral index difference between the laser ridge and the region outside the ridge area as shown in Figure 6.

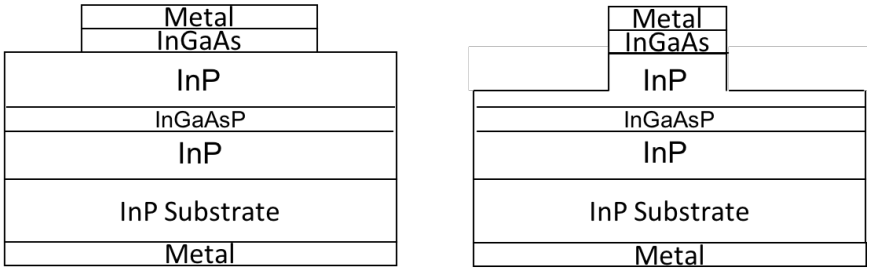

Figure 5. Sketch for (a) BA laser and (b) RG laser.

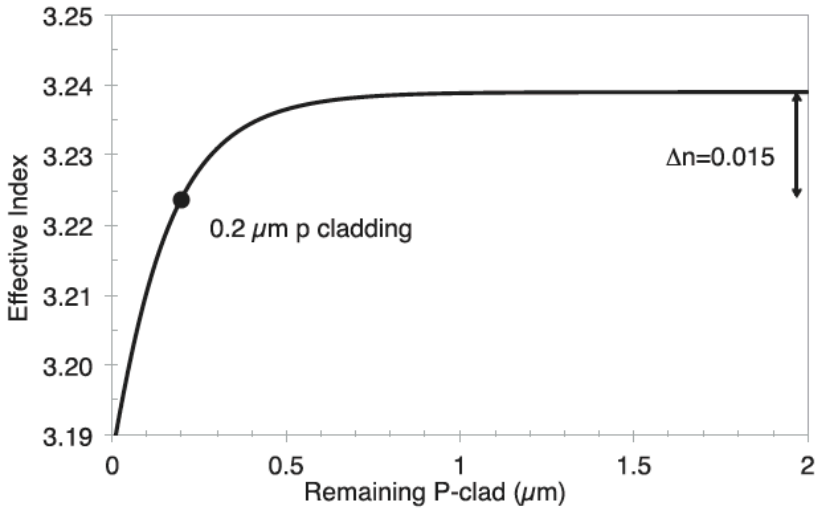

Figure 6. Effective index as a function of remaining p cladding thickness.

The Light-current (LI) curve is an important characteristic of a laser. Figure 7 shows a typical optical output power of light as a function of the external current. Threshold current I_{th} is defined to be the current at which there is a rapid increase in output power due

to stimulated emission. Below threshold, the optical power is dominated by spontaneous emission.

Longer and wider lasers require more external current to operate in the stimulated emission, so it is meaningless to just compare threshold current of different semiconductor lasers. Threshold current density, the threshold current divided by the area of the laser stripe, is an important metric used to compare different laser designs. In analyzing the threshold current density of laser diodes, it is essential to know the actual area where the injected current is applied. RG lasers have a narrow stripe (2-5 μm) covered by a metal contact. When applying the external current through a RG laser, the lateral current spreads, causing the injected-current area in the active region to be much larger than the actual metal stripe area, making it difficult to determine accurately the threshold current density of RG lasers. By contrast, BA lasers have a much wider cavity stripe, on the order of 100 μm or more, so the pumped current area is almost the same as the area of the metal stripe. As a result, BA lasers are good for determining accurate threshold current densities, transparency current densities, internal losses, and internal efficiencies.

The slope of the LI curve above the threshold is also an important characteristics of a laser. LI curves are temperature dependent. A higher operating temperature increases the threshold current density, reduces the slope efficiency, and shifts the lasing wavelength peak. As indicated in Figure 7, power rollover can occur at higher currents, typically due to heating effects.

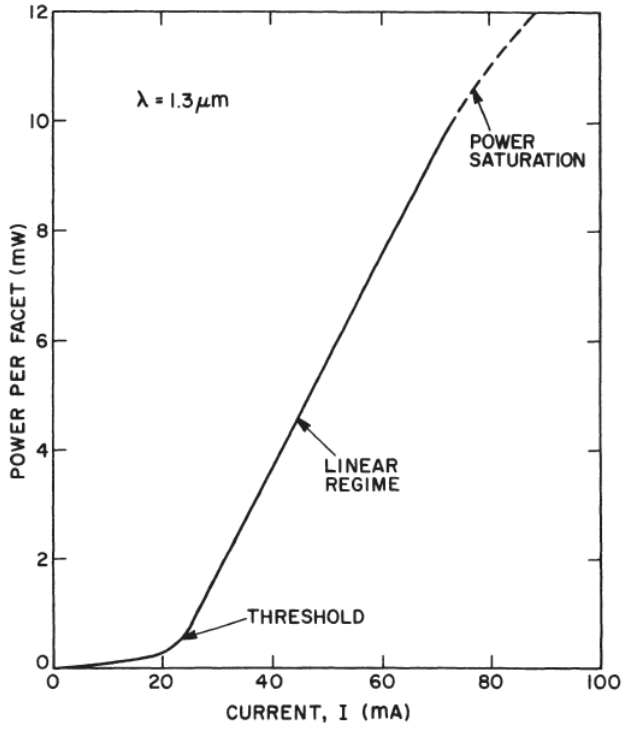

Figure 7. Light-current (LI) curve for InGaAsP laser [11].

Another characteristics of a laser is the optical power spectrum [17]. Many semiconductor laser applications require a well-defined narrow spectral bandwidth of light. As discussed in section 1.1.2, FP lasers have longitudinal modes. The multiple longitudinal modes cause multiple spectral peaks around a central peak. Below threshold, the spontaneous emission determines the shape of the spectral pattern with multiple peaks in the wide bandwidth. For ridge-guide and other laser structures with lateral mode confinement, the output powers of the longitudinal modes closest to the highest gain increases, reducing the number of longitudinal modes. Even in the rare cases where there is only one longitudinal mode in continuous operation, numerous longitudinal modes occur when the laser is modulated. Further, such lasers switch longitudinal modes rapidly with

changes in current. The power spectrum of BA lasers have numerous longitudinal and transverse modes with a relatively wide spectral width.

1.2. Gratings

To obtain dynamically single mode (also known as single frequency) operation, one or both of the cleaved-facet mirrors of a single transverse mode laser can be replaced with a grating. Depending on the period, the gratings with shorter periods can provide a spectrally narrow reflectivity, which can select a single longitudinal mode that is locked in over a wide operating range of currents and temperature. At longer periods, gratings can be used to couple light out of the laser waveguide.

Gratings are composed of a periodic variation of a layer thickness that can be modeled as an equivalent layer with a periodic refractive index. The shape of the layer variation usually has a sinusoidal or square profile – at least these are the profiles most commonly analyzed. An array of index discontinuities along the direction of the light propagation (the z direction in Figure 8) provides the constructive interference that is known as Bragg deflection or Bragg diffraction. As the guided light propagates in the grating structure having a fixed grating period Λ, only light at a certain wavelength is deflected at a fixed angle. If the angle indicated in Figure 8 is -90°, the light is reflected by the grating in the 1st order of Bragg diffraction. The grating period of 1st order Bragg diffraction is half of the wavelength of the light in the waveguide:

$$\Lambda_{1st} = \frac{\lambda_m}{2} = \frac{\lambda_0}{2n_{eff}} \tag{6}$$

where Λ is the grating period, λ_m is the wavelength of light traveling in materials, λ_0 is the wavelength of light propagating in free space, and n_{eff} is the effective index of the waveguide. Gratings operating in 1st order are used for in-plane reflection and transmission (parallel to the direction of propagation in the waveguide). The reflected and transmitted intensities of a grating of length L, derived from Couple Mode Theory, are [18], [19]

$$R = \frac{|\kappa L|^2}{\left(\frac{\Delta\beta L}{2}\right)^2 + (sL)^2 coth^2(sL)} \tag{7}$$

$$T = \frac{\gamma}{\gamma \cosh(\gamma L) - (\alpha - j\Delta\beta) sinh(\gamma L)} \tag{8}$$

where

$$s = \left[|\kappa|^2 - \left(\frac{\Delta\beta}{2}\right)^2\right]^{1/2} \tag{9}$$

$$\gamma = [\chi^2 + (\alpha - j\Delta\beta)^2]^{1/2} \tag{10}$$

$$\Delta\beta = 2(\beta - \beta_0) \tag{11}$$

Gratings operating in 2nd order Bragg diffraction not only reflect light, but also couple light out of the waveguide, both upwards (towards the superstrate) and downwards (towards the substrate). The grating period of the 2nd order Bragg diffraction is equal to the wavelength in the waveguide

$$\Lambda_{2nd} = \lambda_m = \frac{\lambda_0}{n_{eff}} \tag{12}$$

By measuring the wavelength of the emitted light from a laser cavity and by calculating the effective index of the optical mode in the waveguide, we can calculate the grating period for any order [14].

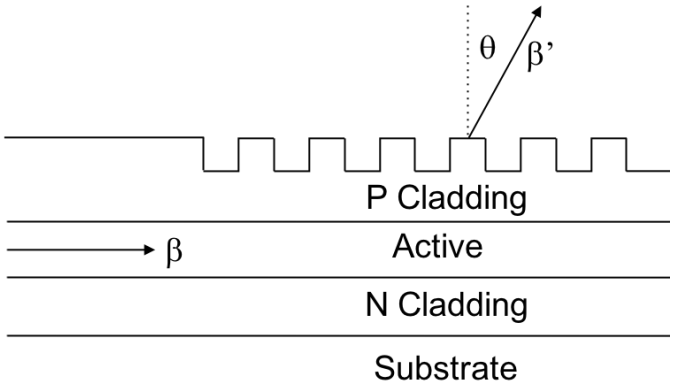

Figure 8. A schematic illustration of a waveguide with a grating structure to deflect light at an angle.

The angle of the output beam from a grating can be written as: [14]

$$\sin^2\theta = n_{eff}^2 - 2n_{eff}\left(\frac{\lambda_0}{\Lambda}\right) + (\frac{\lambda_0}{\Lambda})^2 \qquad (13)$$

1.2.1. Effectiveness of a Grating

1.2.1.1 First-order Grating Coupling Coefficient by an Integral Method

In general, optical waveguides can support multiple modes, even though most laser structures are designed to support only a single mode. A grating wavevector K ($K=2\pi/\Lambda$, where Λ is the grating period) can couple any forward mode (mode *p*) to any backward mode (mode *q*) in the case of contra-directional coupling, or any forward mode to any other forward mode in the case of co-directional coupling [20]. For grating reflectors and outcouplers, we are interested in contra-directional coupling as shown in Figure 9.

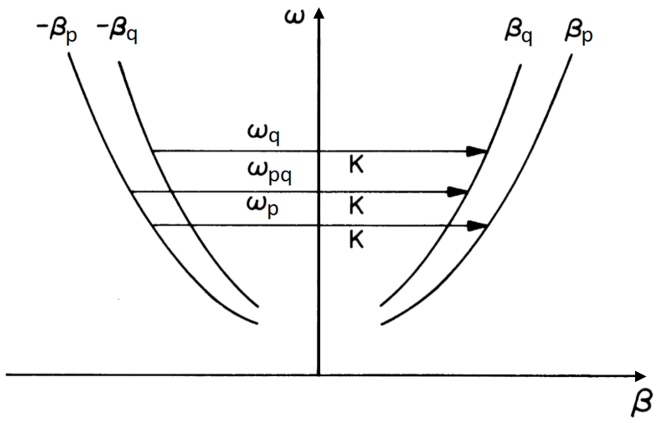

Figure 9. ω-β diagram illustrates self-coupling [20].

Equation (14) shows a perturbation formula for the first-order coupling strength k_{pq} between a *p* mode and a *q* mode of a grating formed in an optical waveguide [15], [21], [18]:

$$\kappa_{pq} = \frac{\omega\varepsilon_0}{4} b_m (n_1^2 - n_2^2) \cdot \int_{-a}^{0} E_p^*(x) E_q(x) dx \qquad (14)$$

where ω is the angular frequency of an optical mode, ε_0 is the permittivity of free space, b_m is the Fourier coefficient corresponding to the 1st order of the grating period, n_1 is the index of refraction of the core layer directly under the grating, n_2 is the index of refraction of the layer directly above the grating, *a* is the depth of the grating. The integral form in equation (14) is the fraction of light confined in the grating region that is also known as the grating confinement factor. The term of $(n_1^2 - n_2^2)$ is the relative permittivity difference since the relative permittivity ε_{rel} is equal to the square of the refractive index n^2. The coupling strength of a grating increases as the relative permittivity difference between the layer below and the layer above the grating increases. Furthermore, the strength of the grating increases as the fraction of light confined in the grating region increases according

to the integral term of equation (14). Although equation (14) applies only to first-order Bragg gratings, it indicates that for grating of all orders, increasing the permittivity difference and the grating confinement factor increases the strength of the grating.

1.2.1.2 First-Order Grating Coupling Coefficient by an Equivalent Surface Current Method

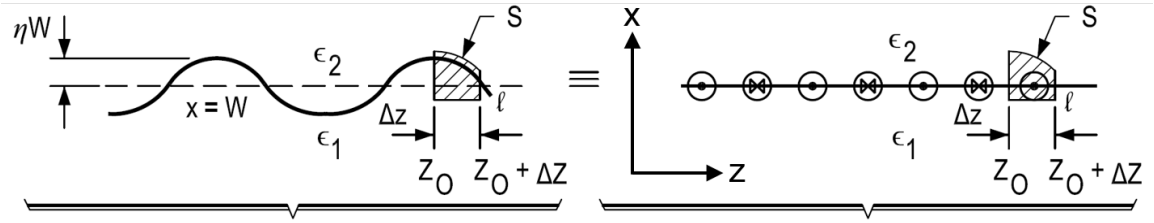

(a) (b)

Figure 10. Illustration of (a) a periodic sinusoidal boundary and (b) an equivalent planar boundary with a periodic surface current between two materials.

Another method to determine the coupling coefficient of a first order grating assumes that a periodic boundary is equivalent to a flat boundary with a periodic surface current, as shown in Figure 8. The sinusoidal boundary in Figure 10(a), between two materials with relative permitivites ε_1 on the lower side of the grating and ε_2 on the higher side of the grating can be written as

$$W_b(x) = W(1 + \eta cosKz) \tag{15}$$

where W is the thickness of the core layer, ηW is the amplitude of the periodic boundary, z is the spatial coordinate along with the axis of the optical waveguide and the propagation direction of the optical mode, and K is the grating wave number ($K = 2\pi/\Lambda$). This periodic

sinusoidal boundary is equivalent to the configuration consisting of an unperturbed boundary with a periodic surface current as shown in Figure 10(b).

From Maxwell's equations,

$$\nabla \times \vec{H} = \frac{\partial \vec{D}}{\partial t} + \vec{J} = \varepsilon_0 \varepsilon_{rel} \frac{\partial \vec{E}}{\partial t} + \vec{J} = j\omega \varepsilon_0 \varepsilon_{rel} \vec{E} + \vec{J} \tag{16}$$

where ε_0 is the permittivity in free space, ε_{rel} is the relative permittivity in materials, ω is the angular frequency of the electromagnetic field, J is the current, and E is the electric field. By Stokes Theorem,

$$\int_s (\nabla \times \vec{H}) d\vec{s} = \oint_l \vec{H} d\vec{l} \tag{17}$$

Substituting equation (17) into equation (16), we obtain

$$\oint_l \vec{H} d\vec{l} = j\omega \varepsilon_0 \varepsilon_{rel} \int_s \vec{E} d\vec{s} + \int_s \vec{J} d\vec{s} \tag{18}$$

As applying to Figure 10(a), there is the open surface S in the material of ε_1 without any current. Then equation (18) can be written as

$$\oint_l \vec{H} d\vec{l} = j\omega \varepsilon_0 \varepsilon_1 \int_s \vec{E} d\vec{s} \tag{19}$$

In addition, as applying to Figure 10(b), the open surface S is in the material of ε_2 with a surface current J_s.

$$\oint_l \vec{H} d\vec{l} = j\omega \varepsilon_0 \varepsilon_2 \int_s \vec{E} d\vec{s} + \int_s J_s(z) \delta(x - W) \widehat{e_y} d\vec{s} \tag{20}$$

where J_s is

$$\overrightarrow{J_s} = J_s(z) \delta(x - W) \widehat{e_y} \tag{21}$$

Since the periodic sinusoidal boundary between ε_1 and ε_2 in Figure 10(a) is equivalent to the unperturbed boundary between ε_1 and ε_2 with the surface current J_s in Figure 10(b), equation (19) is equal to equation (20) so we obtain

$$J_s(z)\Delta z = j\omega\varepsilon_0(\epsilon_2 - \epsilon_1)\int_s \vec{E}d\vec{s} \tag{22}$$

The integral part in equation (22) can be approximated as

$$\int_s \vec{E}d\vec{s} \approx E(W,z)\Delta x\Delta z \approx E(W,z)[\eta W cos(Kz)]\Delta z \tag{23}$$

where E(W, z) is the electric field at x = W for any value of z. To substitute equation (23) into (22), the surface current is given by

$$J_s(z) = j\omega\varepsilon_0(\epsilon_2 - \epsilon_1)E(W,z)[\eta W cos(Kz)] \tag{24}$$

Figure 10(a) and (b) show a periodic perturbed boundary is equivalent to a planar boundary with a periodic surface current as indicated in equation (24). The periodic surface current can be generated by mode *p* with a propagation constant of β_p that is coupled or phase-matched to mode *q* with a propagation constant of β_q in the grating vector K. The magnitude of K is the sum of the magnitudes of β_p and β_q for a 1st order grating. The coupling coefficient derived from this approach is equivalent to that of equation (14) [20], [22].

1.2.1.3 Figure of Merits

Based on equations (14) and (24), the strength of a grating is proportional to the index of refraction difference on either side of the grating boundary and to the grating confinement factor, or to the magnitude of the optical field at the grating interface. We introduce two Figures of Merit (FoM) to give a crude idea of the effectiveness of a grating

in an optical waveguide. FoM_a is the relative permittivity difference between two materials on both sides of a grating (n_1^2 and n_2^2) multiplied by the grating confinement factor (Γ_g).

$$FoM_a = (n_1^2 - n_2^2)\Gamma_g \tag{25}$$

FoM_b is the relative permittivity difference multiplied by the fraction of the peak of the electric field in the center of the grating.

$$FoM_b = (n_1^2 - n_2^2) \cdot E^2(W, z) \tag{26}$$

1.2.2. Floquet-Bloch Theory

First order periodic gratings can be analyzed with coupled mode theory (section 1.2.1) for shallow grating depths. However, to treat deep grating depths and 2nd and higher order gratings, we use a numerical Floquet-Bloch approach [23], [24], [25]. The Floquet-Bloch analysis satisfies the boundary condition at each waveguide interface in the grating waveguide. In addition, boundary conditions are satisfied at the interface between the grating region and the non-grating optical waveguide region.

Considering the transverse electric (TE) mode propagating along the z direction, the component of the electric field in the y direction in the i^{th} layer of a periodic grating structure is given by [24]

$$E_y^{(i)}(x, y) = f^{(i)}(x, z)e^{-i\gamma z} \tag{27}$$

where $\gamma = \alpha + j\beta$ is the complex propagation constant of the guided mode, α is the field attenuation coefficient, β is the longitudinal propagation constant, and $f^{(i)}(x, z)$ is the amplitude of the electric field as well as a periodic function so that it can be written as $f^{(i)}(x, z) = f^{(i)}(x, z + \Lambda)$. $f^{(i)}(x, z)$ is also expandable in a Fourier series:

$$f^{(i)}(x,z) = \sum_{n=-\infty}^{\infty} f_n^{(i)}(x) e^{-jnKz} \tag{28}$$

Substituting equation (28) into equation (27), the electric field can be written as

$$\begin{aligned} E_y^{(i)}(x,y) &= f^{(i)}(x,z) e^{-i\gamma z} \\ &= \sum_{n=-\infty}^{\infty} f_n^{(i)}(x) e^{-jnKz} e^{-i(\alpha+j\beta)z} \\ &= \sum_{n=-\infty}^{\infty} f_n^{(i)}(x) e^{-jK_{zn}z} \end{aligned} \tag{29}$$

where $f_n^{(i)}(x)$ is the amplitude of the electric field of the n^{th} space harmonic in the i^{th} layer, and K_{zn} is the complex propagation constant of the n^{th} space harmonic

$$K_{zn} = \beta_n - j\alpha = (\beta + nK) - j\alpha \tag{30}$$

and, β_n is the longitudinal propagation constant of the n^{th} space harmonic, K is the grating wavenumber, and α is the attenuation constant. 2α refers to the power attenuation coefficient. If $\alpha > 0$ in a first order grating, light is being reflected. Above first-order, an $\alpha > 0$ can also correspond to leakage of energy into the substrate or superstrate due to leaky modes. Since the power attenuation of an optical mode is proportional to $e^{-2\alpha z}$, the intensity of light travelling in the optical waveguide decreases to e^{-1} within a distance of

$$z = L = N\Lambda = \frac{1}{2\alpha} \tag{31}$$

where L is the grating length and N is the number of grating periods. Equation (31) provides the length of the grating required to reduce the intensity of light to e^{-1} (or ~ 0.37).

The Floquet-Bloch method provides a precise solution of gratings in waveguides including the complex propagation constants (transverse and longitudinal) and of the electric and magnetic field distributions, shows the portion of light that is deflected in multiple directions and the spectral linewidths of the deflected light. The Floquet-Bloch

approach has been extended to analyze gratings etched through multiple epitaxial layers and for multiple grating layers resulting from ECS structures. More details on ECS gratings will be provided in later chapters .

Chapter 2

ENHANCED COUPLING STRENGTH GRATINGS

2.1. Conventional Grating Waveguides: SOI, DFB, and DBR

Gratings in Silicon On Insulator (SOI) waveguides were demonstrated with outcoupling efficiency greater than 60% in a short grating length of 13 μm at a wavelength of 1550 nm [2]. Due to problems of generating light from silicon discussed in chapter 1, light has to be generated by either growing III-V material or wafer bonding III-V material to silicon, or externally generated light has to be coupled into and out of silicon photonic waveguides [26], [27]. Gratings have long been used in semiconductor lasers, mostly to obtain single frequency operation. For some applications, such as optical pumps for solid state lasers, broad area (100 μm wide) lasers that consist of numerous lateral and longitudinal modes are suitable. Such lasers are often referred to as gain-guided lasers. Other applications require that the output of the semiconductor laser have a single transverse TE_{00} or TM_{00} mode to provide an output beam that can be efficiently coupled to optical waveguides or focused to near diffraction limited spots. These lasers are known as single transverse mode lasers but can have numerous longitudinal modes. Finally, applications such as telecommunications and spectroscopy require a very narrow, single spectral line. Such single frequency lasers generally are either distributed feedback (DFB) lasers or distributed Bragg reflector (DBR) lasers. DFB and DBR lasers typically incorporate III-V waveguides having wavelength selective gratings to provide single

frequency operation. The grating of a DFB laser can be etched into the substrate followed by one epitaxial growth of the complete laser structure. Alternatively, the grating may be etched into the p-type cladding layer above the active region, and the remaining semiconductor layers are regrown above the grating. DFB lasers always have the grating co-located with the active region [28], [29].

A DBR laser uses a passive grating at one or both ends of the active region that provide a wavelength selective reflectivity to reflect light into the laser cavity for optical feedback [30]. In recent years, combinations of passive and active gratings have been used in semiconductor lasers, and such structures are referred to as distributed reflector (DR) lasers [31].

Gratings used for both DFB and DBR lasers in III-V materials are typically hundreds of μm long due to a low index contrast at the grating interface, a low grating confinement factor, or a low value of the electric field at the grating interface. The gratings used in DFB, DBR and DR lasers are often first-order gratings that only provide in-plane reflection and have a grating period $\Lambda = \lambda/(2n_{eff})$ where n_{eff} is the effective index. Gratings have also been used in second-order ($\Lambda = \lambda/n_{eff}$) to outcouple light from semiconductor lasers [14]. However, until this ECS work, all of the grating outcouplers in III-V materials required hundreds or even thousands of μm to outcouple a large (>50%) amount of light in a single pass from a second-order grating.

If the short outcoupler gratings demonstrated in silicon photonic waveguides could be obtained in III-V semiconductor waveguides, lasers could incorporate such short gratings to couple light into silicon photonic circuits.

Furthermore, efficient and short horizontal cavity lasers could be tested at the wafer level like vertical cavity surface emitting lasers (VCSELs) with the additional advantage of providing wavelengths beyond 1 μm with high power. VCSELs with wavelengths over 1 μm are limited by the thicker quarter wave DBR layers and the low index contrast between InGaAs and InP or InGaAlAs and InP.

In this chapter, the effectiveness of conventional gratings and ECS gratings are analyzed by the Figure of Merits discussed in chapter 1:

$$FoM_a = (n_1^2 - n_2^2)\Gamma_g \tag{32}$$

$$FoM_b = (n_1^2 - n_2^2) \cdot E^2(W, z) \tag{33}$$

FoM_a is the relative permittivity difference between two materials on both sides of a grating (n_1^2 and n_2^2) multiplied by the grating confinement factor (Γ_g). FoM_b is the relative permittivity difference multiplied by the fraction of the peak of the electric field in the center of the grating.

For simplicity, calculations are for a one-dimensional cross-section waveguide with TE polarized modes at a wavelength of 1550 nanometers. To discuss the ECS concept, the indices of refraction are limited to one decimal place.

In Figure 11(a), a typical grating structure in a silicon photonics waveguide has a high index contrast between a silicon core layer with the index of 3.5 (n_1) and SiO_2 outer layers with an index of 1.5 (n_2, n_3). Typical thickness values for a silicon photonic waveguide with a grating coupler are W_{core} = 0.2 μm and W_g = 0.1 μm [2], [32]. This waveguide has a high relative permittivity contrast at both the grating interface (n_1^2-n_2^2 = 10) and at the interface between the core and substrate layer (Δn_{sub} = 2). A large grating confinement factor ($\Gamma_{grating}$ = 15.3%) results from the large portion of the optical mode

confined in the grating layer as shown in Figure 11(a). FoM_a of this silicon photonics waveguide is 1.53, that is, FoM_a is equal to $(n_1^2-n_2^2)$ multiplied by $\Gamma_{grating}$. Moreover, a fraction of the peak of the electric field in the center of the grating ($E^2 = 0.3165$) is also high. FoM_b of this waveguide is 3.165, that is, FoM_b is equal to $(n_1^2-n_2^2)$ multiplied by E^2. Values of these parameters are listed in Table 1.

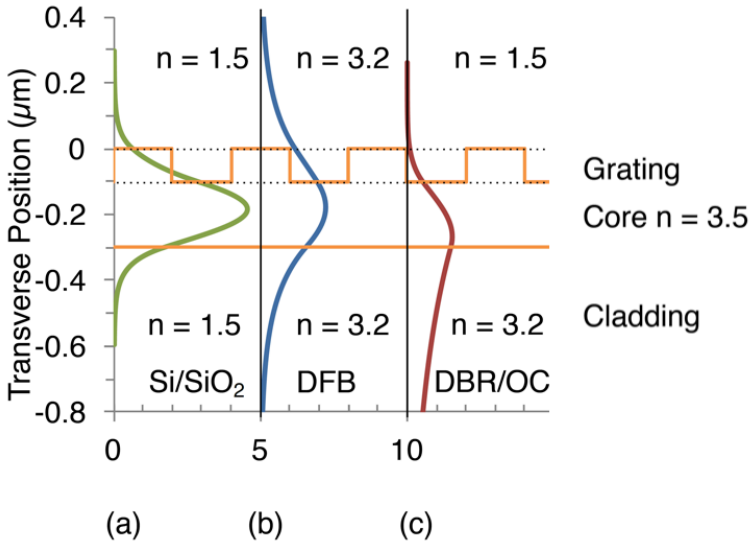

Figure 11. Field intensity of (a) silicon photonics waveguide, (b) DFB, (c) DBR/OC.

In Figure 11(b), a general DFB grating waveguide has a high-index center layer (3.5) and slightly low-index outer layers on both sides. The superstrate layer over the grating is usually an alloy of the III-V compound materials that have an index of refraction higher than the superstrate of silicon photonics waveguides. The index difference on both sides of the core layer is on the order of 0.1 to 0.5, depending on the semiconductor composition. Assume W_{core} is 0.2 μm, W_g is 0.1 μm, and the index of outer layers is 3.2. This DFB waveguide has a low relative permittivity contrast at the grating interface (n_1^2-

$n_2^2 = 2.01$) and a low index contrast at the interface between the core and substrate layer ($\Delta n_{sub} = 0.3$). A large grating confinement factor ($\Gamma_{grating} = 15.8\%$) results from the large portion of the field intensity confined in the grating layer as shown in Figure 11(b), resulting in FoM_a of this DFB waveguide to be 0.32. Moreover, a fraction of the peak of the electric field in the center of the grating ($E^2 = 0.6981$) is high so that FoM_b of this waveguide is 1.4032. Values of these parameters are listed in Table 1. In Figure 11(c), a typical DBR grating structure has a high-index core layer (n_1), a slight low-index substrate layer (n_3), and a superstrate layer of a relatively low index of refraction (n_2=1.5). The index difference at the grating interface is much higher than the index difference between the core and substrate layer. Assume W_{core} is 0.2 μm, W_g is 0.1 μm, and n_3 is 3.2. This DBR waveguide has a high relative permittivity contrast at the grating interface and a low index contrast at the interface between the core and substrate layer ($\Delta n_{sub} = 0.3$). A small grating confinement factor ($\Gamma_{grating} = 2.5\%$) is due to the small portion of the optical mode confined in the grating layer as shown in Figure 11(c), resulting in a FoM_a for this DBR waveguide of 0.25. Moreover, a fraction of the peak of the electric field in the center of the grating ($E^2 = 0.1519$) is low, resulting in a FoM_b of 1.519.

Table 1 indicates the properties of a silicon photonics waveguide, a DFB waveguide and a DBR waveguide as shown in Figure 11(a) to (c). All waveguides share the same thickness of the core layer W_{core} of 0.2 μm with the index of 3.5 and the same grating depth of 0.1 μm. Compared to silicon photonics waveguides, conventional DFB waveguides have a large grating confinement factor and a large fraction of the peak of the field intensity in the center of the grating. But the relative permittivity difference on both sides of the core layer is small, resulting in a small value of FoM_a and FoM_b. In addition, conventional

DBR waveguides have a large relative permittivity contrast at the grating interface. The grating confinement and the fraction of the peak of the optical mode are small. That results in a small value of FoM_a and FoM_b as well. According to the calculated FoM values, the grating effectiveness of a silicon photonics grating waveguide is much larger than those of conventional DFB or DBR grating waveguides.

Table 1. Properties of different types of typical optical waveguides with a grating.

	Si WG	DFB	DBR
Liner (nm)	NA	NA	NA
Δn_{sub}	2	0.3	0.3
$n_1^2-n_2^2$	10	2.01	10
$\Gamma_{grating}$	15.3%	15.8%	2.5%
$E^2 = I_b/I_{peak}$	0.3165	0.6981	0.1519
FoM_a	1.53	0.32	0.25
FoM_b	3.165	1.4032	1.519

Although practical semiconductor laser waveguides have numerous layers containing multiple quantum wells and barriers, and separate confinement heterostructure (SCH) layers, all with different compositions and doping concentrations, such structures can be approximated with one central "core" layer surrounded by cladding layers. For this reason, and also to demonstrate the key concept of ECS gratings, we consider a simple, asymmetric three-layer waveguide with a grating at one of the interfaces.

2.2. Concept of Enhanced Coupling Strength Grating

To increase the strength or coupling of a grating, it is necessary to increase the index difference at the grating boundary and the grating confinement factor, or equivalently,

increase both the index difference and the magnitude of the electric field at the grating boundary. This is achieved in III-V materials by adding a thin low-index "liner" layer between the grating layer followed by a high-index cover layer as shown in Figure 12. The liner layer can be a low-index material such as silicon nitride or silicon dioxide. The cover layer can be made of a transparent, low loss high-index material such as amorphous silicon (a-Si) or other amorphous, transparent III-V materials. This grating configuration is defined as an Enhanced Coupling Strength (ECS) grating waveguide as shown in Figure 12. The low-index liner layer provides a large contrast of the relative permittivity (n_1^2-n_2^2) at the grating interface. The high-index cover layer increases the grating confinement factor by increasing the fraction of the optical field in the grating region, which requires that the value of the refractive index of the cover layer be greater than the effective index of the waveguide. Figure 12 applies to III-V waveguides as the refractive index of the cladding layer (n_3) is 3.2. Further, Figure 12 applies to silicon photonics waveguides as the refractive index of the cladding layer (n_3) is 1.5.

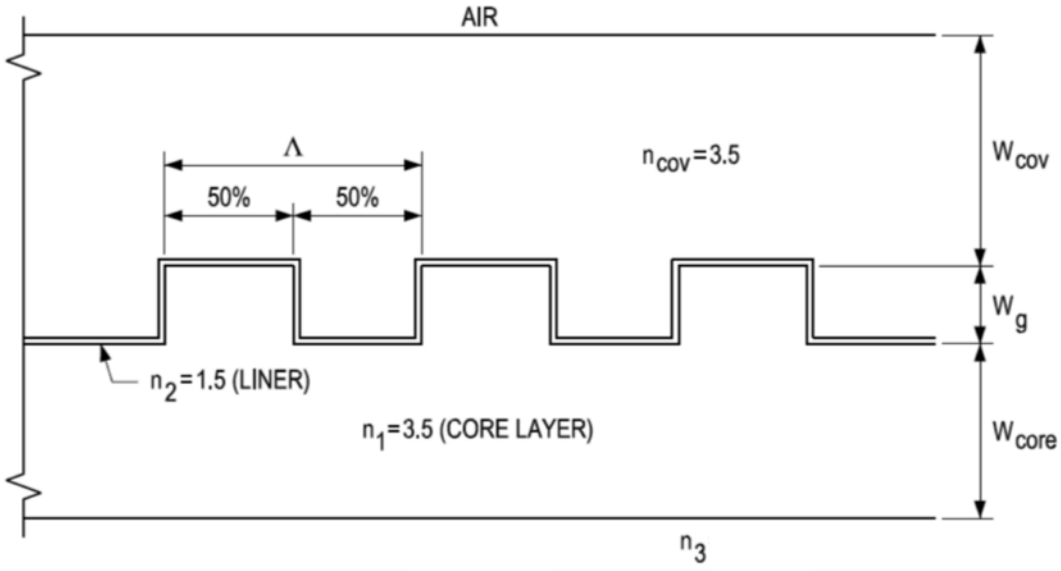

Figure 12. Sketch of a waveguide that includes an ECS grating with a thin, low-index liner and high index cover layer.

In the later chapters, we will discuss how the ECS technique improves the grating efficiency by varying the thickness of the liner, cover and core layer, and the depth of the grating by optimizing the crude FoMs. Adding a thin liner layer results in two periodic interfaces, splitting the periodic index variation into three horizontal regions (I, II, and III) as indicated in Figure 13. The fields of the resulting waveguide are approximated by considering the average refractive index of each section of a grating. The average index of refraction is calculated by taking the square root of the average relative permittivity of each section of a grating. A 50% grating duty cycle is defined at the interface between the silicon core layer and the liner layer shown in Figure 13.

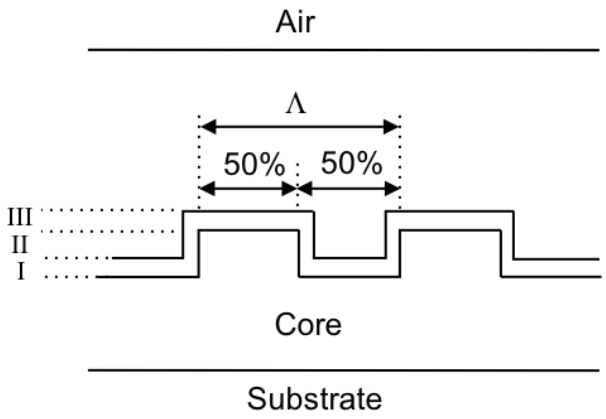

Figure 13. Sketch of regions I, II, and III of a grating with a liner and cover layer.

2.2.1. Varying the Thickness of Cover, Core and Grating Layers

The ECS grating configuration shown in Figure 12 can also be used to roughly optimize the thicknesses of the cover, core, and grating layer by calculating FoM_a and FoM_b. Examples of such plots are shown in Figure 14 to Figure 16. In the simple, uniform core, Figure 14(a) shows the index profile of an ECS grating waveguide with a fixed core layer of 0.2 μm, a fixed grating depth of 0.3 μm, a fixed liner thickness of 10 nm and a variable thickness of the cover layer. Figure 14(b) shows the grating confinement factor as a function of the thickness of the cover layer. For the specific choice of layer indices, layer thicknesses, grating period, and grating duty cycle, the optimum thickness of the cover layer is 0.3 μm as shown in Figure 14(b).

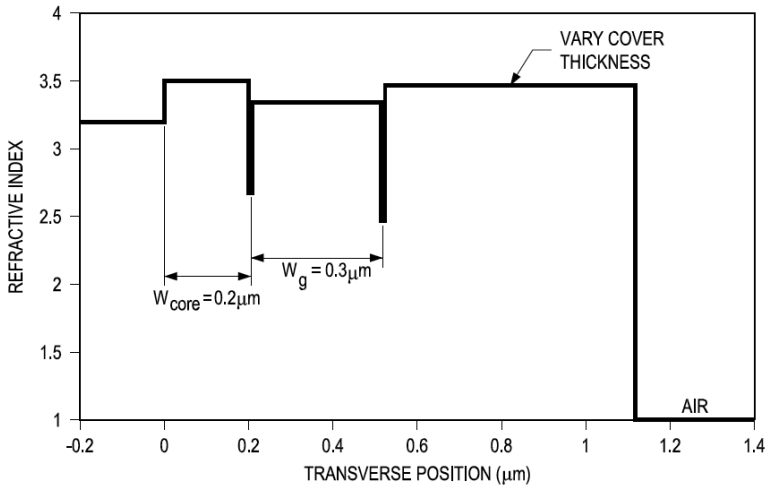

(a)

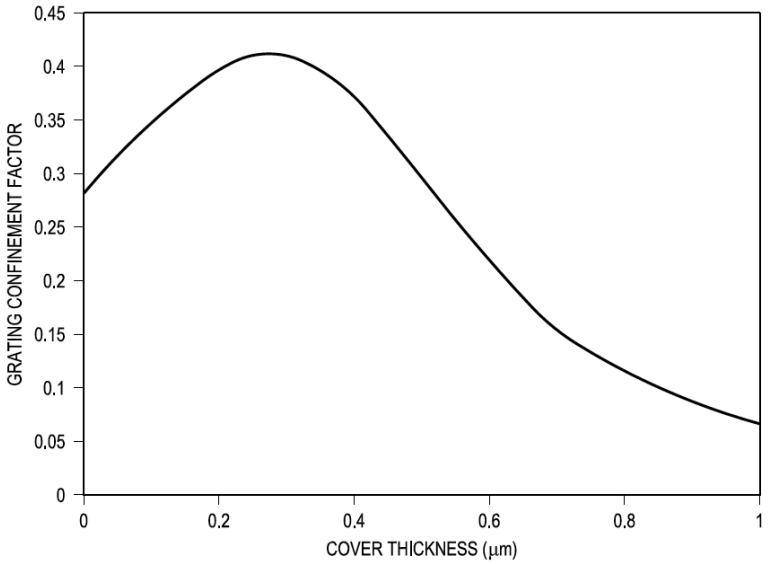

(b)

Figure 14. (a) The index profile of the ECS waveguide shown in Figure 12 with a fixed core thickness of 0.2 μm, a grating thickness of 0.3 μm and a variable thickness of the high-index cover layer, and (b) the grating confinement factor as a function of the thickness of the high-index cover layer.

Figure 15(a) to (c) shows the ECS waveguide index profile, the grating confinement factor as a function of the core layer thickness, and the field intensity plots in the transverse

direction. In the simple uniform core, Figure 15(a) shows the index profile of an ECS grating waveguide with a fixed grating depth of 0.2 μm, a fixed liner thickness of 10 nm, a fixed high-index cover layer of 0.2 μm, and a variable thickness of the core layer. Figure 15(b) shows the grating confinement factor as a function of the thickness of the core layer up to 0.5 μm. For the choice of layer indices, layer thicknesses, grating period, and grating duty cycle, the optimum thickness of the core layer is below 0.1 μm as shown in Figure 15(b). The electric field intensity as a function of the transverse direction with variable core thickness ranging from 0.1 to 0.5 μm is plotted in Figure 15(c).

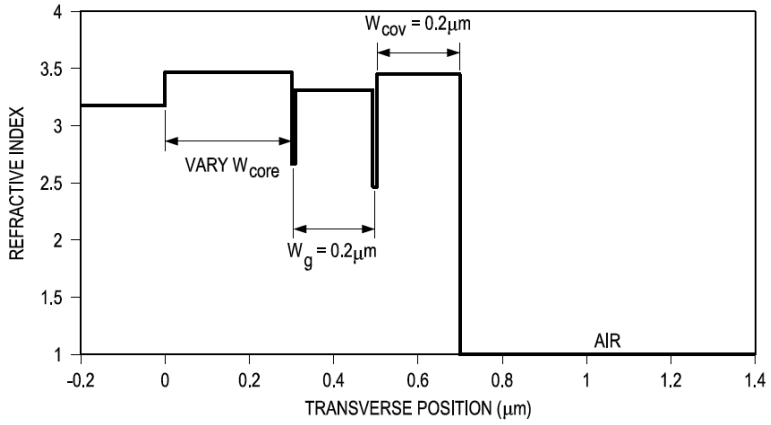

(a)

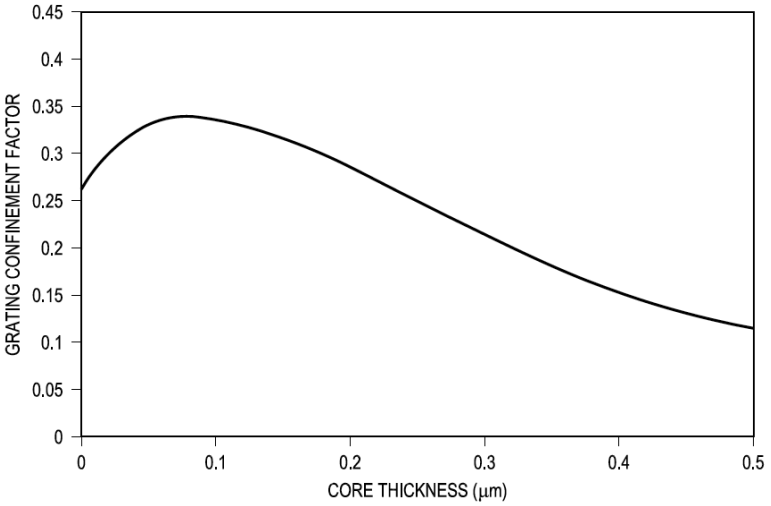

(b)

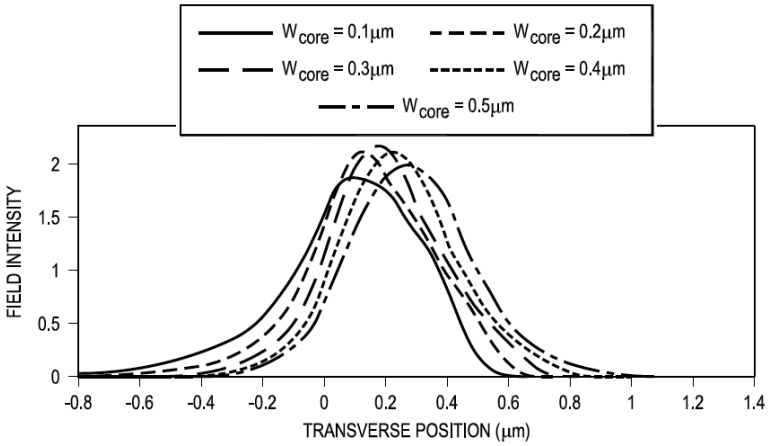

(c)

Figure 15. (a) The index profile of the ECS waveguide with a variable core thickness, (b) the grating confinement factor as a function of the core thickness, and (c) the field intensity plots of different core thicknesses.

Figure 16(a) to (c) shows the index profile, grating confinement factor as a function of the grating depth, and the field intensity plots in the transverse direction. In the simple uniform core, Figure 16(a) shows the index profile of an ECS grating waveguide with a fixed core thickness of 0.2 μm, a fixed liner thickness of 10 nm, a fixed high-index cover layer of 0.1 μm, and a variable thickness of the grating depth. Figure 16(b) shows the grating confinement factor as a function of the grating depth up to 0.5 μm. The electric field intensity as function of the transverse direction with variable grating depth ranging from 0.1 to 0.5 μm is plotted in Figure 16(c).

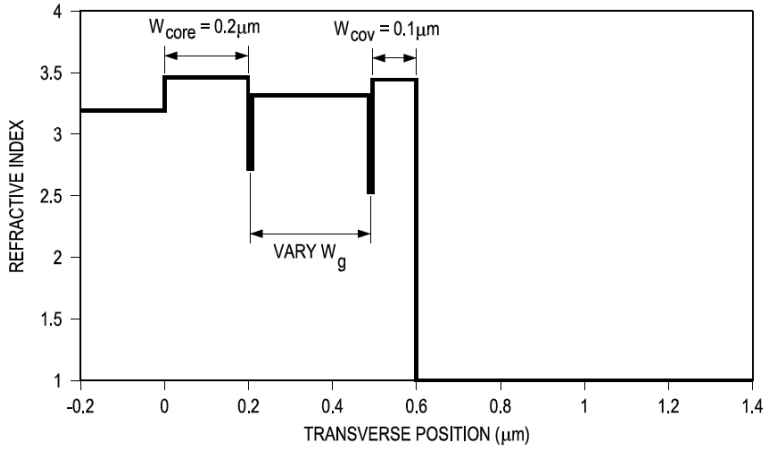
W core = 0.2μm
W cov = 0.1μm
VARY W g
REFRACTIVE INDEX
TRANSVERSE POSITION (μm)

(a)

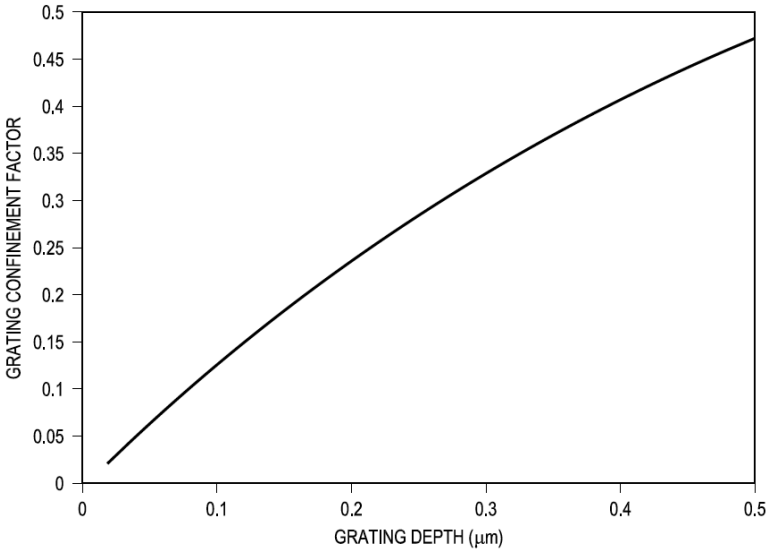
GRATING CONFINEMENT FACTOR
GRATING DEPTH (μm)

(b)

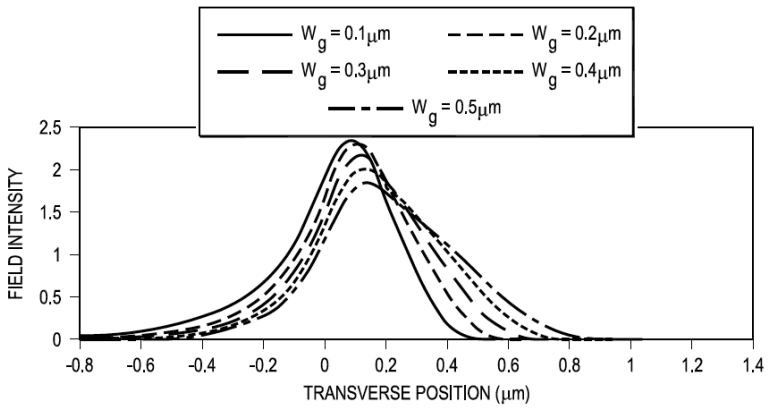
W g = 0.1μm
W g = 0.2μm
W g = 0.3μm
W g = 0.4μm
W g = 0.5μm
FIELD INTENSITY
TRANSVERSE POSITION (μm)

(c)

Figure 16. (a) An index profile of the ECS grating waveguide, (b) the grating confinement factor as a function of the thickness of the grating layer, and (c) a field intensity plots for grating thicknesses ranging from 0.1 to 0.5 μm.

2.2.2. Variable Liner Thickness

The profile of the refractive index in Figure 17(a) is for an ECS grating waveguide in Figure 12. The index of the substrate is 3.2, the index of the core is 3.5 with a thickness of 0.2 μm, a fixed grating depth of 0.1 μm with variable thickness of a liner layer ranging from 5 nm to 25 nm, and the index of the cover layer is 3.5 with a thickness of 0.15 μm. The grating region splits into three horizontal sections I, II, and III as shown in Figure 13. We can approximate the fields of the resulting waveguide by considering the average refractive index of each section of a grating. The average index of refraction is calculated by taking the square root of the average relative permittivity of each section of a grating. Assuming the grating duty cycle at the interface between the core layer and the liner in Figure 13 is 50%, the average index of refraction in section I is 2.693.

$$n_{ave}(section\ I) = \sqrt{50\% \times 3.5^2 + 50\% \times 1.5^2} = 2.693 \tag{34}$$

Additionally, if the liner thickness in Figure 13 is 5 nm and the grating period is 0.5 μm, the average index of section II is 3.471.

$$\begin{aligned} n_{ave}(section\ II) &= \sqrt{50\% \times 3.5^2 + 2\% \times 1.5^2 + 48\% \times 3.5^2} \\ &= 3.471 \end{aligned} \tag{35}$$

And the average index of section III is 2.655.

$$n_{ave}(section\ III) = \sqrt{52\% \times 1.5^2 + 48\% \times 3.5^2} = 2.655 \tag{36}$$

The corresponding field intensities for liner thicknesses of 5, 10 and 25 nm (in Figure 13) are shown in Figure 17(b).

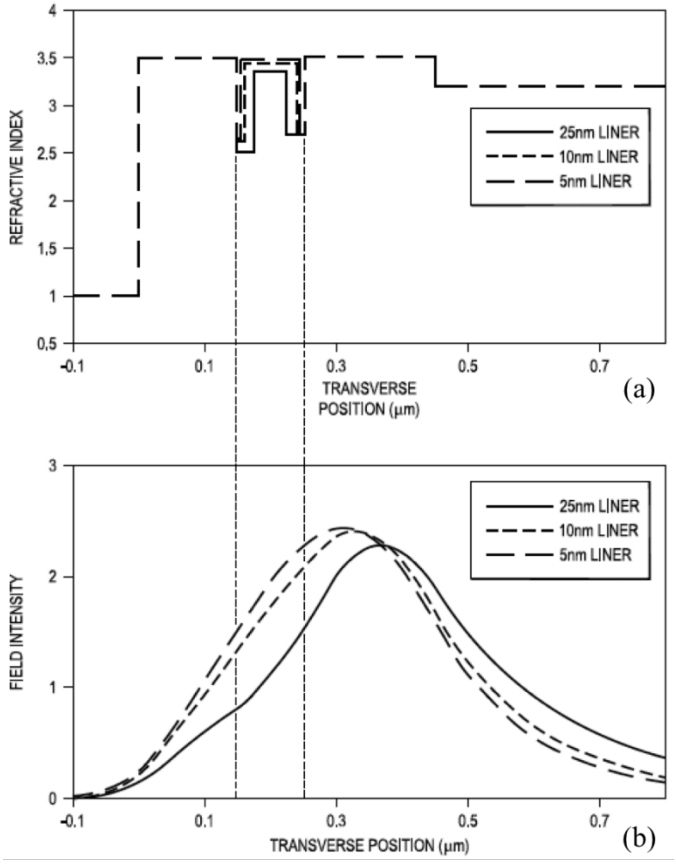

Figure 17. (a) The index profile for a structure shown in Figure 12 with a liner thickness of 5, 10, and 25 nm and the grating section presented as the average relative permittivities in grating region of I, II, and III, and (b) field intensity plots for liner thicknesses ranging from 5 to 25 nm.

The fraction of the field intensity in the grating region increases as the thickness of the liner decreases. This simple approximation using the effective indices of the grating sections shows that the values of the grating confinement factor increase as the liner thickness decreases. The fraction of the peak field in the middle of the grating also increases as the liner thickness decreases as indicated in Table 2, as also indicated by FoM_a and FoM_b. Even in the case of a liner thickness of 25 nm, which is not optimized, the

values of the FoMs are still three times larger than both conventional DFB and DBR waveguides.

Table 2. Properties of different types of optical waveguides with a grating configuration.

	Si WG	DFB	DBR	ECSG	ECSG	ECSG	ECSG-SI
Liner (nm)	NA	NA	NA	25	10	5	5
Δn_{sub}	2	0.3	0.3	0.3	0.3	0.3	2
n_1^2-n_2^2	10	2.01	10	10	10	10	10
$\Gamma_{grating}$	15.3%	15.8%	2.5%	11.1%	17.1%	19.3%	30.1%
$E^2 = I_b/I_{peak}$	0.3165	0.6981	0.1519	0.4467	0.7207	0.8003	0.9759
FoM_a	1.53	0.32	0.25	1.11	1.71	1.93	3.01
FoM_b	3.165	1.4032	1.519	4.467	7.207	8.003	9.759

Figure 18 shows the normalized intensity modal profile for (a) silicon photonics waveguide, (b) DFB waveguide, (c) DBR/outcoupler waveguide, (d) ECS DBR/outcoupler waveguide, and (e) ECS silicon photonics waveguide. All waveguides share the same thickness of the core layer (W_{core} = 0.2 μm), the same refractive index of the core layer (3.5), and the same grating depth of (0.1 μm). The grating in silicon photonics waveguides shown in Figure 18(a) can have an efficient outcoupler grating due to a large index difference between the high-index Si core and the indices of the substrate and superstrate. Nevertheless, gratings in III-V waveguides (DBR, DFB) are fabricated with layers having a small index difference for at least one interface as shown in Figure 18(b) that reduce the interaction of the field with the grating. By applying a thin low-index layer followed by a thicker high-index cover layer over the grating, the waveguide mode moves into the grating region that results in a larger fraction of the field in the grating region as shown in Figure 18(d) and Figure 18(e).

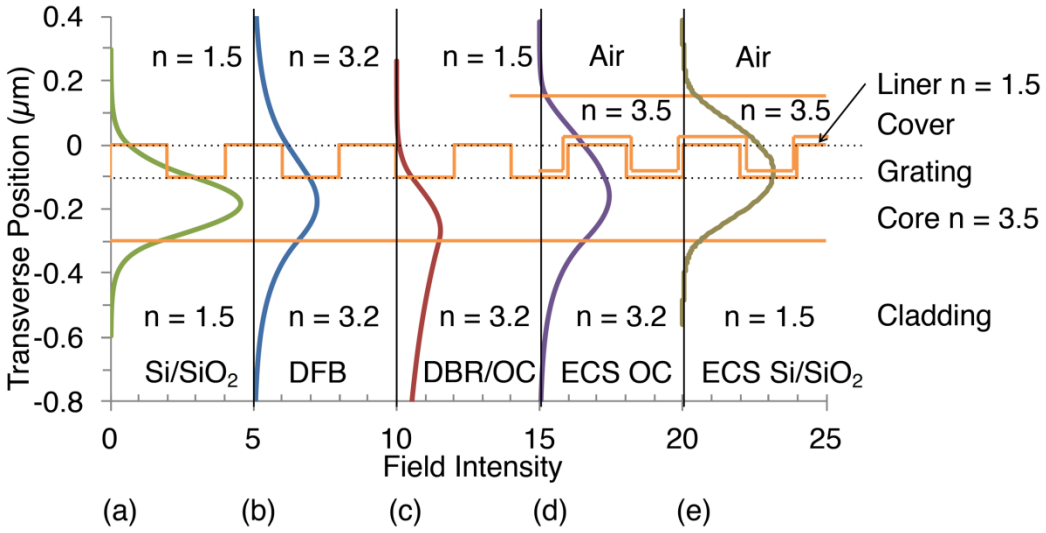

Figure 18. Field intensity of (a) silicon photonics waveguide, (b) DFB, (c) DBR/OC, (d) ECS outcoupler, and (e) ECS silicon photonics waveguide.

2.3. ECS Silicon Photonics Waveguide

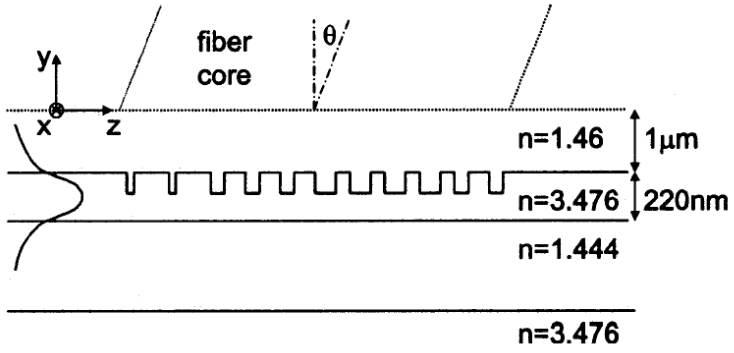

Figure 19. A silicon photonic grating outcoupler [2].

An early and common silicon grating outcoupler [2] consists of 220 nm of silicon on a buried oxide layer. The grating is etched into the silicon to a depth of 100 nm and covered by 1 μm of silicon dioxide. The grating is 13 μm long with a variable grating

period and duty cycle in order to shape the outcoupled beam into a Gaussian for maximum coupling into the fiber. The authors report about 35% of light is directed into the substrate and 65% of light is directed into the superstrate.

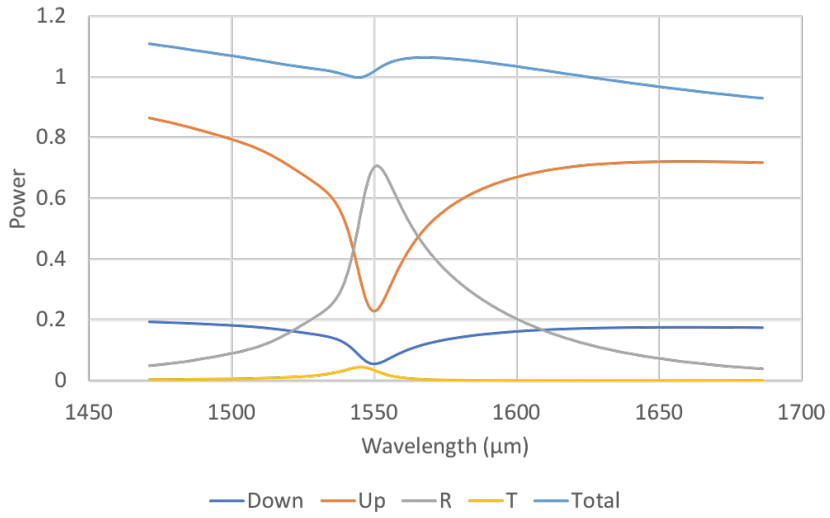

Figure 20. Calculated power spectrum for the 13 μm long silicon photonics structure [1].

The silicon photonics grating waveguide of Figure 19 is analyzed by the SMU developed Floquet-Bloch approach and the fraction of the incident power radiated down (P_{do}), the incident power radiated up (P_{up}), the incident power reflected (R), the incident power transmitted (T) and the sum of the incident power reflected, transmitted and radiated as a function of the wavelength is shown in Figure 20. The grating length is 13 μm and a uniform 50% duty cycle grating is modeled rather than the variable duty cycle and variable grating period shown in Figure 19. The 2nd Bragg grating period is 598.3 nm and occurs at a wavelength of 1550 nm. The upward radiated power is about 72% and the downward radiated power into the substrate is about 17%, which is similar to that reported for the structure shown in Figure 21.

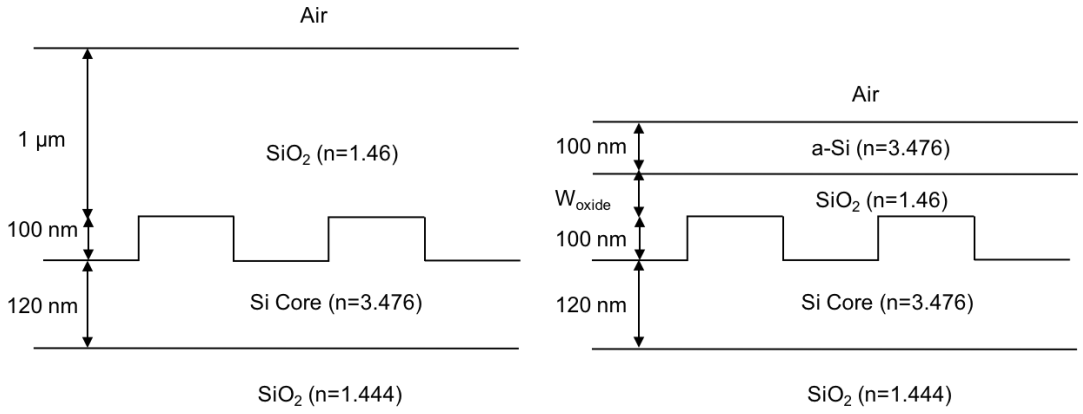

(a) (b)

Figure 21. (a) silicon photonics grating waveguide and (b) ECS silicon photonics waveguide with a 120-nm Si core layer, a variable silicon dioxide layer above grating teeth, and a 100-nm a-Si cover layer.

Figure 21(a) shows the index values of a silicon photonics waveguide with a uniform grating with a silicon core thickness of 120 nm, a grating depth of 100 nm followed by 1 μm of oxide. Figure 21(b) is an ECS silicon photonics grating with a silicon dioxide liner layer and a 100-nm a-Si cover layer above the grating.

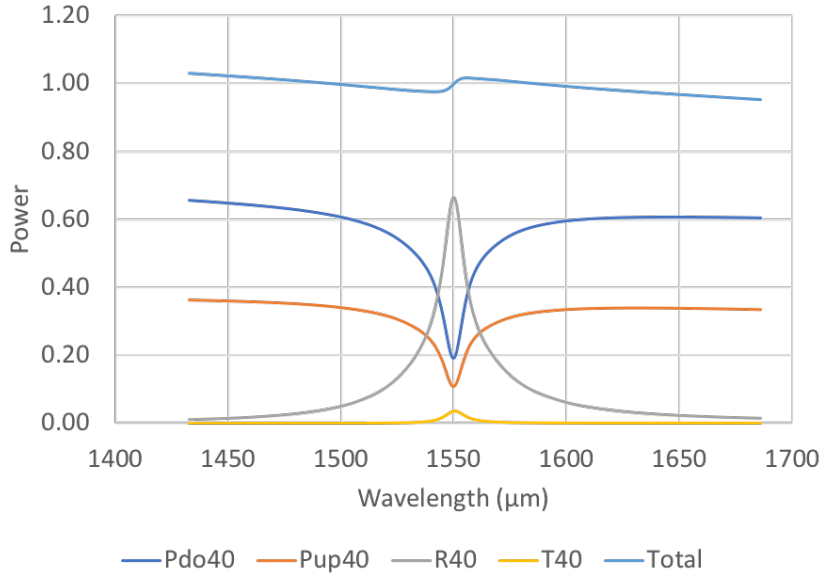

Figure 22. Power spectrum for the silicon photonics grating outcoupler shown in Figure 21(a) with a length of 24 µm.

Figure 22 shows the power radiated down (P_{do}), power radiated up (P_{up}), total power radiated ($P_{up}+P_{do}$), power reflected (R), power transmitted (T) and sum of power as a function of the wavelength for the silicon photonics grating waveguide shown in Figure 21(a). The grating length is 24 µm with a 50% duty cycle. The 2nd Bragg grating period is 598.3 nm at a wavelength of 1550 nm. The excess of the total power from 100% shows that the maximum error of the Floquet-Bloch approach is below 5%. The upward radiated power is 34% and the downward radiated power is 60% so the total radiated power is 94%. The reflected power can be minimized by operating at the wavelength further away from the 2nd Bragg condition.

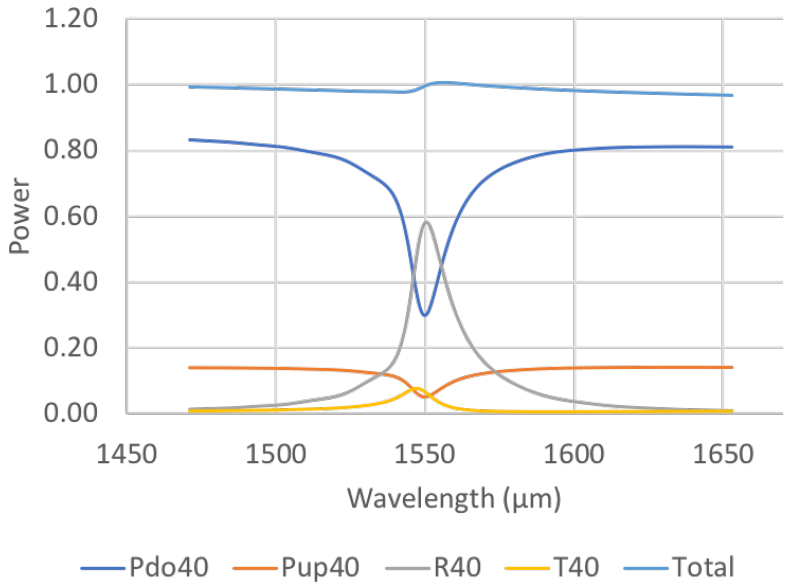

Figure 23. Power spectrum for the ECS grating waveguide shown in Figure 21(b) with a 100-nm liner layer.

Figure 23 shows the power radiated down (P_{do}), power radiated up (P_{up}), total power radiated ($P_{up}+P_{do}$), power reflected (R), power transmitted (T) and sum of all powers as a function of the wavelength for the ECS silicon photonics grating waveguide shown in Figure 21(b) with 100-nm liner layer above the grating (W_{oxide} = 100 nm). The grating length is 24 µm with a 50% duty cycle. The 2nd Bragg grating period is 586.4 nm at the wavelength of 1550 nm. The excess of the total power from 100% shows that the maximum error of the Floquet-Bloch approach is below 5%. The upward radiated power is 14%, the downward radiated power is 81%, and the total radiated power is 95%. Although the ratio of the upward and downward radiated power changes compared to the conventional silicon photonics grating in Figure 21 (a) the total radiated power doesn't change.

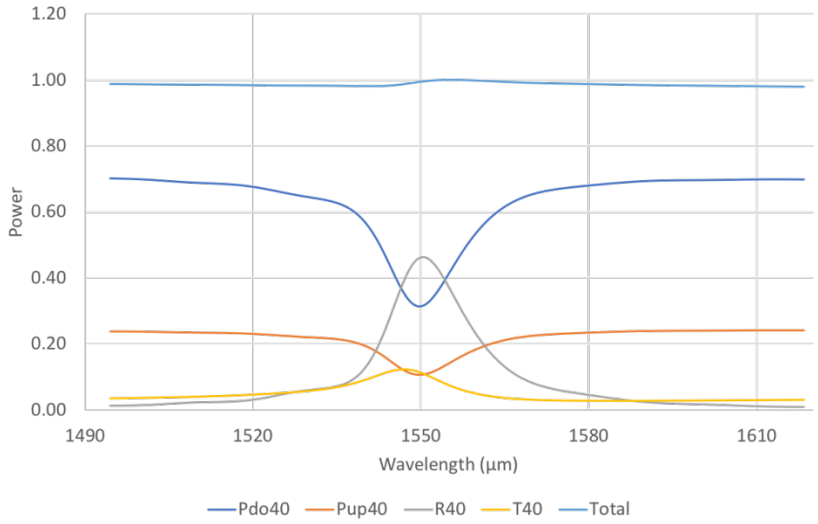

Figure 24. Power spectrum for the ECS grating waveguide with 50-nm liner shown in Figure 21(b).

Figure 24 shows the power spectrum as a function of the wavelength for the ECS silicon photonics grating waveguide shown in Figure 21(b) with 50-nm liner layer (W_{oxide} = 50 nm) above the grating. The grating length is 24 µm with a 50% duty cycle. The 2nd Bragg grating period is 574.3 nm at the wavelength of 1550 nm. Although the ratio of the upward and downward radiated power changes compared to the conventional silicon photonics grating in Figure 21 (a) the total radiated power doesn't change.

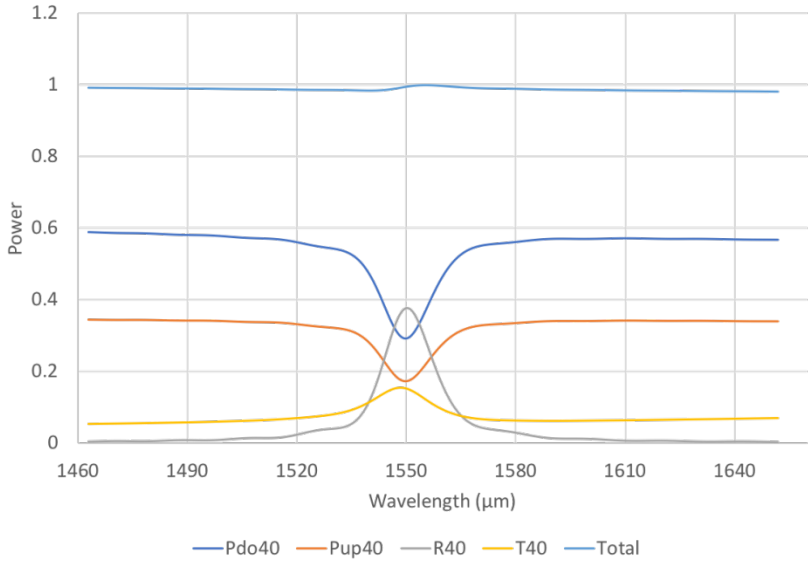

Figure 25. Power spectrum for the ECS grating waveguide with 25-nm liner shown in Figure 21(b).

Figure 25 shows the power spectrum as a function of the wavelength for the ECS silicon photonics grating waveguide shown in Figure 21(b) with a liner layer of 25 nm (W_{oxide} = 25 nm) above the grating teeth. The grating length is 24 µm with a 50% duty cycle. The 2nd Bragg grating period is 564.8 nm at the wavelength of 1550 nm. The upward radiated power is 34% and the downward radiated power is 57%, resulting in a total radiated power of 91%.

Although the ratio of the upward and downward radiated power changes compared to the conventional silicon photonics grating in Figure 21(a) the total radiated power doesn't change.

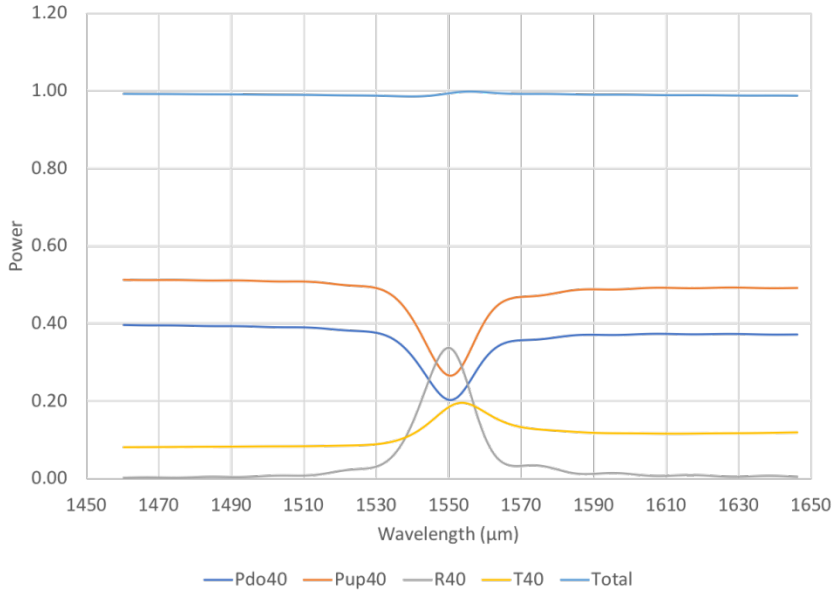

Figure 26. Power spectrum for the ECS grating waveguide shown in Figure 21(b) with low-index fillings between grating teeth (W_{oxide} = 0 nm)

Figure 26 shows the power spectrum as a function of the wavelength for the ECS silicon photonics grating waveguide shown in Figure 21(b) having a low-index material between grating teeth. The grating length is 24 µm with a 50% duty cycle. The 2nd Bragg grating period is 552.3 nm at the wavelength of 1550 nm. The upward radiated power is 49%, the downward radiated power is 37% and result in a total radiated power of 86%. Although the ratio of the upward and downward radiated power changes compared to the conventional silicon photonics grating in Figure 21 (a) the total radiated power decreases somewhat.

Figure 27 is a comparison chart of the radiated power at 1620 nm for the ECS grating waveguide and summarizes the results of Figure 23 to Figure 26.

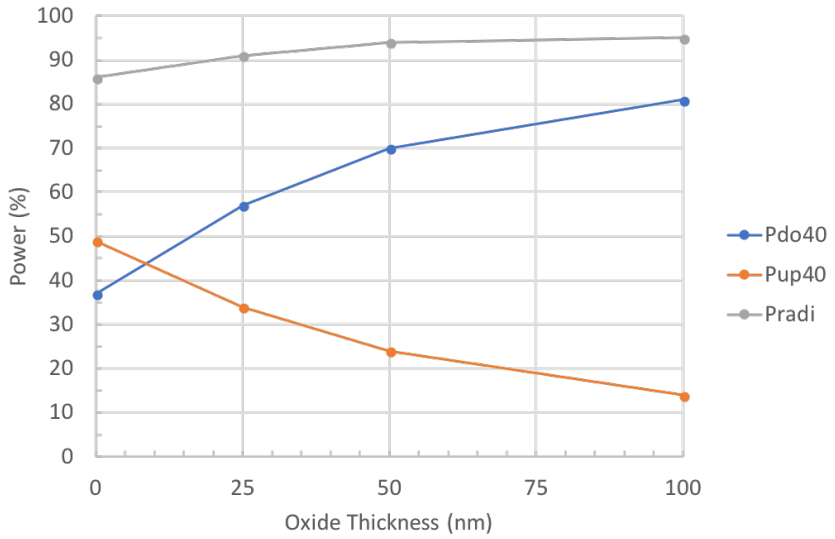

Figure 27. Radiation power as a function of oxide thickness above grating for the ECS grating waveguide.

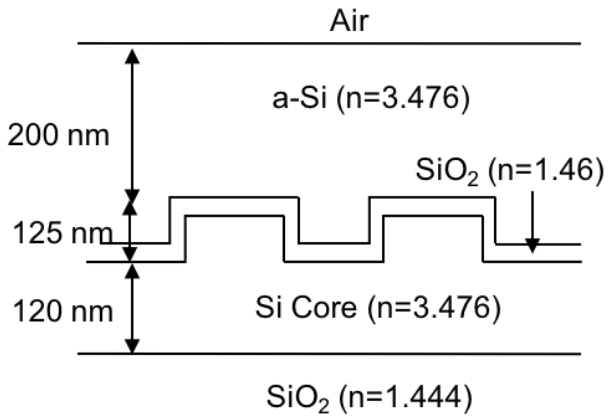

Figure 28. ECS silicon photonics grating waveguide with 25-nm oxide liner above grating followed by 200-nm a-Si cover layer.

Figure 28 shows the ECS grating in silicon photonics waveguide. The silicon core layer has a thickness of 120 nm. The grating is etched 100 nm deep in silicon, followed by the deposition of a thin 25-nm SiO_2 liner and a 200-nm amorphous Si cover layer. The total grating depth is 125 nm including the etched grating depth and the liner thickness. The etched grating has a 50% duty cycle.

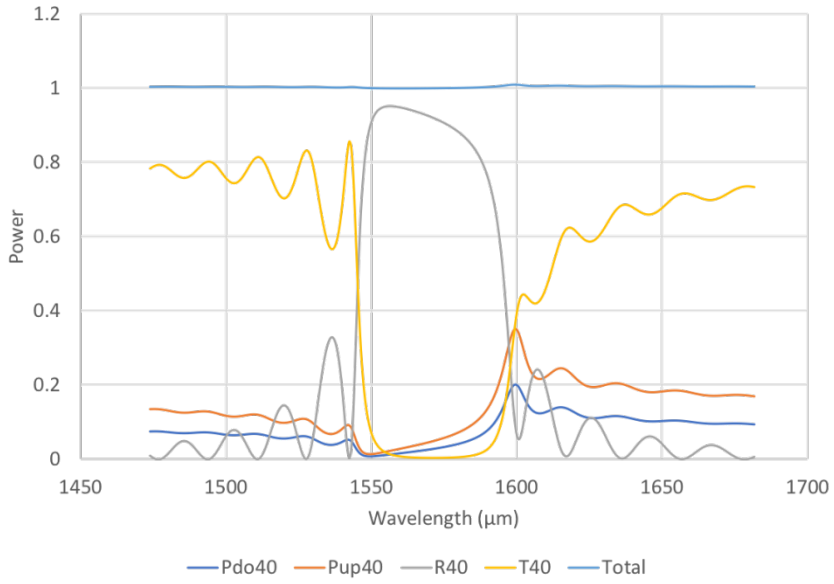

Figure 29. Power spectrum for ECS silicon structure with the thin liner shown in Figure 28.

Figure 29 shows the power spectrum as a function of the wavelength for the ECS silicon photonics grating waveguide shown in Figure 28 having a thin low-index liner above the grating. The 2nd Bragg period is 509.9 nm. The upward and downward radiated power are both less than 20%. Most of light is reflected in the stopband between 1550 nm to 1600 nm. This structure performs much like a 1st order Bragg grating.

Such a structure could enable efficient holographically patterned DBR reflector gratings, for semiconductor lasers emitting at wavelengths below about 800 nm. The shortest wavelength available for holography are presently between 229 or 264 nm by the frequency doubled (FreD) lasers [33], limiting the grating period to about 0.11 µm. For effective indices of about 3.3, the shortest semiconductor wavelength becomes 800 nm. By using an ECS DBR 2nd order grating, the limit on emission wavelength is reduced to ~

400 nm—and even lower in the GaN waveguides that can have effective indices of well under 3.

2.4. Summary

From the equations for the coupling coefficient, the coupling strength of a simple grating is proportional to the refractive index difference on either side of the grating interface, the grating confinement factor, and the fraction of the peak of the electric field of the waveguide mode at the centerline of the grating region. The Figure of Merit terms approximate the grating performance. These considerations suggest that the strength of an outcoupling grating can be improved by inserting a thin, low-index liner and a high-index cover layer on the top of a conventional III-V grating. For silicon photonics waveguides, we can change the ratio of upward and downward radiation by varying the liner thickness followed by the high-index cover layer above the grating teeth. The analysis of the ECS and conventional silicon photonics grating outcouplers did not show a dramatic improvement for the ECS structure because for a grating length of 24 μm, the conventional outcoupler was very efficient. However, we expect that for shorter grating lengths, perhaps 5 μm, we will find an advantage for ECS outcouplers in silicon photonic waveguides.

By adding a thin low-index liner layer between the high-index cover layer and grating, a second order Bragg grating can perform as an efficient first order Bragg grating for DBR mirrors.

Chapter 3

MODELING ECS GRATING OUTCOUPLERS IN 9-QW LASERS NEAR 1550 NM

In this chapter, we discuss the integration of an ECS grating coupler with a DBR ridge guide laser as shown in Figure 30 by using the simple planar layer approach and the numerical Floquet-Bloch analysis. The emitting wavelength of light from the ridge guide laser is near 1550 nm. The position and length of the ECS outcoupler are determined for the 9-QW laser waveguide.

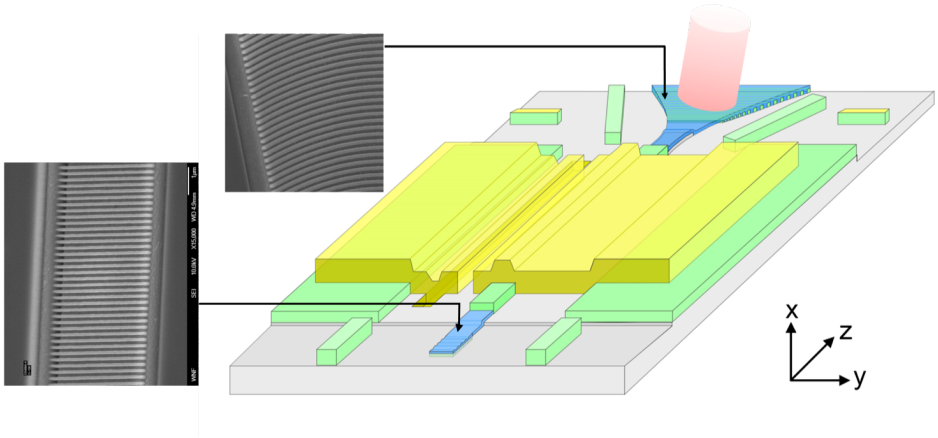

Figure 30. Integration of an ECS tapered coupler with a DBR ridge guide laser. The insets are SEM images of the coupler and DBR grating.

3.1. InGaAsP Grating and InP Grating Structure for the 9-QW Laser

3.1.1. InGaAsP Grating Coupler

Table 3 indicates the compositions, layer thicknesses and indices of refraction in the laser section of the 9-QW waveguide with the InGaAsP grating. The indices of refraction are calculated for a wavelength of 1550 nm. These compositions and thicknesses are generally used for semiconductor lasers [34]. The active region consists of 9 quantum wells (QWs) and 8 barriers sandwiched by two "separate confinement heterostructure" (SCH) layers. These are all made of InGaAsP with different mole fractions. The total thickness of the active region is 0.2 μm. First the InGaAs cap layer and p cladding InP layer are etched. Then the 200-nm InGaAsP grating is formed above the p-side SCH layer.

Table 3. 9-QW laser structure designed for an InGaAsP grating.

Layer	Composition	Thickness (um)	Material Index
Air		--	1
Cap	InGaAs	0.100	3.62525
P-clad	InP	2	3.16492
Space for grating	$In_{0.74}Ga_{0.26}As_{0.5}P_{0.5}$	0.2	3.35110
SCH	$In_{0.74}Ga_{0.26}As_{0.5}P_{0.5}$	0.041	3.35110
8x barriers	$In_{0.74}Ga_{0.26}As_{0.5}P_{0.5}$	0.008	3.35110
9x QWs	$In_{0.74}Ga_{0.26}As_{0.81}P_{0.19}$	0.006	3.50636
SCH	$In_{0.74}Ga_{0.26}As_{0.5}P_{0.5}$	0.041	3.35110
N substrate	InP	--	3.16492

3.1.1.1 Field Intensity in the Gain Region

Figure 31 shows the refractive index profile and field intensity in the transverse direction (x direction in Figure 30) for the 9-QW laser as tabulated in Table 3. These QWs

are not centered in the InGaAsP SCH layers because the ECS grating coupler will be placed in the p-side of the InGaAsP SCH layer to radiate light out.

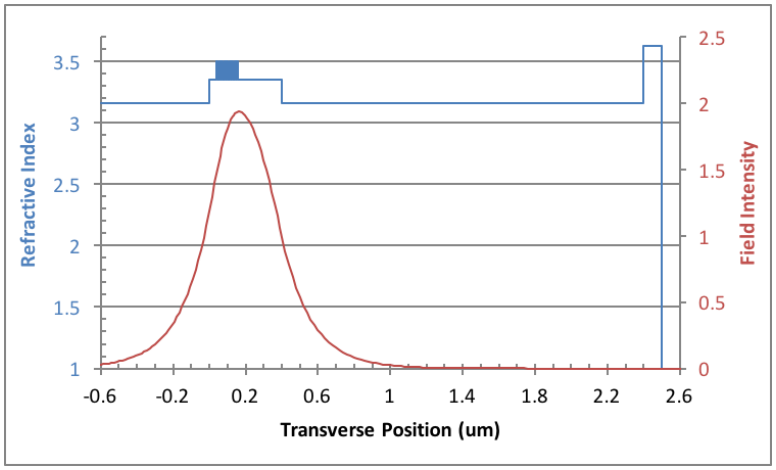

Figure 31. Index profile and transverse field intensity in the laser section for the 9-QW waveguide with the InGaAsP grating.

To ensure that the lateral mode can be supported in the laser gain region, the index difference between the ridge and groove in the lateral direction (y direction in Figure 30) should be in a range of 0.01 to 0.02 for InGaAsP/InP ridge guide lasers. As indicated in Figure 32, the effective index decreases as the thickness of the p-clad InP layer decreases. When the effective index difference is 0.01 (Δn) between the ridge and groove, the p-clad InP thickness is 0.22 μm in the grooves. Figure 32 also shows that the 9-QW confinement factor is 9.6% in the laser ridge. The QW confinement factor increases as the p-clad InP thickness decreases.

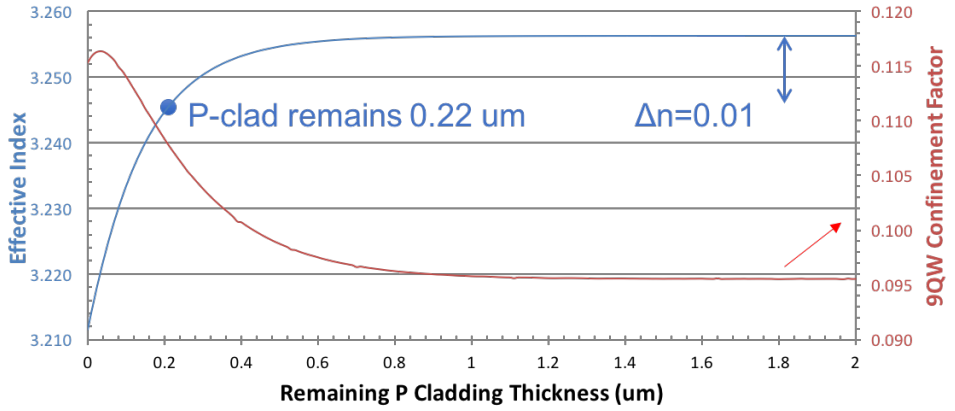

Figure 32. Effective index and QW confinement factor as a function of the remaining p cladding thickness for the 9-QW laser having the InGaAsP grating.

Figure 33(a) shows the lateral field intensities with variable lateral index differences in a range of 0.01 to 0.02 for a ridge width of 5 µm. As the index difference increases, the full width at half power (FWHP) of the near field decreases. In addition, the laser ridge might be undercut during the etching process, so the field intensity in a 4-µm ridge is also calculated in Figure 33(b).

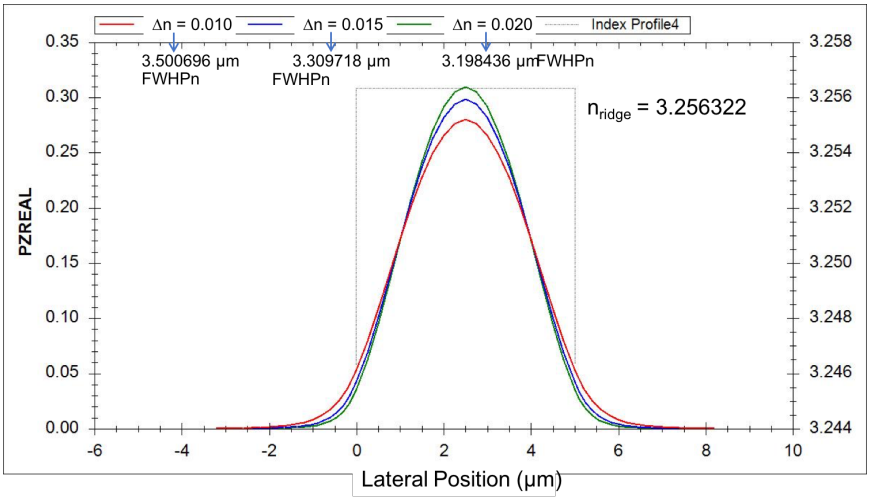

(a)

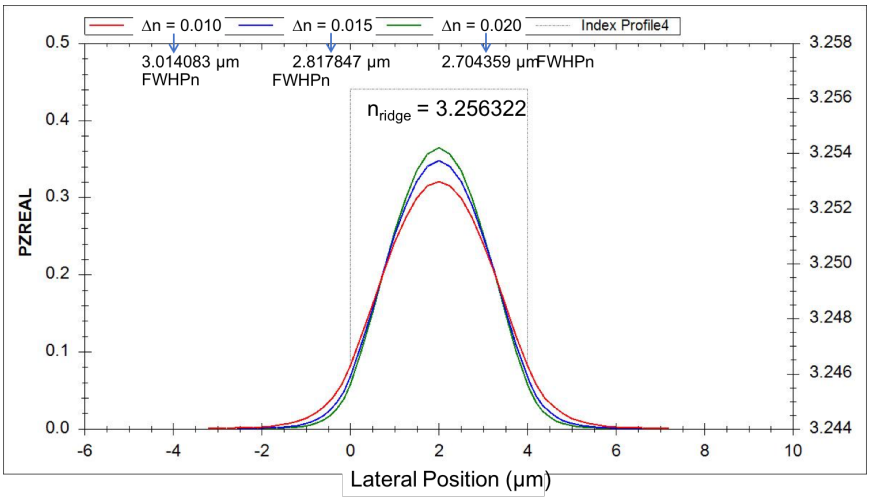

(b)

Figure 33. Lateral field intensity for a ridge width of (a) 5 µm and (b) 4 µm with variable index steps in a 9-QW waveguide.

3.1.1.2 Refractive Index Calculations in the Grating Region

The following analysis assumes a InGaAsP ECS grating coupler with a rectangular profile, a constant 50% duty cycle and a constant period as shown in Figure 34. The square grating is etched into InGaAsP (n_1=3.3511) followed by deposition of a thin SiO_2 liner (n_2=1.46) and an amorphous silicon cover layer (n_{Si}=3.476). The permittivity difference at the grating interface is:

$$n_1^2 - n_2^2 = 9.1 \tag{37}$$

The grating region is split into sections I, II, and III. The average refractive index of each section is calculated by taking the square root of the average relative permittivity of each section. Figure 34 illustrates what happens with a liner thickness of 5 nm and a grating period of 0.5 µm. Within a grating period Λ, the resulting layers are 50% InGaAsP (n_1) and 50% liner (n_2) in section I. Therefore, the average index of refraction in section I is

$$n_{ave}(section\ I) = \sqrt{50\% \times 3.3511^2 + 50\% \times 1.46^2} = 2.585 \quad (38)$$

Similarly, in section II, within a grating period Λ, the resulting layers are 50% InGaAsP (n_1), 48% cover layer (n_{Si}) and 2% liner (n_2) on the sidewalls due to

$$\frac{liner}{\Lambda} = \frac{5\ nm}{500\ nm} = 1\% \quad (39)$$

The average index of refraction in section II is

$$n_{ave}(section\ II) = \sqrt{50\% \times 3.3511^2 + 2\% \times 1.46^2 + 48\% \times 3.476^2} = 3.385 \quad (40)$$

Again, in section III, within a grating period Λ, the resulting layers are 50% liner (n_2), 48% cover layer (n_{Si}) and 2% liner (n_2). The average index of refraction in section III is

$$n_{ave}(section\ III) = \sqrt{52\% \times 1.46^2 + 48\% \times 3.476^2} = 2.628 \quad (41)$$

The electric fields in the transverse direction of the waveguide in Figure 34 are calculated by WAVEGUIDE III [35] using the equivalent average index of refraction of sections I, II and III (Equations (38), (40), and (41)) in the grating layers.

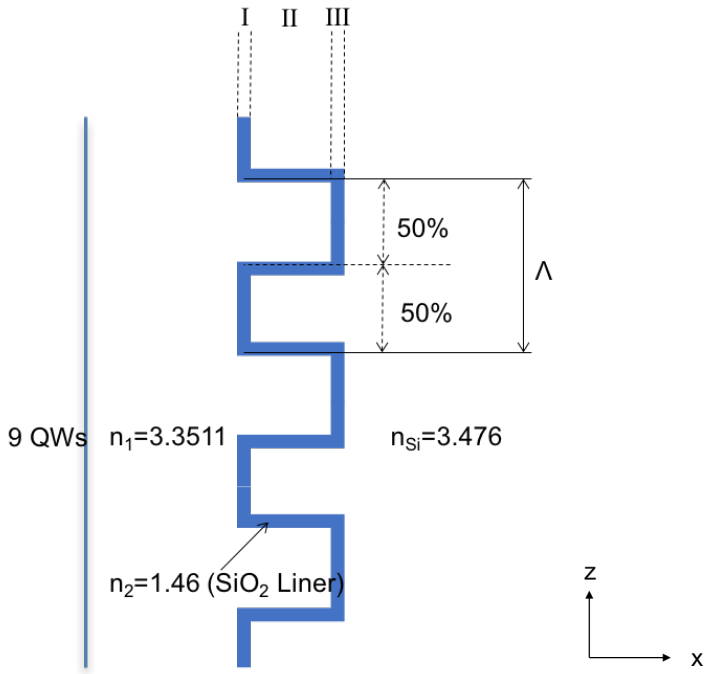

Figure 34. Illustration of the InGaAsP grating coupler with the liner and cover layer.

Table 4 provides the compositions, thicknesses and indices of the epitaxial layers of the grating section in the 9-QW laser waveguide. The indices of refraction of Grating 1, Grating 2 and Grating 3 are calculated from n_{ave}*(section I)*, n_{ave}*(section II)* and n_{ave}*(section III)*, respectively. The total thickness of Grating Section 1 to 3 is 0.2 μm, including the SiO_2 liner of 5 nm. An amorphous silicon layer is deposited on top of the liner layer and fills in the trenches between the grating teeth.

Table 4. Grating region of 9-QW laser waveguide having an InGaAsP grating.

Layer	Composition	Thickness (um)	Material Index
Air		--	1
A-Si	Amorphous Silicon	0.150	3.476
Grating 3	52% SiO_2+48% Si	0.005 (SiO_2 TL)	2.628
Grating 2	50% barrier(SCH)+2% SiO_2+48% Si	0.190	3.385
Grating 1	50% barrier(SCH)+50% SiO_2	0.005 (SiO_2 TL)	2.585
SCH	$In_{0.74}Ga_{0.26}As_{0.5}P_{0.5}$	0.041	3.35110
8x barriers	$In_{0.74}Ga_{0.26}As_{0.5}P_{0.5}$	0.008	3.35110
9x QWs	$In_{0.74}Ga_{0.26}As_{0.81}P_{0.19}$	0.006	3.50636
SCH	$In_{0.74}Ga_{0.26}As_{0.5}P_{0.5}$	0.041	3.35110
N substrate	InP	--	3.16492

3.1.1.3 Field overlaps

The cap layer and a portion of the p-clad layer are etched before the formation of a DBR grating or an outcoupler grating [30]. During fabrication, transition regions between the ridge laser region and the grating region are created, and reflections and radiation losses occur at these interface discontinuities. The reflectivity and radiation loss at an interface in a waveguide is proportional to $(1 - \kappa_x)$ [14]

$$\kappa_x = \frac{\left|\int_{-\infty}^{\infty} E_g(x)E_w^*(x)dx\right|^2}{\left(\int_{-\infty}^{\infty} E_g(x)E_g^*(x)dx \int_{-\infty}^{\infty} E_w(x)E_w^*(x)dx\right)} \tag{42}$$

where κ_x is the normalized overlap integral of fields on each side of the boundary, E_g is the electric field on one side of the boundary and E_w is the electric field on another side of the boundary. Overlap integrals greater than 0.9 are desirable for efficient lasers.

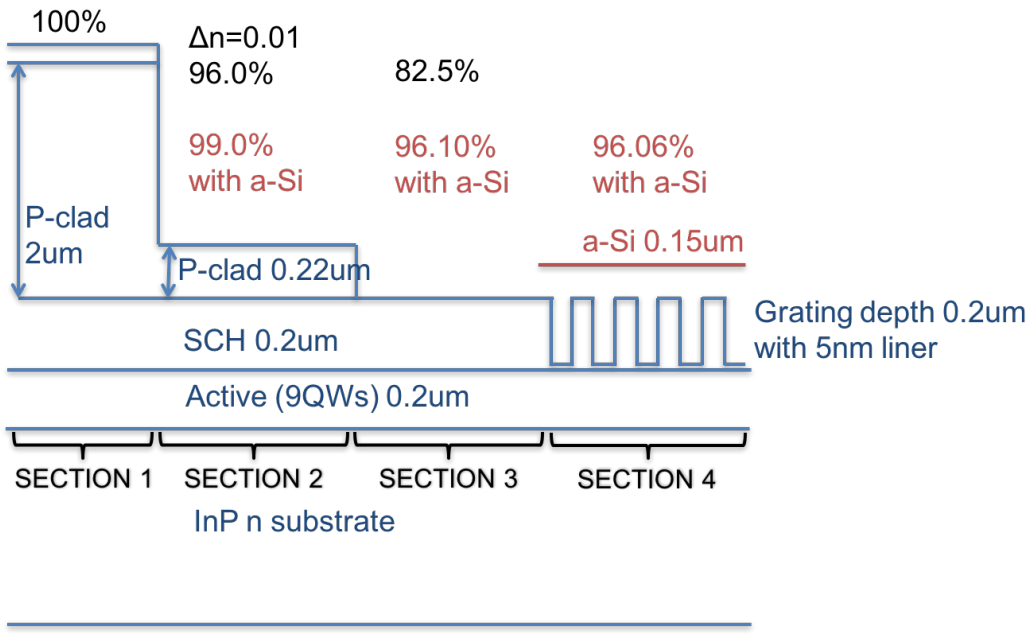

Figure 35. Cross section for the 9-QW laser waveguide with the InGaAsP grating.

Figure 35 shows a stepped cross section from a laser section, two transition regions, and an ECS outcoupler grating section. These stepped sections also refer to the device topology as shown in Figure 30. Laser section 1 corresponds to the epi layers tabulated in Table 3. Transition section 2 is the bottom of the laser ridge and the level of the top of the backside DBR grating. Transition section 3 is the top of the front-side outcoupler grating. The length of transition section 2 and 3 is generally on the order of 10 µm. Grating section 4 is the front-side outcoupler grating deposited with a liner and cover layer.

The overlap integrals of each section are indicated in Figure 35 as light propagates from laser section 1. The overlap integral of the fields between laser section 1 and transition section 2 is 96% without and 99% with an amorphous silicon layer. The overlap integral of the fields between laser section 1 and transition section 3 is 82.5%, which is much lower than the overlap of transition section 2. But by adding an amorphous silicon

cover layer of 150 nm, the overlap integral is boosted to 96%. The overlap integral of the fields between laser section 1 and grating section 4 is 96.06% with the deposition of a 5-nm SiO_2 liner and a 150-nm amorphous silicon layer. Without the liner a silicon cover layers, the waveguide in section 4 is cutoff—so the overlap would be 0%.

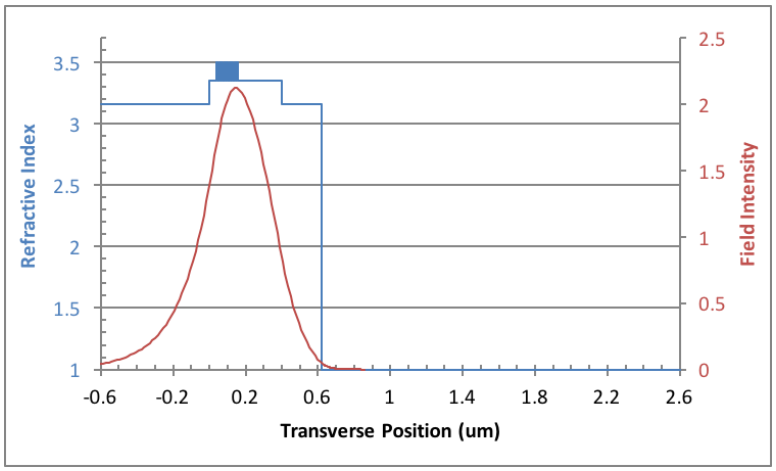

(a)

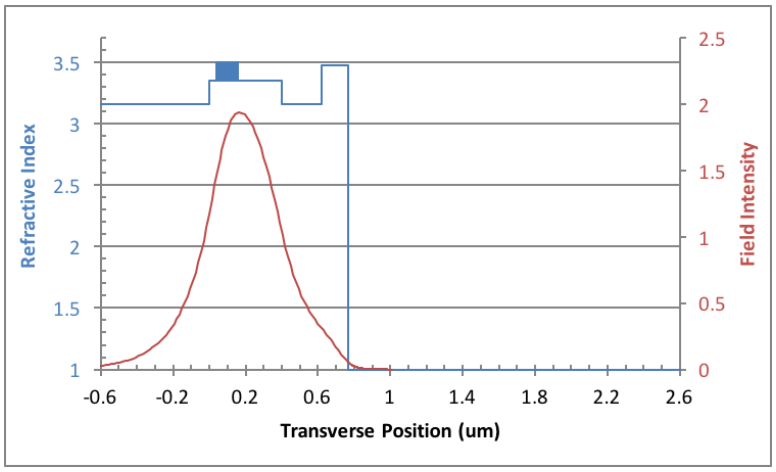

(b)

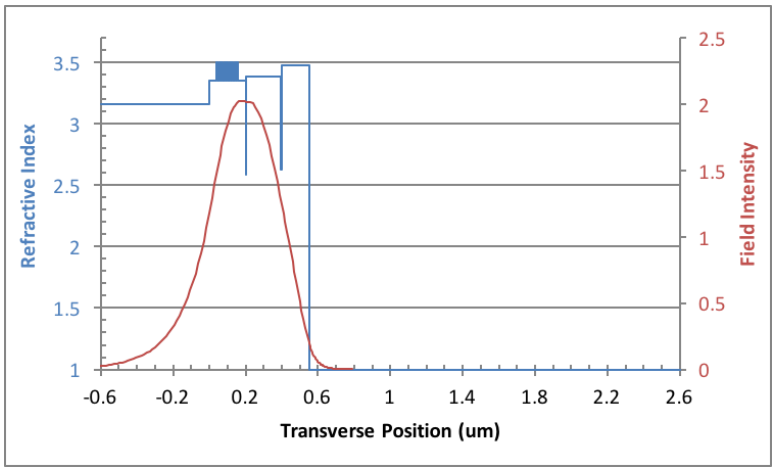

(c)

Figure 36. Field intensity in (a) transition section 2, (b) transition section 2 covered by the cover layer of 150 nm and (c) grating section 4 after the liner and cover deposition for the 9-QW waveguide.

In laser section 1, the field intensity and index profile are shown in Figure 31. Figure 36(a) shows the field intensity and index profile for transition section 2. Figure 36(b) shows the field intensity and index profile for transition section 2 with the amorphous silicon cover layer of 150 nm that improves the overlap integral. Figure 36(c) shows the field intensity and index profile in grating coupler section 4 with the 5-nm low-index liner and 150-nm high-index cover layer on top of the 0.2-μm grating.

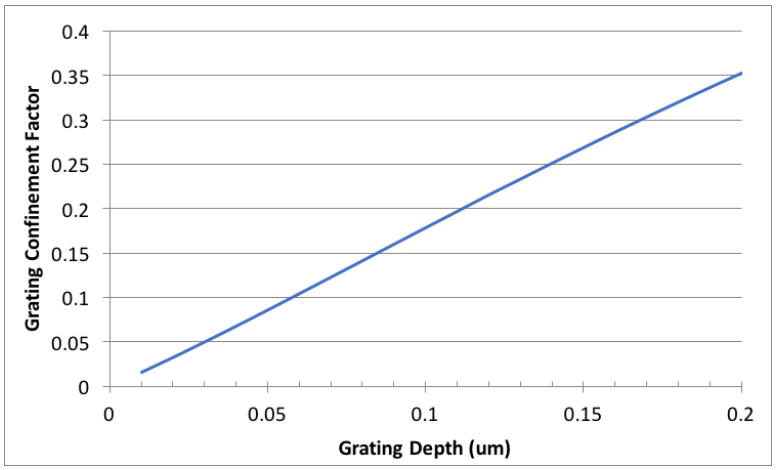

Figure 37. Grating confinement factor as a function of the InGaAsP grating depth.

The grating confinement factor as a function of the InGaAsP grating depth in the 9-QW laser waveguide is shown in Figure 37. Since the thickness of the InGaAsP layer for the grating is 0.2 μm, the grating depth is up to 0.2 μm. The grating confinement factor is proportional to the grating depth and is 0.353 for a 0.2-μm grating. The permittivity difference at the grating interface is calculated in equation (37). FoM_a is proportional to the grating confinement factor and the index difference. Therefore, FoM_a for this 0.2-μm InGaAsP grating is 3.21. Later we compare figure of merit of this InGaAsP grating to that of an InP grating.

3.1.1.4 Normalized propagation constants with variable liner thicknesses

We have analyzed the InGaAsP grating in a 9-QW structure by using a simple planar layer approach in the previous section. In this section, the numerical Floquet-Bloch approach is used to consider the interaction of the optical modes at the grating interfaces. In the Floquet-Bloch software, we establish the input waveguides to be the laser waveguide

tabulated in Table 3 followed by the InGaAsP grating waveguide tabulated in Table 4. The initial etched grating structure has a 50% duty cycle with a grating period of 500 nm for the second Bragg condition at a wavelength of 1550 nm.

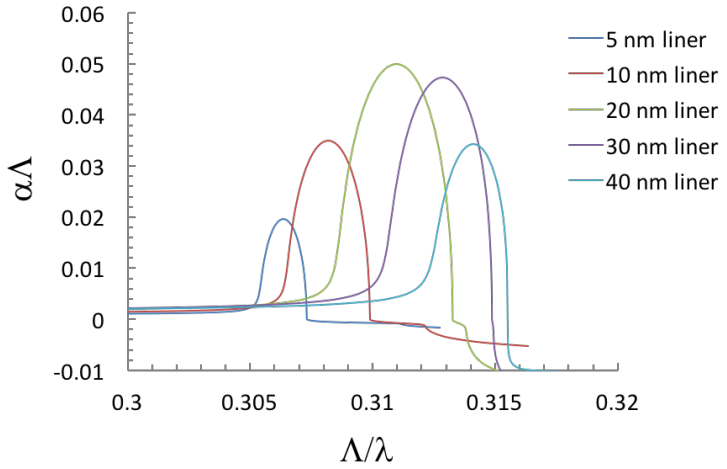

(a)

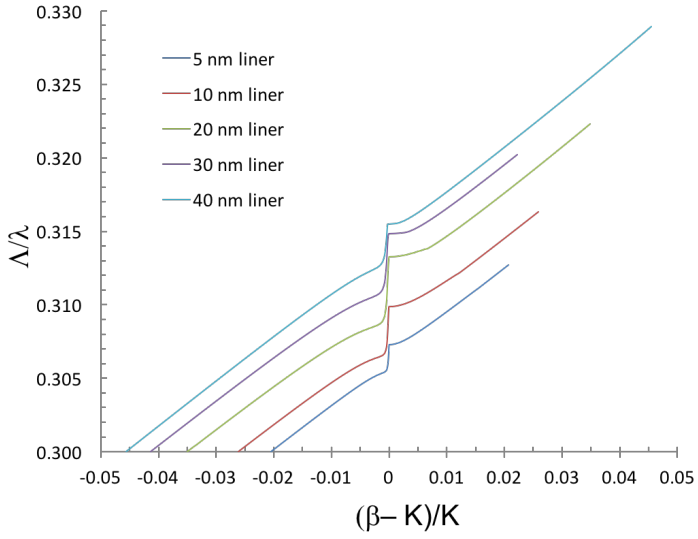

(b)

Figure 38. Normalized (a) imaginary part and (b) real part of the longitudinal propagation constant as a function of the normalized reciprocal wavelength for the InGaAsP grating structure with variable liner thicknesses.

Figure 38(a) shows the normalized imaginary part of the longitudinal propagation constant (or attenuation) ($\alpha\Lambda$) as a function of the normalized reciprocal wavelength (Λ/λ_0) with variable liner thicknesses. By increasing the liner thickness, the center of the normalized attenuation ($\alpha\Lambda$) curve also shifts to the different normalized reciprocal wavelength (Λ/λ_0). The highest peak of the normalized attenuation ($\alpha\Lambda$) is 0.05 at Λ/λ_0=0.311 for the liner thickness of 20 nm as shown in Figure 39. Figure 38(b) shows the normalized real part of the longitudinal propagation constant ((β-K)/K) as a function of the normalized reciprocal wavelength (Λ/λ_0). The second Bragg condition occurs at ((β-K)/K) = 0. As the liner thickness increases, the center of the normalized wavelength shifts for a fixed grating period. These normalized propagation constants are calculated for a grating having an infinite length.

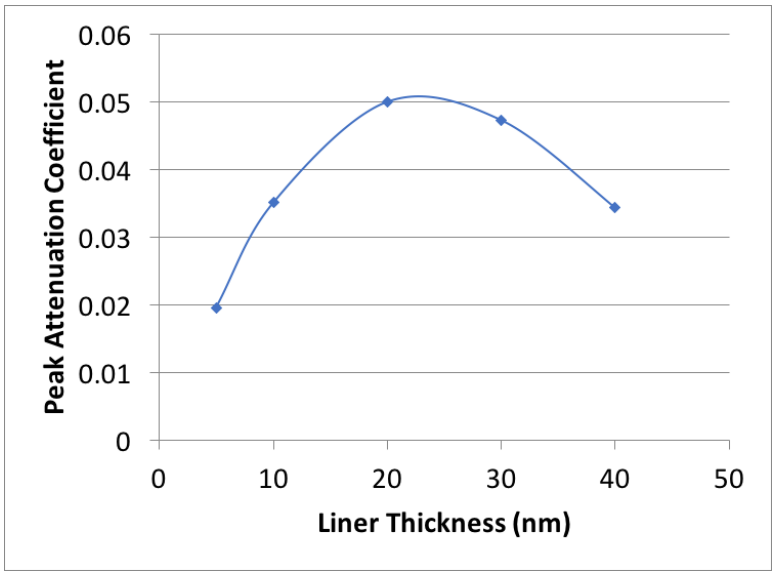

Figure 39. Attenuation peak as a function of liner thickness for the thick SCH laser.

3.1.2. InP Grating Coupler

Table 5 indicates the compositions, layer thicknesses and indices of refraction in a laser section for a 9-QW waveguide with an InP grating. The indices of refraction are calculated at a wavelength of 1550 nm. The active region consists of the same 9 QWs and 8 barriers sandwiched by two SCH layers as in the previous section. The sum of the layers in the core region is 0.2 μm. After the InGaAs cap layer and partial p cladding layer are etched, the grating is formed in the p-clad InP layer.

Table 5. 9-QW laser structure designed for an InP Grating (thin SCH).

Layer	Composition	Thickness (um)	Material Index
Air		--	1
Cap	InGaAs	0.100	3.62525
P-clad	InP	2	3.16492
SCH	$In_{0.74}Ga_{0.26}As_{0.5}P_{0.5}$	0.041	3.35110
8x barriers	$In_{0.74}Ga_{0.26}As_{0.5}P_{0.5}$	0.008	3.35110
9x QWs	$In_{0.74}Ga_{0.26}As_{0.81}P_{0.19}$	0.006	3.50636
SCH	$In_{0.74}Ga_{0.26}As_{0.5}P_{0.5}$	0.041	3.35110
N substrate	InP	--	3.16492

3.1.2.1 Field intensity in the gain region

Figure 40 shows the refractive index profile and field intensity in the transverse direction for the 9-QW laser as tabulated in Table 5. These QWs are centered in the InGaAsP SCH layers.

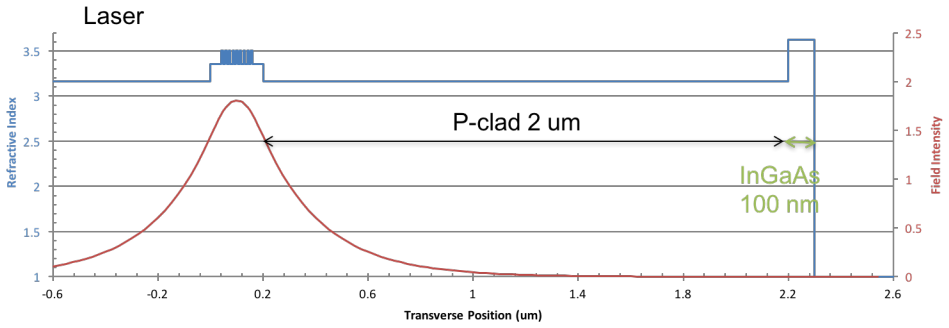

Figure 40. Index profile and transverse field intensity in the laser section for the 9-QW waveguide with the InP grating.

In order to support the field mode in the InGaAsP/InP laser gain region, it is necessary that the lateral index difference (Δn) is in a range of 0.01 to 0.02. As indicated in Figure 41, the effective index decreases as the thickness of the p-clad InP layer decreases. When the effective index difference is 0.01 (Δn) between the ridge and the groove, the p-clad InP is 0.38 μm in the groove and the p-clad InP is 2 μm in the ridge. Figure 41 also shows that the 9-QW confinement factor is 9.5% in the laser ridge; the QW confinement factor decreases as the p-clad InP thickness decreases. The QW confinement factor curve is different from the InGaAsP grating in Figure 32.

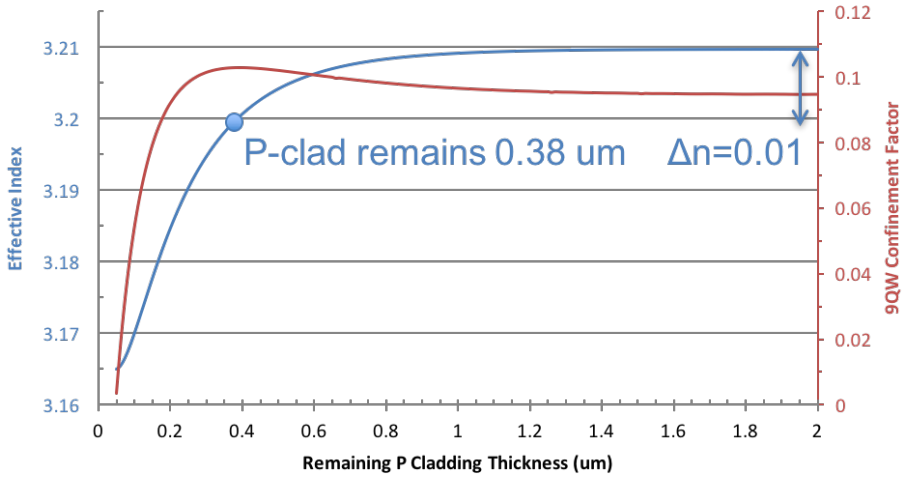

Figure 41. Effective index and QW confinement factor for the 9-QW laser having the InP grating.

3.1.2.2 Refractive index calculations for the InP grating case

The following analysis assumes an InP ECS grating coupler with a rectangular profile, a constant 50% duty cycle, a constant period and a uniform depth as shown in Figure 42. The square grating is etched in InP (n_1=3.16492), and a thin SiO_2 liner (n_2=1.46) and an amorphous silicon cover layer (n_{Si}=3.476) are deposited. The permittivity difference at the grating interface is:

$$n_1^2 - n_2^2 = 7.89 \tag{43}$$

The grating region is split into sections I, II, and III. The average refractive index of each section is calculated by taking the square root of the average relative permittivity of each section. Figure 42 illustrates what happens with a liner thickness of 5 nm and a grating period of 0.5 μm. Within a grating period Λ, the resulting layers are 50% InP (n_1) and 50% liner (n_2) in section I. Therefore, the average index of refraction in section I is

$$n_{ave}(section\ I) = \sqrt{50\% \times 3.14492^2 + 50\% \times 1.46^2} = 2.465 \tag{44}$$

Similarly, in section II, within a grating period Λ, the resulting layers are 50% InP (n_1), 48% cover layer (n_{Si}) and 2% liner (n_2) on the sidewalls. The average index of refraction in section II is

$$\begin{aligned} n_{ave}(section\ II) &= \sqrt{50\% \times 3.16492^2 + 2\% \times 1.46^2 + 48\% \times 3.476^2} \\ &= 3.294 \end{aligned} \tag{45}$$

Again, in section III, within a grating period Λ, the resulting layers are 50% liner (n_2), 48% cover layer (n_{Si}) and 2% liner (n_2). The average index of refraction in section III is

$$n_{ave}(section\ III) = \sqrt{52\% \times 1.46^2 + 48\% \times 3.476^2} = 2.628 \qquad (46)$$

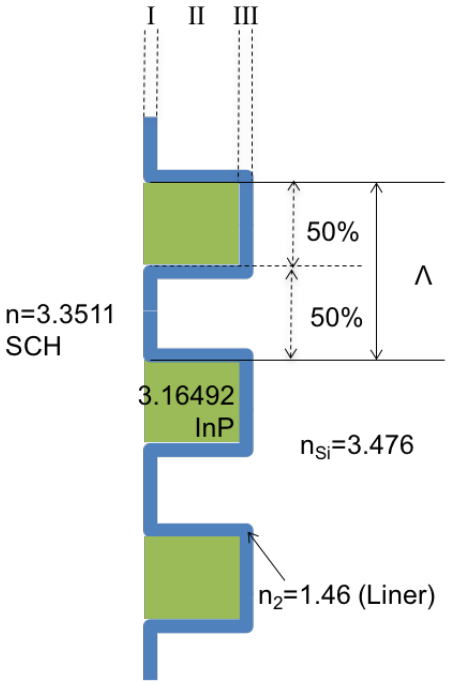

Figure 42. Illustration of the InP grating covered by a liner and a cover layer.

Table 6 illustrates the epitaxial table of the InP grating section in the 9-QW laser waveguide. The indices of refraction of grating 1, grating 2 and grating 3 are calculated from n_{ave}*(section I)*, n_{ave}*(section II)* and n_{ave}*(section III)*, respectively. Total thickness of grating 1 to 3 is 0.2 μm including a SiO_2 liner of 5 nm. An amorphous silicon layer is deposited on top of the grating and fills in the trenches between the grating teeth.

Table 6. Grating section in the 9-QW waveguide with the InP grating coupler.

Layer	Composition	Thickness (um)	Material Index
Air		--	1
A_Si	Amorphous Silicon	0.150	3.476
Grating 3	52% SiO_2+48% Si	0.005 (SiO_2 TL)	2.628
Grating 2	50% InP+2% SiO_2+48% Si	0.190	3.294
Grating 1	50% InP+50% SiO_2	0.005 (SiO_2 TL)	2.465
SCH	$In_{0.74}Ga_{0.26}$ $As_{0.5}P_{0.5}$	0.041	3.35110
8x barriers	$In_{0.74}Ga_{0.26}$ $As_{0.5}P_{0.5}$	0.008	3.35110
9x QWs	$In_{0.74}Ga_{0.26}$ $As_{0.81}P_{0.19}$	0.006	3.50636
SCH	$In_{0.74}Ga_{0.26}$ $As_{0.5}P_{0.5}$	0.041	3.35110
N substrate	InP	--	3.16492

3.1.2.3 Field overlaps

Figure 43 shows a cross section from a laser section, two transition regions, and an ECS outcoupler grating section. These stepped sections refer to the device shown in Figure 30. Laser section 1 corresponds to the epi layers tabulated in Table 5. Transition section 2 corresponds to the depth of the laser ridge. Transition section 3 corresponds to the top of the outcoupler grating. The length between transition sections 2 and 3 is typically on the order of 10 μm. Grating section 4 is the InP outcoupler grating deposited with a liner and cover layer.

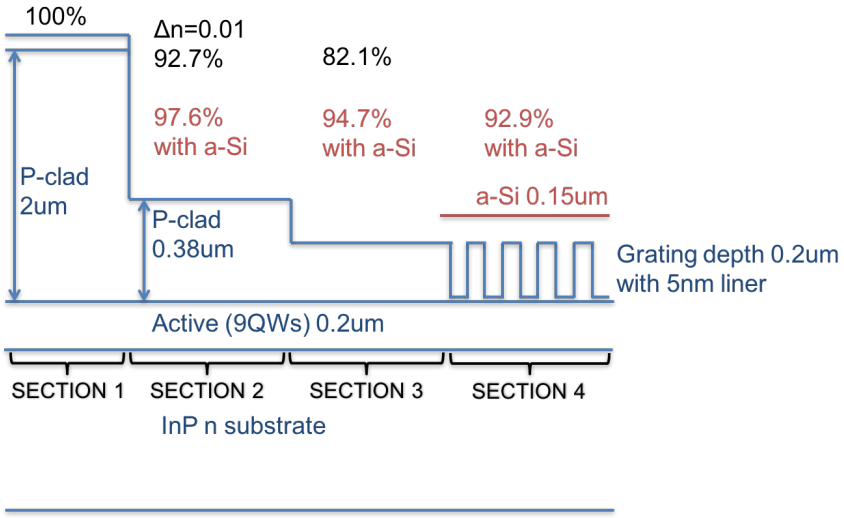

Figure 43. Cross section of the 9-QW laser waveguide with the InP grating.

The overlap integrals of each section are indicated in Figure 43 as light propagates from laser section 1. The overlap integral of the fields between laser section 1 and transition section 2 is 92.7%. The overlap integral of the fields between laser section 1 and transition section 3 is 82.1%. This is much lower than the overlap of transition section 2; however, by adding an amorphous silicon cover layer of 150 nm, the overlap integral is enhanced to 94.7% in transition section 3. The overlap integral of the fields between laser section 1 and grating section 4 is 92.9%. Grating section 4 is where a 5-nm SiO_2 liner and 150-nm amorphous silicon layer are deposited. In contrast with the overlap integrals of the InGaAsP grating waveguide as shown in Figure 35, the overlap integrals of the InP grating is small.

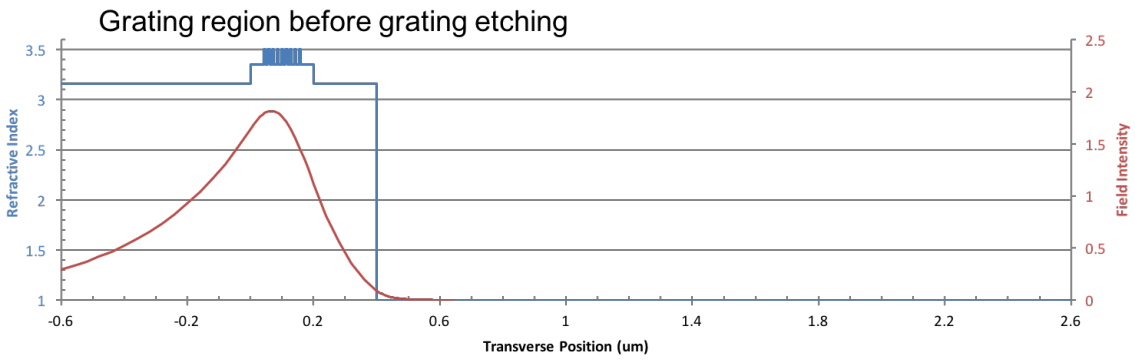

(a)

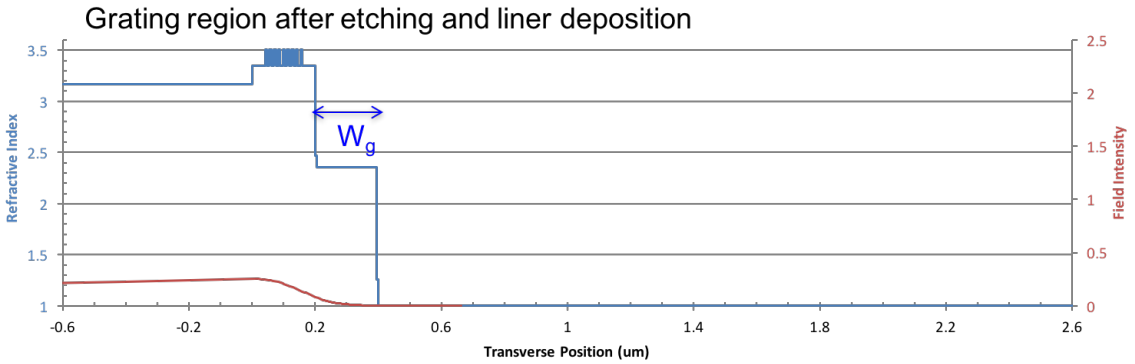

(b)

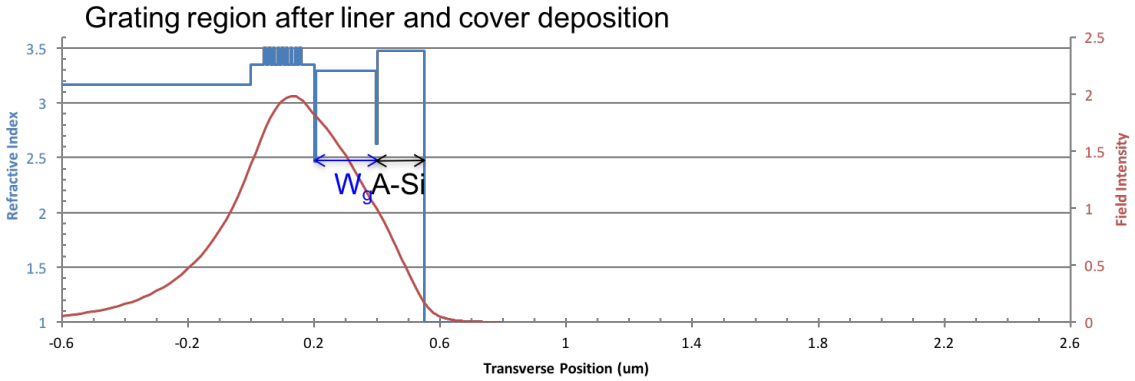

(c)

Figure 44. Field intensity and index profile in (a) transition section 3, (b) grating section 4 after liner deposition and (c) grating section 4 with liner and cover layers.

Moreover, the overlap integral indicates how well the normalized field intensities between sections are overlapped. The field intensity and index profile in laser section 1 are shown in Figure 40. Figure 44(a) shows the field intensity and index profile for where transition section 3 is ready for the grating etching. Figure 44(b) shows the field intensity and index profile for grating section 4 with a low-index liner layer of 5 nm that pushes the field toward to the substrate. Figure 44(c) shows the field intensity and index profile in grating section 4 with a 5-nm low-index liner and 150-nm high-index cover layer on top of the 0.2-μm grating. By adding a high-index amorphous silicon, the field is pulled from the substrate into the active and grating region; that increases the overlap integral in the grating region.

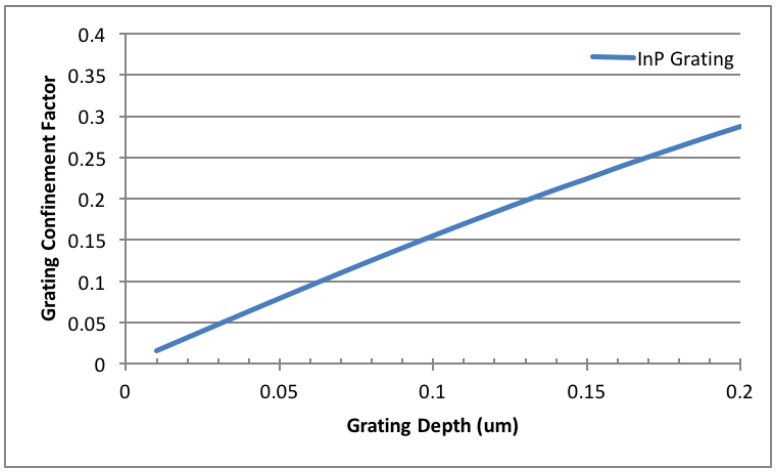

Figure 45. Grating confinement factor for a InP grating coupler.

The grating confinement factor as a function of the InP grating depth in the 9-QW laser waveguide is shown in Figure 45. The grating confinement factor is proportional to the grating depth. As the grating depth is 0.2 μm, the grating confinement factor is 0.288,

which is lower than the one of the InGaAsP grating as discussed in section 3.1.1.3. In addition, the permittivity difference at the InP grating interface is calculated in equation (43). FoM_a is proportional to the grating confinement factor and the index difference. Thus, FoM_a is 2.27 for the InP grating as indicated in Table 7. Since the InP grating has a low permittivity difference and grating confinement factor, FoM_a of the InP grating is lower than FoM_a of the InGaAsP grating.

Table 7. Properties for the thick SCH (InGaAsP grating) and thin SCH (InP grating) structure.

	thick SCH	thin SCH
W_g (um)	0.2	0.2
Λ (um)	0.5	0.5
Δn_{sub}	0.19	0.19
n_1^2-n_2^2	9.10	7.89
$\Gamma_{grating}$	35.3%	28.8%
FOM_a	3.21	2.27

3.1.2.4 Normalized Propagation Constants with Variable Liner Thicknesses

The InP grating structure has been analyzed by using a simple planar layer approach. In this section, the numerical Floquet-Bloch analysis is employed. The Floquet-Bloch software establishes the input waveguide to be the laser waveguide in Table 5 followed by the grating waveguide to be the InP grating in Table 6. The grating structure is a 50% duty cycle with the initial grating period of 500 nm for the second Bragg condition in the wavelength of 1550 nm.

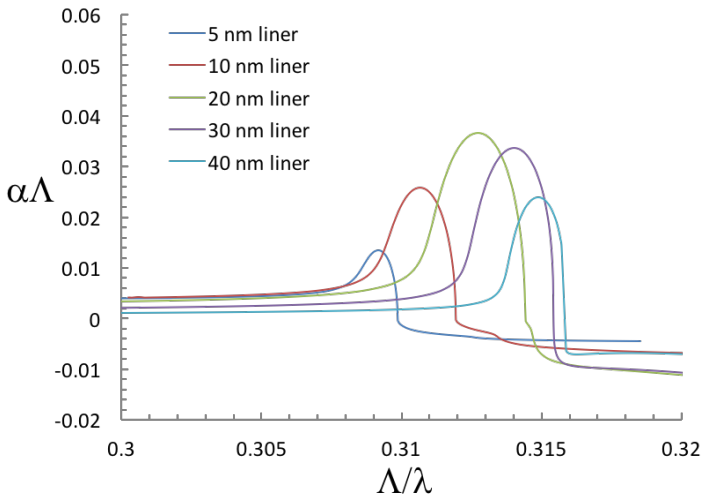

(a)

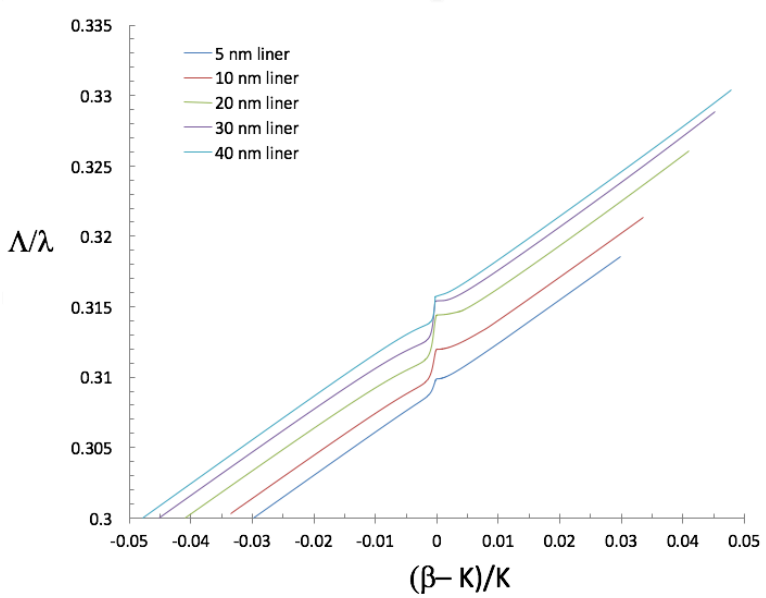

Figure 46. Normalized (a) imaginary part and (b) real part of the longitudinal propagation constant as a function of the normalized reciprocal wavelength for the InP grating structure with variable liner thicknesses.

Figure 46(a) shows the normalized attenuation ($\alpha\Lambda$) as a function of the normalized reciprocal wavelength (Λ/λ_0) with variable liner thicknesses. By increasing the liner thickness, the center of the normalized attenuation ($\alpha\Lambda$) also shifts to the different normalized reciprocal wavelength (Λ/λ_0). The highest peak of the normalized attenuation ($\alpha\Lambda$) is 0.037 at Λ/λ_0=0.313 for a liner thickness of 20 nm as shown in Figure 47. Figure 46(b) shows the normalized real part of the longitudinal propagation constant ((β-K)/K) as a function of the normalized reciprocal wavelength (Λ/λ_0). The steep portion of the curves locates near ((β-K)/K) = 0. When the liner thickness increases, the center of the normalized wavelength changes. Figure 47 indicates that the attenuation coefficient of the InGaAsP grating is higher than the one for the InP grating. These normalized propagation constants are calculated for an infinitely long grating.

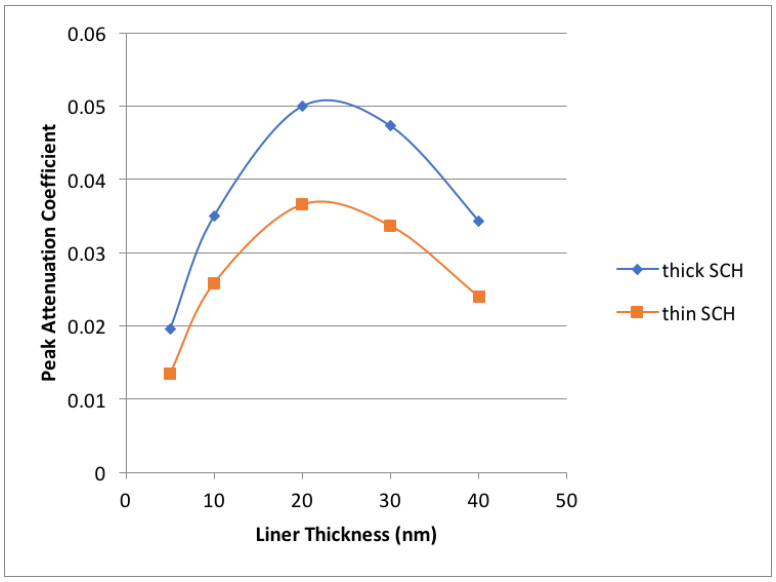

Figure 47. Attenuation peak as a function of a liner thickness for the InGaAsP grating (thick SCH) and InP grating (thin SCH).

3.1.3. Summary

The properties of the InGaAsP and InP grating coupler embedded in the 9-QW laser waveguide have been discussed. By using the simple planar layer approach, the grating confinement factor, FoM_a and field overlap integrals of the InGaAsP grating are better than the ones of the InP grating. By using the numerical Floquet-Bloch approach, the normalized attenuation coefficient of the InGaAsP grating is higher than the one for the InP grating; that implies larger radiated power from the InGaAsP grating coupler than the InP grating coupler. Overall, the InGaAsP grating coupler is the preferred design.

3.2. 9QW Structure Optimization

The ECS grating project was initially undertaken with Oracle on a silicon photonics DARPA program. Our joint goal was to achieve efficient hybrid lasers with a laser length of 50 to 100 μm long. Such a short gain length suggested the use of 9 QWs to obtain sufficient gain in such a short distance.

In previous two sections, we compared the attenuation coefficient and the power radiation for 9-QW ECS structures for fixed liner and cover layers. The epitaxial layers of the 9-QW structures are indicated in Table 3 and Table 4 (thick SCH layers), and Table 5 and Table 6 (thin SCH layers).

The previous two sections also show that embedding an outcoupler grating in InGaAsP has higher efficiency than embedding a grating in InP, which in retrospect appears obvious because of the larger index step between InGaAsP and silicon dioxide compared to the index step between InP and silicon dioxide.

3.2.1. Optimization of the Amorphous Si Cover Layer Thickness

Figure 48 shows the ECS grating for the 9-QW laser structure with the thick SCH layers. The core layer includes 9-QWs, 8 barriers and both SCH layers (Table 3) with a thickness of 0.2 μm (W_{core}). The grating is etched 100 nm (W_{etch}) deep in InGaAsP, followed by the deposition of a thin SiO_2 liner (d = 30 nm) and an amorphous Si cover layer. The total grating depth (W_g) is 130 nm including the etched grating depth (W_{etch}) and the liner thickness (d). The grating period (Λ) is 500 nm with a 50% duty cycle. The thickness of the amorphous Si cover layer is varied to optimize the normalized attenuation coefficient.

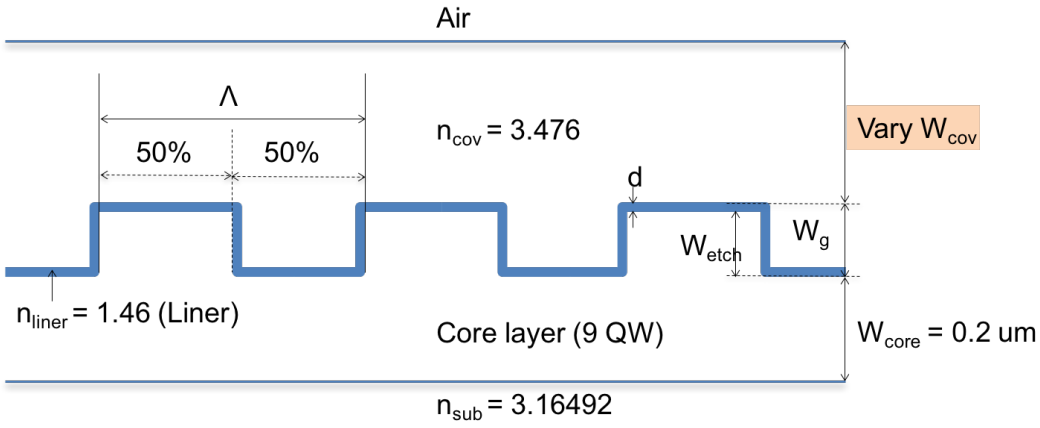

Figure 48. Sketch of the 9-QW ECS grating for varying the thickness of the cover layer.

Figure 49 shows the field intensity and index profile with variable amorphous Si cover thicknesses for the 9-QW ECS grating outcoupler. As shown in Figure 49 (a, b and c), as the thickness of the cover layer is increased above 200 nm, the field intensity is shifted from the core "sub-waveguide" towards the cover "sub-waveguide". This shift of the field intensity towards the cover "subwaveguide" not only increases the grating

confinement factor, but reduces the QW confinement, reducing the optical losses due to band to band absorption.

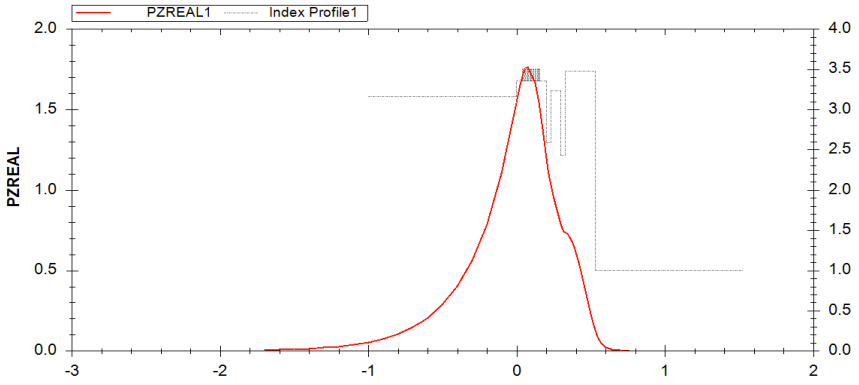

(a)

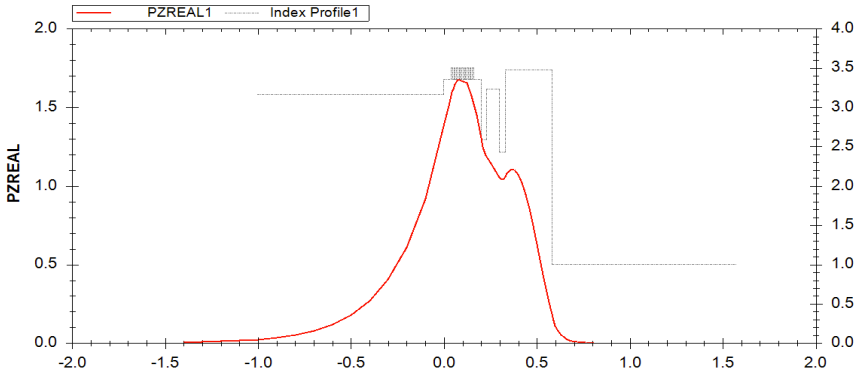

(b)

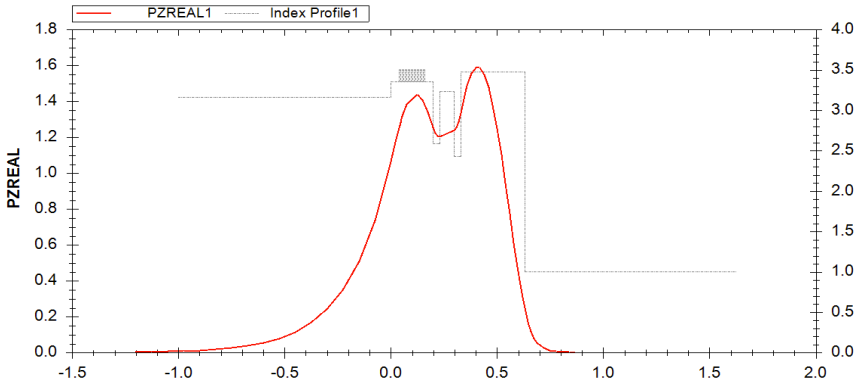

(c)

Figure 49. Field intensity and index profile with the (a) 200 nm, (b) 250 nm, and (c) 300 nm cover layer

Figure 50 shows the normalized attenuation peak as a function of the cover thickness. The value of the normalized attenuation peak is captured from the peak of the normalized attenuation spectrum for each cover layer thickness. From Figure 50, optimum values of the cover thickness are in the range of 200 to 400 nm.

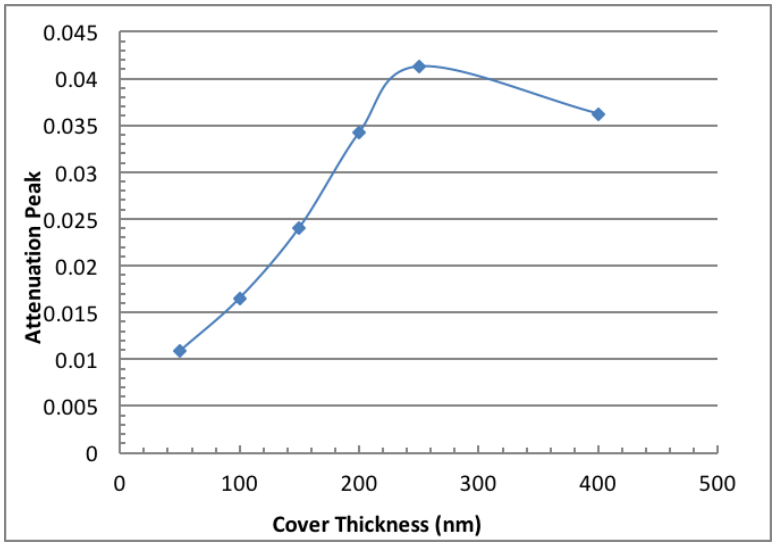

Figure 50. Attenuation peak as a function of the cover thickness.

The plots in Figure 51 show the normalized reciprocal wavelength (Λ/λ_0) as a function of both the normalized propagation constant ((β-K)/K) and the normalized attenuation ($\alpha\Lambda$) for a core thickness of 200 nm, liner layer thickness of 30 nm and a cover layer thickness of 200 nm. The plots are calculated for an infinite grating in the 9-QW ECS waveguide by the Floquet-Bloch approach and assume the wavelength in free space is 1550 nm (λ_0) for a varying grating period (Λ). The plots could also assume a fixed Bragg grating period (Λ_B) with a varying free-space wavelength. However, the latter case would

not be exactly correct, since the refractive index of each layer would change very slightly with wavelength. In either case, the Bragg grating period (Λ_B) is 486.6 nm and the peak of the normalized attenuation is 0.034 at $\Lambda/\lambda_0 = 0.313$. From

$$L = N\Lambda = \frac{1}{2\alpha} \tag{47}$$

the distance where the intensity in the grating waveguide reduced to e^{-1} is 7.135 μm. Note that points (E) and (F) in Figure 51 correspond to wavelengths shorter than the second Bragg condition, while points (A), (B) and (C) correspond to wavelengths longer than the 2nd Bragg condition.

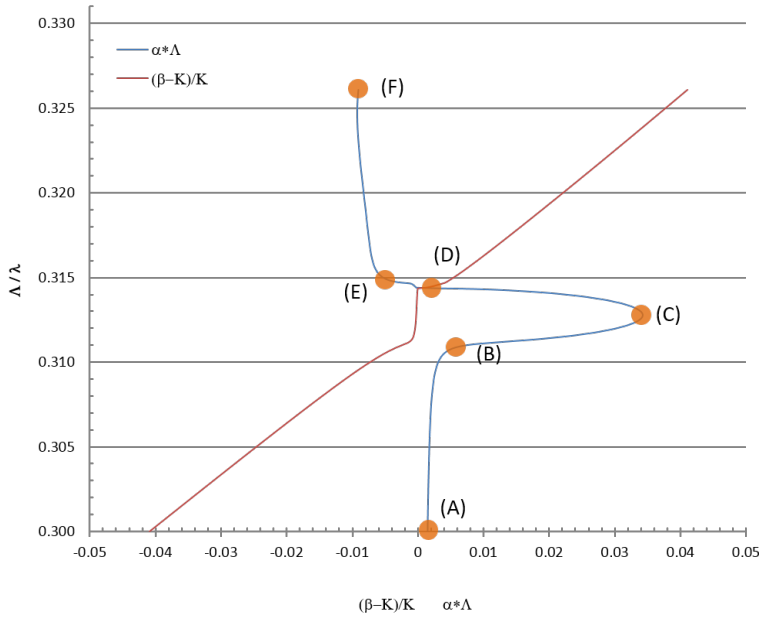

Figure 51. Normalized attenuation and propagation constant for the 9-QW ECS grating with a cover layer of 200 nm.

Figure 52(a) through (f) show the intensity distribution in an infinitely long 9-QW ECS grating with a 200-nm amorphous silicon cover layer at variable normalized wavelengths (Λ/λ_0) corresponding to points (A) through (F) indicated in Figure 51. The

top white lines in the colored plots indicate the teeth and grooves of the grating period with the bottom horizontal line indicating the bottom of the n-side SCH layer of the core layer. Figure 52(a) shows the intensity distribution at $\Lambda/\lambda_0 = 0.3$ where the grating period is far away from the Bragg condition with an almost uniform waveguide intensity. Figure 52(b) shows a periodic intensity distribution at point (B) in Figure 51 with the peak of the normalized attenuation in the center of the grating tooth and groove. Figure 52(c) shows the intensity distribution at point (C) in Figure 51 corresponding to the maximum normalized attenuation with the peak intensity shifted to one side of the grating tooth and groove. Figure 52(d) shows the intensity distribution near the 2^{nd} Bragg condition ($\alpha\Lambda \sim 0$) at point (D) in Figure 51 with the intensity peaks located at the edges of the grating teeth. Figure 52(e) shows the intensity distribution at $\Lambda/\lambda_0 = 0.3145$ point (E) in Figure 51 with a similar intensity distribution to that shown in Figure 51(D). Figure 52(F) shows the intensity distribution at $\Lambda/\lambda_0 = 0.3261$ where the grating period is farther away from the Bragg condition. For wavelengths longer than the second Bragg condition, the intensity peaks are contained within the teeth and grooves, while for shorter wavelengths, the intensity peaks tend to be centered at the boundaries between the teeth and grooves.

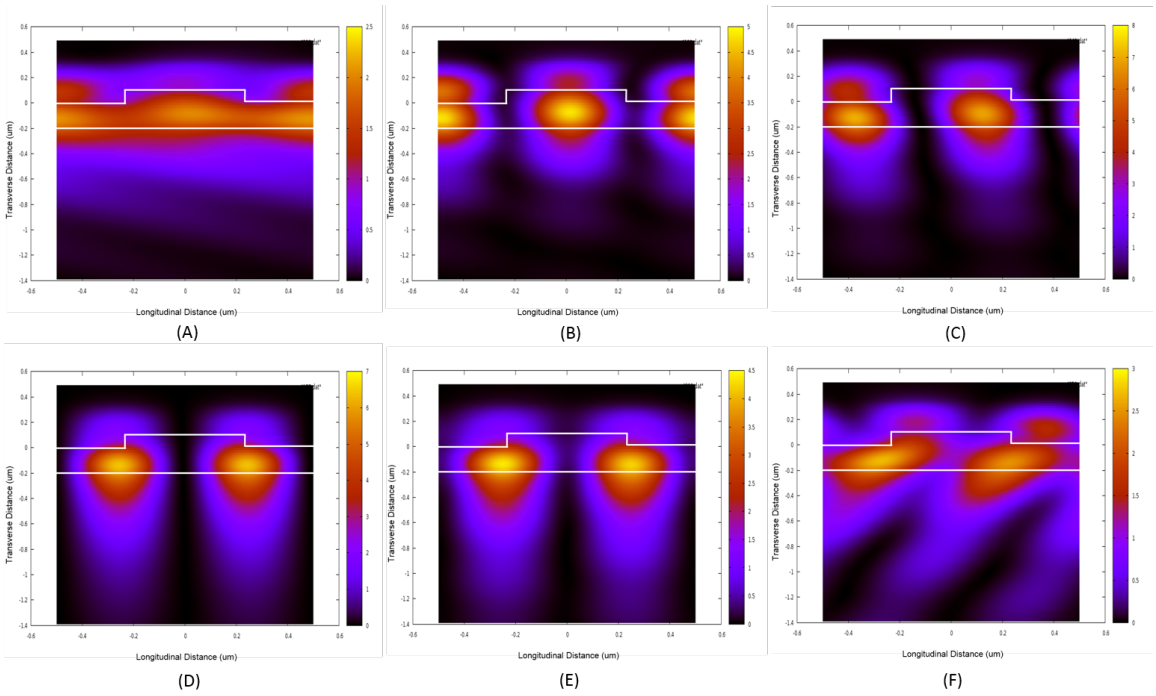

Figure 52. Plots of the 2D field distribution for the 9-QW ECS grating with a cover layer of 200 nm at variable wavelengths.

3.2.2. Optimization of the Liner Thickness

Optimum thicknesses of the amorphous silicon cover layer was determined for the ECS grating outcoupler for the 9-QW laser structure from the plot in Figure 50. The optimum thicknesses of an SiO_2 liner (layer d in Figure 48) for a cover layer thickness of 20 nm was determined from the plot in Figure 47.

Figure 53 shows the maximum normalized attenuation coefficient as a function of an SiO_2 liner thickness for a cover layer thickness of 200 nm. The value of the maximum normalized attenuation is obtained from the peak of the normalized attenuation spectrum for each liner thickness. For a liner thickness of 27 nm and a cover layer thickness of 200 nm, the maximum normalized attenuation coefficient is 0.0346.

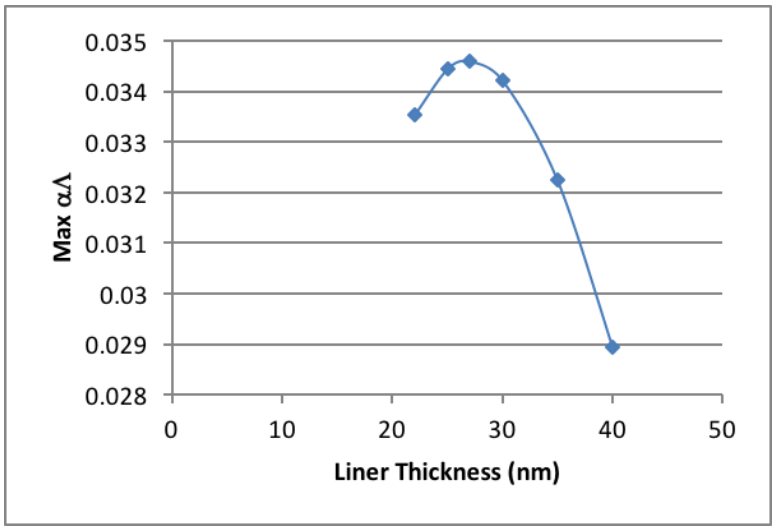

Figure 53. Attenuation peak as a function of liner thickness for the 9-QW ECS grating with a cover layer thickness of 200 nm and core thickness of 200 nm.

Figure 54 shows the normalized reciprocal wavelength (Λ/λ_0) as a function of the normalized propagation constant ($(\beta-K)/K$) and the normalized attenuation coefficient ($\alpha\Lambda$) for an infinite grating length. The Bragg grating period (Λ_B) is 486.6 nm and the peak of the normalized attenuation is 0.035 at $\Lambda/\lambda_0 = 0.312$. From

$$L = N\Lambda = \frac{1}{2\alpha} \tag{11}$$

the length of the grating required to reduce the intensity of transmitted light to e^{-1} (or ~ 0.37) is 6.9 μm.

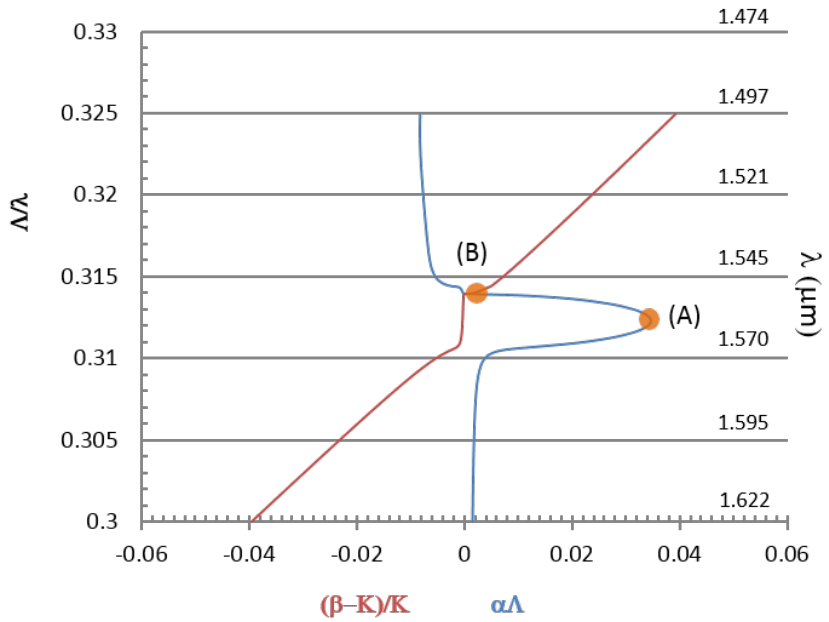

Figure 54. Normalized attenuation and propagating constant for the 9-QW ECS grating with a 27-nm liner.

Figure 55(a) and (b) show the intensity distribution in an infinitely long grating with a 27-nm liner layer and a 200-nm cover layer at variable normalized wavelengths (Λ/λ_0) corresponding to points (A) and (B) indicated in Figure 54. The upper white lines in the colored plots outline the "teeth" and grooves of a grating period and the lower horizontal line indicates the bottom of the n-side SCH layer of the core layer. Figure 55(a) shows the intensity distribution at point (A) in Figure 54 corresponding to the maximum normalized attenuation with the intensity peaks located within the grating teeth. Figure 55(b) shows the intensity distribution near the 2nd Bragg condition ($\alpha\Lambda \sim 0$) at point (B) in Figure 54 with the intensity peaks located at edges of the grating teeth.

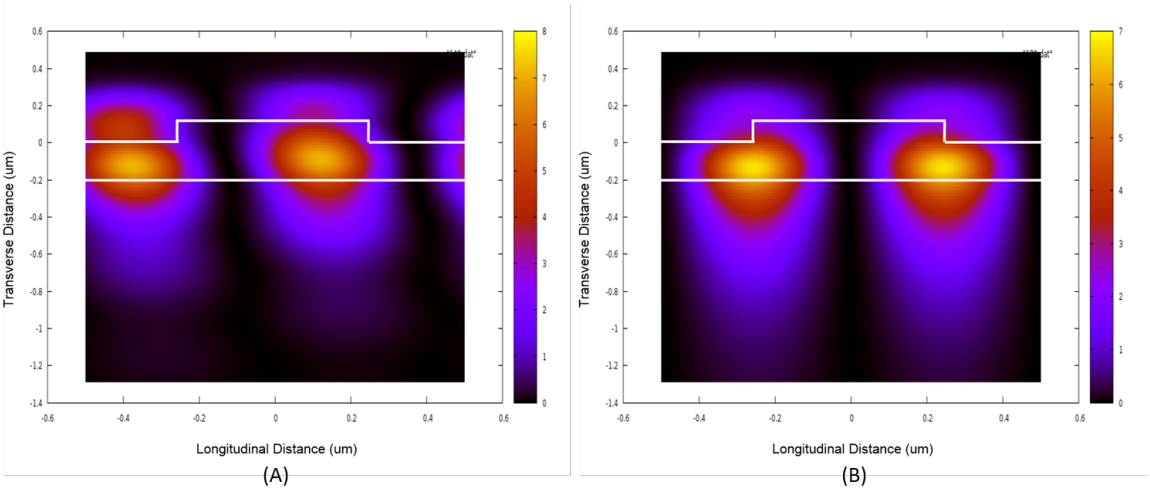

Figure 55. 2D field distribution of the ECS grating with the 27-nm liner at different wavelengths.

3.2.3. Optimization of the Core Thickness

The optimized thicknesses of an SiO_2 liner and amorphous silicon cover layer for a 9-QW grating structure have been previously determined. Next the optimized thickness of the core layer (W_{core} in Figure 48) is determined by optimizing the normalized attenuation coefficient with an optimized liner layer of 27 nm and optimized cover layer of 200 nm.

Figure 56 shows the maximum normalized attenuation coefficient as a function of the core layer thickness. The value of the maximum normalized attenuation is obtained from the peak of the normalized attenuation spectrum for each core thickness. At a core layer thickness of 150 nm, the maximum normalized attenuation coefficient is 0.0363. Because of the thicknesses of the barriers and quantum wells, the core layer thickness is limited to 118 nm.

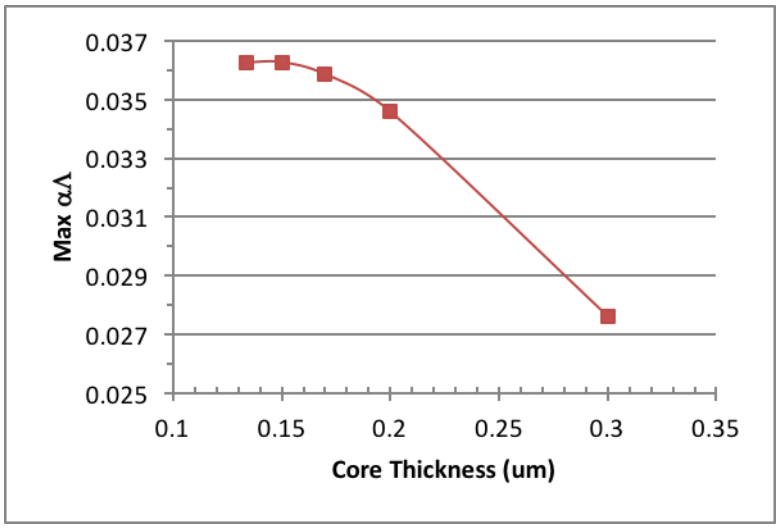

Figure 56. Attenuation peak as a function of the core thickness for the 9-QW ECS outcoupler.

Figure 57 shows the normalized reciprocal wavelength (Λ/λ_0) as a function of the normalized propagation constant ($(\beta-K)/K$) and the normalized attenuation coefficient ($\alpha\Lambda$) for an infinitely long grating. The Bragg grating period (Λ_B) is 488.7 nm for of 1550 nm (λ_0). The peak of the normalized attenuation is 0.036 at $\Lambda/\lambda_0 = 0.314$. The grating length is 6.76 μm for light intensity decreases of e^{-1} for a wavelength of 1550 nm.

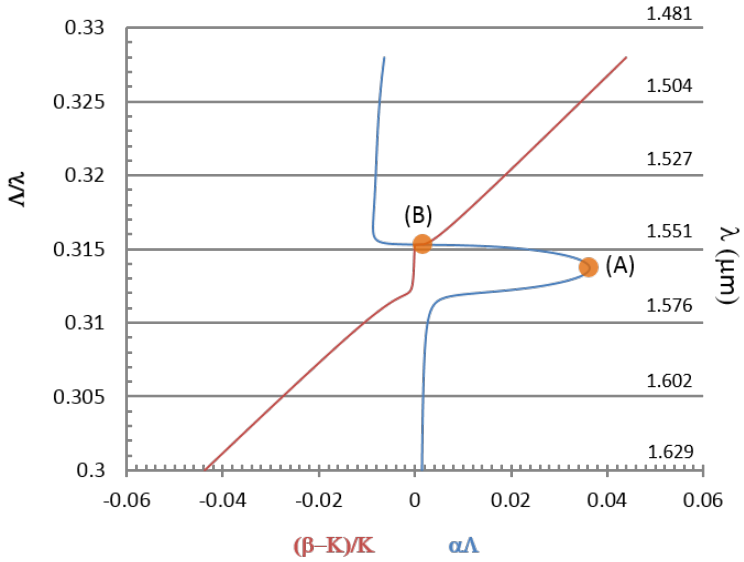

Figure 57. Normalized attenuation and propagation constant for the 9-QW ECS grating with the 150 nm core.

Figure 58(a) and (b) show the intensity distribution in the infinite 9-QW grating with a 150 nm core, 27-nm liner and 200-nm cover layer as a function of distance for normalized wavelengths (Λ/λ_0) corresponding to points (A) and (B) indicated in Figure 57. Figure 58(a) shows the intensity distribution at point (A) in Figure 57 corresponding to the maximum normalized attenuation. Figure 58(b) shows the intensity distribution near the 2nd Bragg condition ($\alpha\Lambda \sim 0$) at point (B) in Figure 57. As in previous intensity plots, the high intensity spots are located within the teeth and grooves on the long wavelength side of the second Bragg and centered at the boundaries of the teeth and grooves at the second Bragg condition.

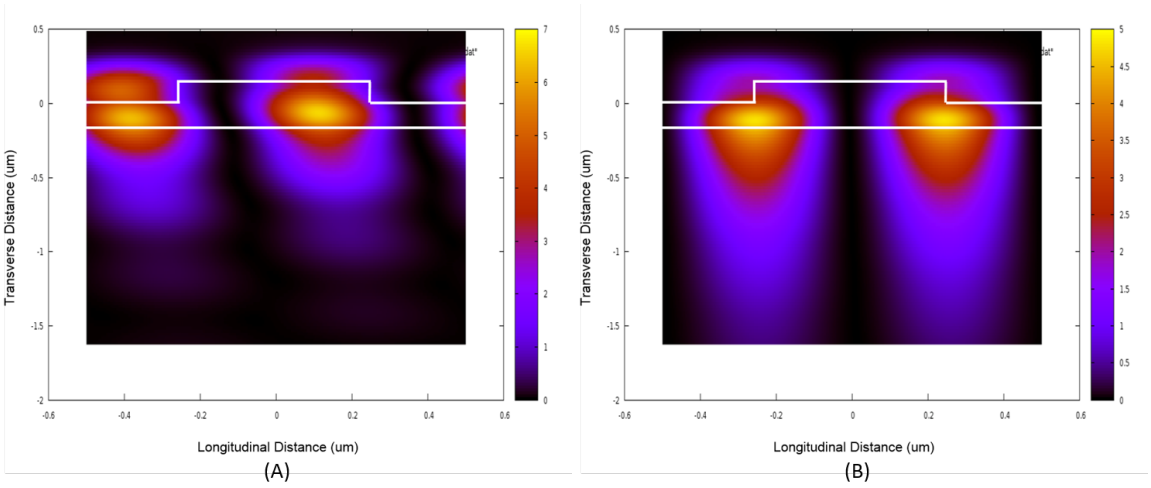

Figure 58. 2D field distribution at different wavelength for the 9-QW ECS grating with the 150-nm cover layer.

3.2.4. Optimization of the Grating Depth for a 9-QW Structure

The etched depth of the grating (W_{etch} in Figure 48) is now varied to optimize the radiated power with an optimized cover layer of 200 nm, liner layer of 27 nm and core layer of 150 nm.

Figure 59 shows the fraction of the incident power radiated down (P_{do}), the incident power radiated up (P_{up}), the incident power reflected (R) and the incident power transmitted (T) as a function of the grating period. The grating length is 20 μm with a 50% duty cycle. For a grating outcoupler, the incident light radiated upwards or downwards refers to percent of incident light outcoupled by the grating. Figure 59(a) shows the power spectrum for the optimized 9-QW waveguide having a grating depth of 100 nm. Most of the incident light (>80%) is transmitted and the maximum radiated power (P_{do}+P_{up}) is only 20% at the grating period of 481 nm. In Figure 59(b), for a grating depth of 150 nm, the maximum radiated power (P_{do}+P_{up}) is increased to 54% with a transmitted power of 32% at a grating period of 479 nm. Figure 59(c) shows the power spectrum for a deeper etched grating depth of 200 nm. At a grating period of 481 nm, the maximum radiated power (P_{do}+P_{up}) is ~ 70%, with both the transmitted and reflected power of ~ 15%, each. In the future we will investigate the maximum practical grating depths for ECS laser structure, both theoretically and from fabrication considerations.

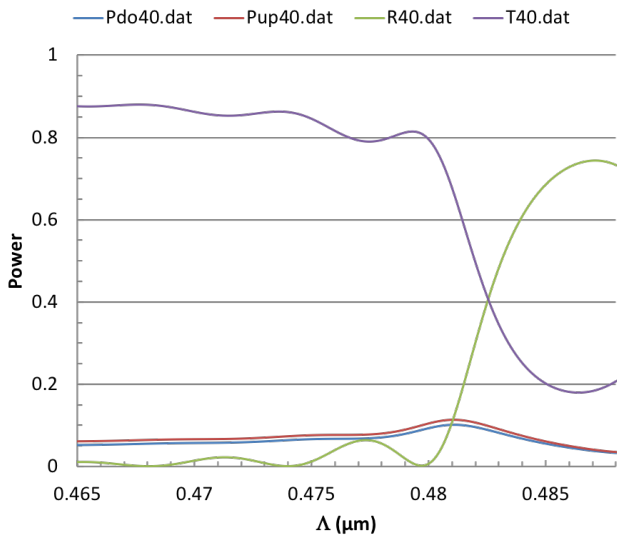
Pdo40.dat
Pup40.dat
R40.dat
T40.dat
1
0.8
0.6
0.4
0.2
0
Power
0.465
0.47
0.475
0.48
0.485
Λ (μm)

(a)

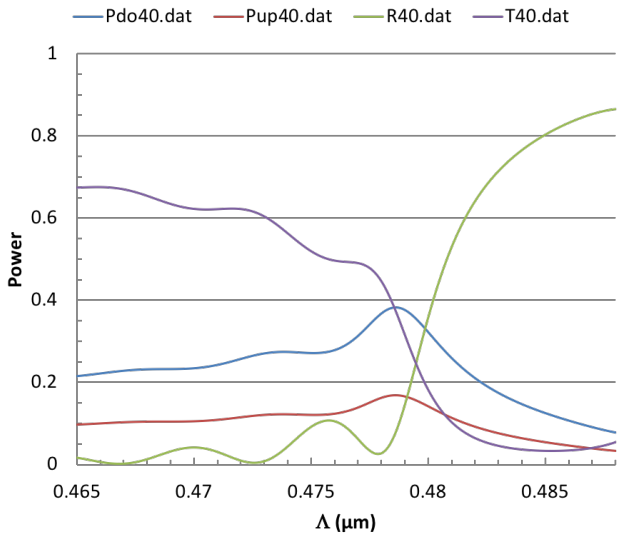
Pdo40.dat
Pup40.dat
R40.dat
T40.dat
1
0.8
0.6
0.4
0.2
0
Power
0.465
0.47
0.475
0.48
0.485
Λ (μm)

(b)

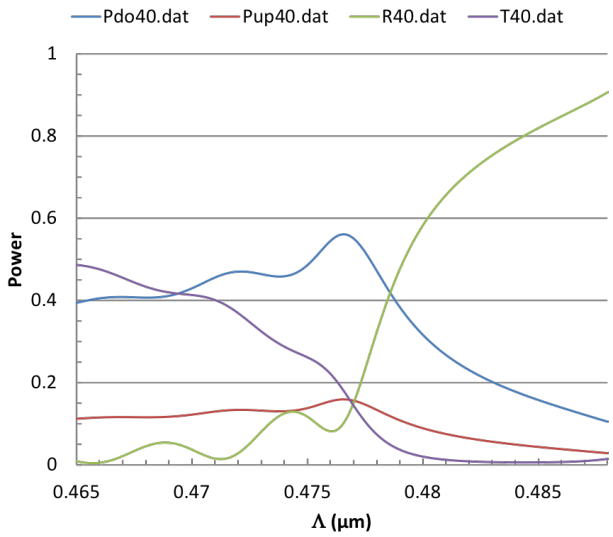

(c)

Figure 59. Power spectrums for the 9-QW ECS with an etched grating depth of (a) 100nm, (b) 150 nm and (c) 200 nm.

3.2.5. Summary

We have determined practical thicknesses of core, liner, cover layer and grating depths for a 9-QW ECS grating waveguide by optimizing the attenuation coefficient. The resulting 9-QW ECS waveguide can couple more than 70% of the light out of a 20 μm long grating.

After this initial work on an ECS grating in a 9 QW structure, a decision was made to decrease the number of quantum wells to simplify the epitaxial growth process and to reduce losses in the grating region. In the following chapter, we optimize the power radiated from a ECS grating outcoupler for the 5-QW laser structure.

Chapter 4

MODELING ECS GRATING OUTCOUPLERS IN 5-QW LASERS NEAR 1550 NM

In this chapter, we discuss the integration of an ECS grating coupler with a 5-QW ridge guide laser and rear DBR mirrors by using the simple planar layer approach and the numerical Floquet-Bloch analysis. The wavelength of light from the ridge guide laser is ~ 1550 nm. The position and length of the ECS outcoupler and DBR are determined for 5-QW laser structure in this section. A standard grating outcoupler (without a low-index liner and high-index cover layer) for the same 5-QW structure is compared to the optimized ECS grating outcoupler. The performance of different configurations of the SiO_2 liner and amorphous silicon cover layer is analyzed in part to account for possible fabrication restrictions and production tolerances.

Table 8. Epitaxial layers of the 5-QW laser structure. (* The SCH values are those chosen after the analysis in sections below.)

Layer	Composition	Thickness (μm)	Material Index
Air		--	1
Cap	InGaAs	0.100	3.62525
P-clad	InP	2	3.16492
SCH	$In_{0.74}Ga_{0.26}As_{0.5}P_{0.5}$	0.244*	3.35110
4x barriers	$In_{0.74}Ga_{0.26}As_{0.5}P_{0.5}$	0.008	3.35110
5x QWs	$In_{0.74}Ga_{0.26}As_{0.81}P_{0.19}$	0.006	3.50636
SCH	$In_{0.74}Ga_{0.26}As_{0.5}P_{0.5}$	0.044*	3.35110
N substrate	InP	--	3.16492

4.1. 5QW ECS Structure Optimization

4.1.1. Optimizing the Core Thickness

Figure 60 shows the ECS grating for the 5-QW laser structure. The core layer includes 5 QWs and 4 barriers with SCH layers on both sides. The grating is assumed to be etched 200 nm (W_{etch}) deep in InGaAsP, followed by the deposition of a thin SiO_2 liner (d = 27 nm) and an amorphous Si cover layer (W_{cov} = 200 nm). The total grating depth (W_g) is 227 nm including the etched grating depth (W_{etch}) and the liner thickness (d). The thickness of a high-index cover layer is varied to optimize the power of radiations.

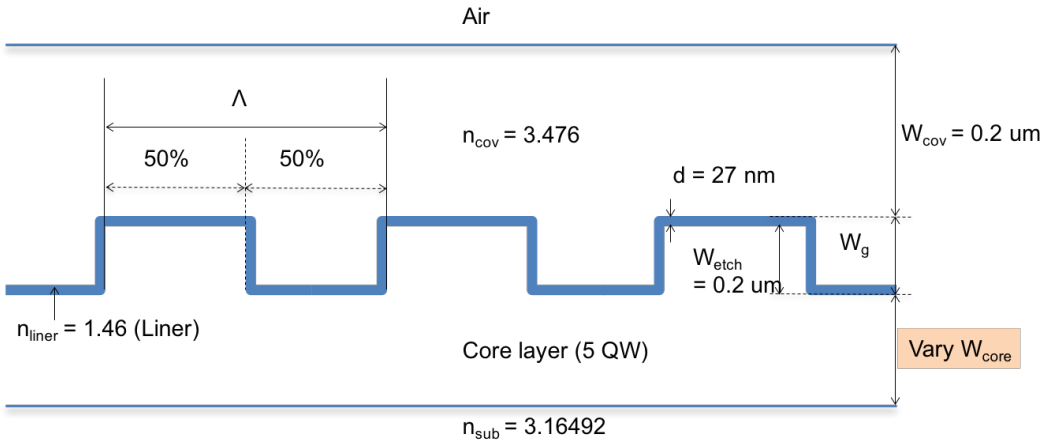

Figure 60. Sketch of the 5-QW ECS grating for varying the thickness of the core layer.

Figure 61 shows the power radiated down (P_{do}), power radiated up (P_{up}), power reflected (R), power transmitted (T), total power radiated (P_{up}+P_{do}) and sum of all of the powers as a function of the wavelength. The grating length is 19.564 μm and the 2nd Bragg grating period is 489.1 nm with a 50% duty cycle at a wavelength of 1550 nm. The incident power is assumed to be 1, so the variation of the sum of the total reflected, transmitted and outcoupled power indicates that the maximum error of this Floquet-Bloch approach is less than 5% from the exact Bragg condition. The percentage of light radiated upwards and

downwards (P_{up}+P_{do}) is our measure of the grating coupling efficiency. For the structure shown in Figure 60, the maximum total radiated power is 74.1% and the reflected power (R) is only about 10% at the wavelength of 1587.9 nm.

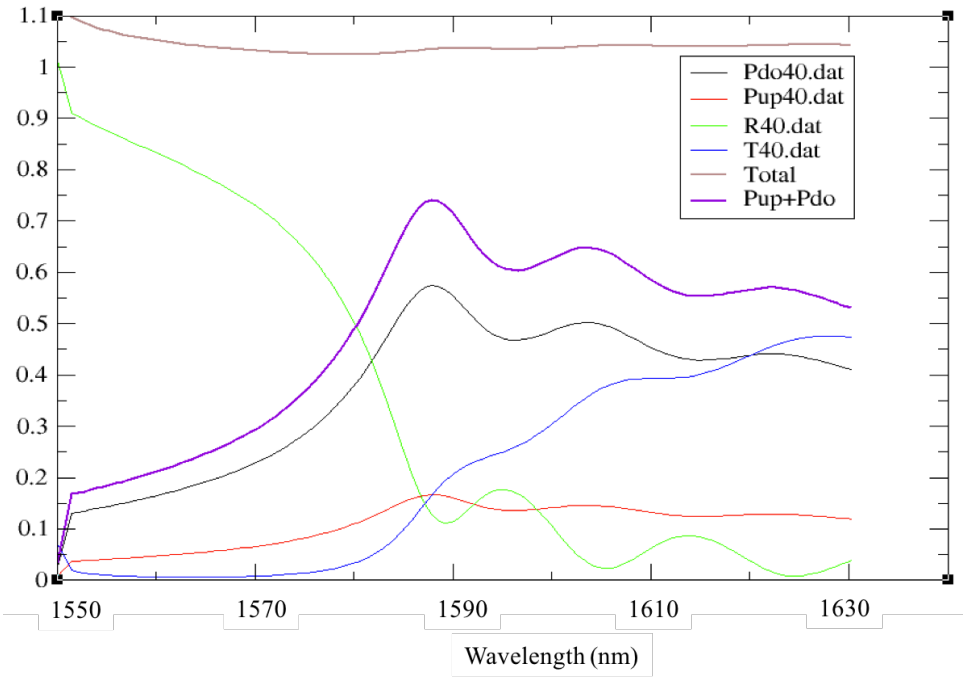

Figure 61. Power spectrum for the 5-QW ECS grating having a core layer of 150 nm, liner layer of 27 nm and a cover layer of 200 nm."

The plot in Figure 62 shows the total radiated power as a function of the core layer thickness. The slight variation of the total radiated power is only about 3.6% as the core layer thickness is changed from 100 nm to 200 nm thick. Table 9 summarizes the upward radiated power, downward radiated power and total radiated power of light for different thicknesses of the core layer. As the core layer thickness increases, the downward radiated power is reduced which contributes to the total radiated power reduction.

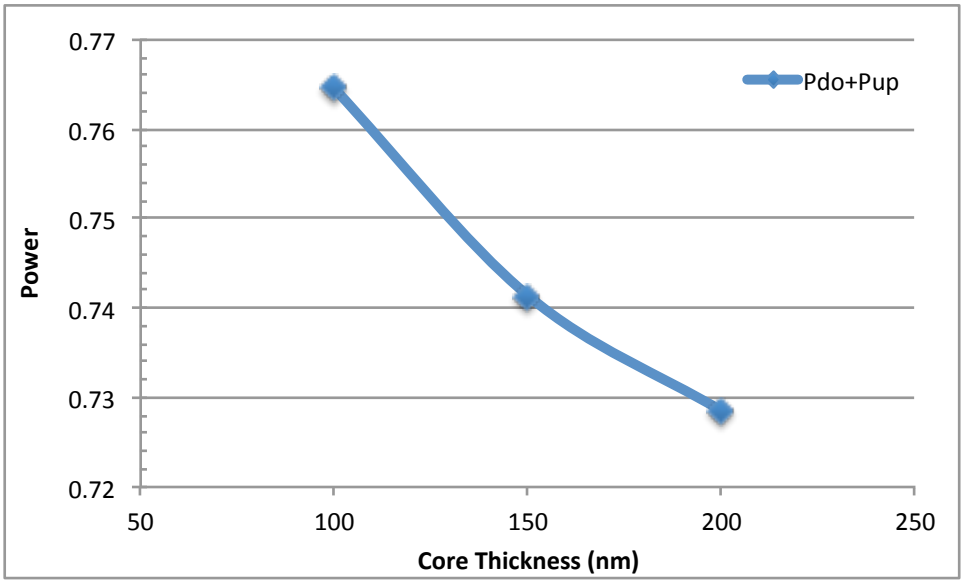

Figure 62. Radiated power as a function of the core thickness, a liner layer of 27 nm and a cover layer of 200 nm.

Table 9. Radiated power of different core thicknesses for the 5-QW ECS grating.

Core (nm)	Power Down	Power Up	Up and Down
100	0.593348	0.171232	0.76458
150	0.57459	0.1668	0.74139
200	0.553022	0.175478	0.7285

The total QW confinement factor is calculated in the ridge and grating region in Figure 63. The total QW confinement factor in the laser gain region changes little (about 5%) as the core layer thickness varies but the total QW confinement factor in the grating region decreases as the core thickness decreases. A lower QW confinement factor in the unpumped grating region is desirable to reduce absorption losses. Therefore, 150 nm is chosen for the core layer thickness.

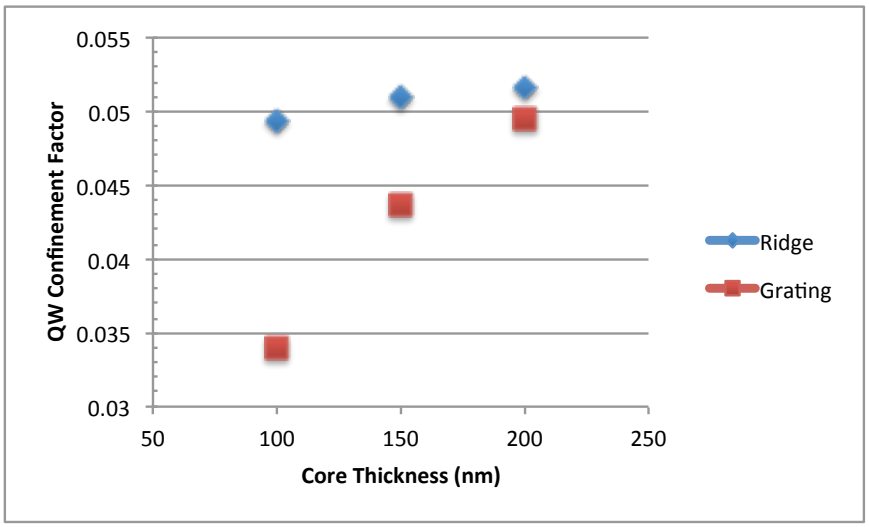

Figure 63. Total QW confinement factor in the ridge and grating section as a function of the core thickness. Liner layer of 27 nm and a cover layer of 200 nm.

4.1.2. Optimizing the Amorphous Si Cover Layer Thickness

The thickness of an amorphous silicon cover layer (W_{cov} in Figure 60) is varied to optimize the radiated power for a core layer of 150 nm. The plot in Figure 64 shows the radiated power as a function of the cover layer thickness. The calculation assumes the grating length to be 19.548 μm with a 50% duty cycle. At a cover thickness is 230 nm, the maximum radiated power is 75.86%.

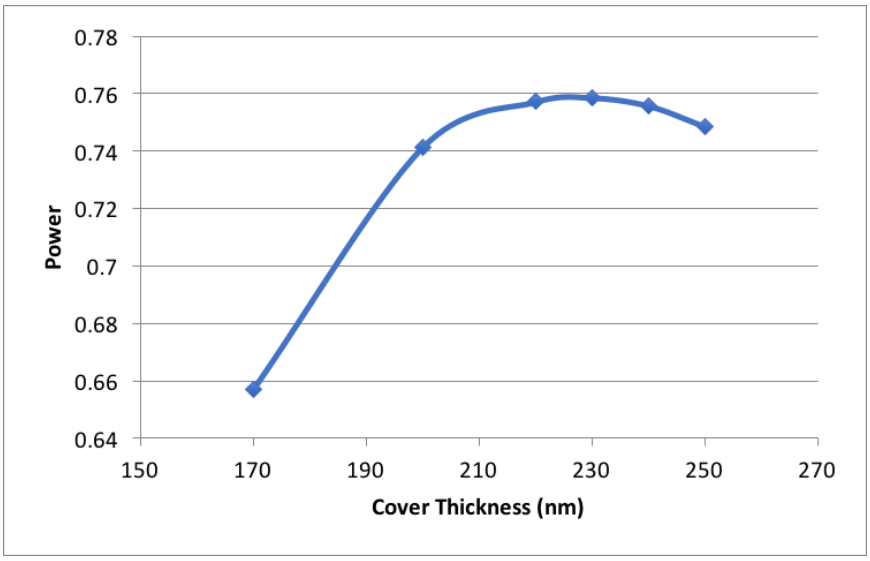

Figure 64. Radiated power as a function of the cover thickness for the 5-QW ECS grating with a core layer of 150 nm and liner layer of 27 nm.

Figure 65 shows the power radiated down (P_{do}), power radiated up (P_{up}), total power radiated ($P_{up}+P_{do}$), power reflected (R), power transmitted (T) and sum of power as a function of the wavelength. The 2nd Bragg grating period is 488.7 nm at the wavelength of 1550 nm. The excess of the total power from 100% shows that the maximum error of the Floquet-Bloch approach is below 5%. The maximum radiated power ($P_{up}+P_{do}$) is 75.9% and the reflected power (R) is about 10% at the wavelength of 1591.3 nm. The reflected power can be minimized with small reductions of the radiated power by operating at a wavelength further away from the 2nd Bragg condition.

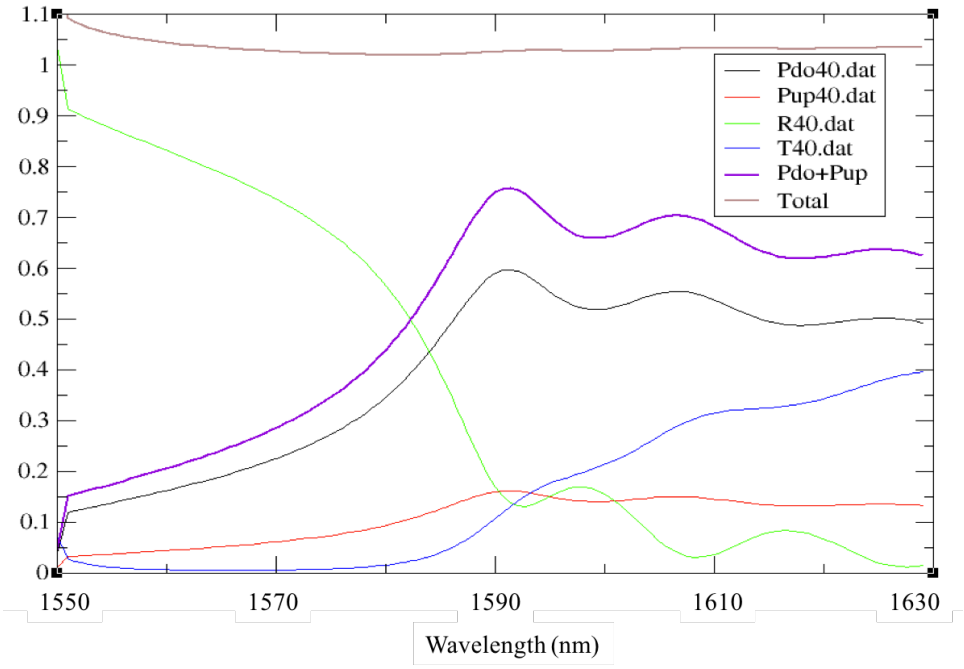

Figure 65. Power spectrum for the 5-QW ECS grating having a core layer of 150 nm, liner layer of 27 nm and a cover layer of 230 nm.

4.1.3. Optimizing the Liner Thickness

The thickness of a SiO_2 liner layer (*d* in Figure 60) is varied to optimize the radiated power with a core layer of 150 nm and a cover layer of 230 nm. The plots in Figure 66 show the radiated power ($P_{do}+P_{up}$) and the sum of the power ($P_{do}+P_{up}+R+T$) as a function of the liner thickness. As the radiated power increases with liner thickness, the error associated with the total power calculated also increases, from ~2% to an unacceptable 35%. A thickness of 25 nm for the liner layer was chosen to keep the numerical errors below 5%. Future work will investigate the source(s) of error for this calculation. For these choices of core layer (150 nm), liner layer (25 nm) and cover layer (230 nm), the upward and downward radiated power is 73.6% for a grating length of 19.5 μm for the 5-QW ECS outcoupler waveguide in Figure 67.

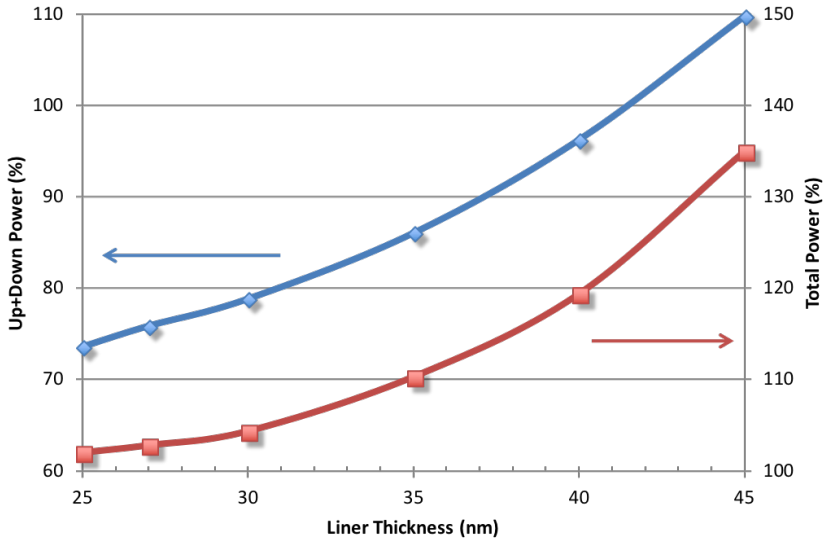

Figure 66. Radiated and total power as a function of the liner thickness with a core layer of 150 nm and a cover layer of 230 nm.

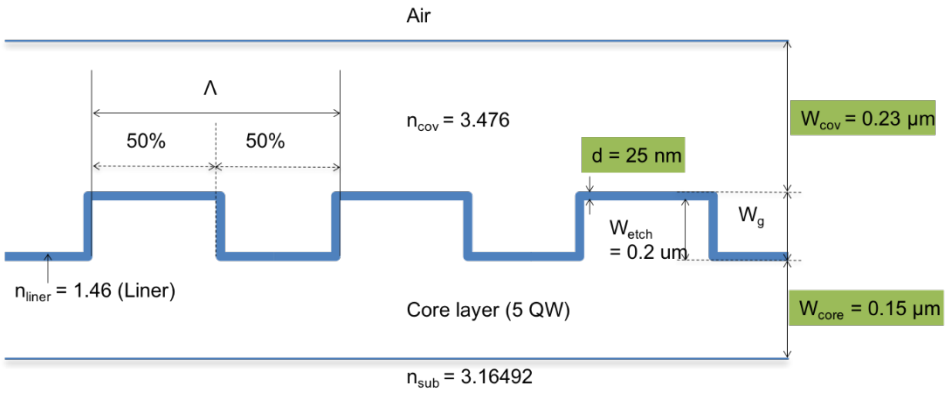

Figure 67. Sketch for optimized 5-QW ECS grating structure.

The layer compositions, thicknesses and indices of the optimized 5-QW ECS grating structure are shown in Table 3.

Table 10. Layers in the grating section of the 5-QW laser structure.

Layer	Composition	Thickness (μm)	Material Index
Air		--	1
A-Si	Amorphous Silicon	0.230	3.476
Grating 3	60% SiO_2+40% Si	0.025	2.47224
Grating 2	50% InGaAsP+10% SiO_2+40% Si	0.175	3.26514
Grating 1	50% InGaAsP+50% SiO_2	0.025	2.58471
SCH	$In_{0.74}Ga_{0.26}As_{0.5}P_{0.5}$	0.044	3.35110
4x barriers	$In_{0.74}Ga_{0.26}As_{0.5}P_{0.5}$	0.008	3.35110
5x QWs	$In_{0.74}Ga_{0.26}As_{0.81}P_{0.19}$	0.006	3.50636
SCH	$In_{0.74}Ga_{0.26}As_{0.5}P_{0.5}$	0.044	3.35110
N substrate	InP	--	3.16492

The plots in Figure 68 are the normalized reciprocal wavelength (Λ/λ_0) as a function of the normalized propagation constant ((β-K)/K) and the normalized attenuation ($\alpha\Lambda$). These are calculated for an infinite grating in the 5-QW ECS waveguide by the Floquet-Bloch approach for the core layer (150 nm), liner layer (25 nm) and cover layer (230 nm) determined in the previous sections. Calculations assume the wavelength in free space to be 1550 nm (λ_0) with different values for the grating period (Λ). The peak of the normalized attenuation is 0.08 at $\Lambda/\lambda_0 = 0.312$. The grating length corresponding to the intensity of transmitted light reduced to e^{-1} is

$$L = N\Lambda = \frac{1}{2\alpha} \tag{48}$$

which is 3.05 μm.

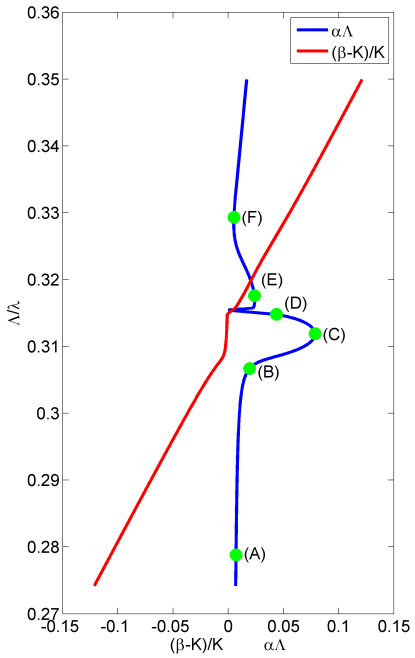

Figure 68. Normalized attenuation and propagation constant of the 5-QW ECS grating with a core layer of 150 nm, liner layer of 25 nm and a cover layer of 230 nm.

The plots in Figure 69 show the fraction of the incident power radiated down (P_{do}), the incident power radiated up (P_{up}), the incident power reflected (R), the incident power transmitted (T), the incident power radiated both upwards and downwards ($P_{do}+P_{up}$) and the sum of the incident power reflected, transmitted and radiated as a function of the grating period for the 5-QW structure with a core layer of 150 nm, a liner layer of 25 nm and a cover layer of 230 nm. The sum of the power exceeding 100% shows that the maximum error of the Floquet-Bloch analysis is around 5%. The 2nd Bragg grating period is 488.2 nm at the wavelength of 1550 nm.

The points (A), (B), (C), (D), (E) and (F) in Figure 69 match the corresponding points indicated in Figure 68. The grating length is 19.5, 48.82 and 100 μm long in the power spectrum shown in Figure 69(a), (b) and (c), respectively. The maximum

normalized attenuation occurs at point (C) in Figure 68; however, for all grating lengths, the total radiated power is only around 20% and the reflected power is around 80% at point (C) in Figure 69. The attenuation is related to not only radiation but transmission and reflection. Thus, the grating period (or wavelength) of the maximum attenuation is not the desired grating period (or wavelength) for maximum radiation.

In Figure 69(a), the maximum radiated power occurs at point (B) on the long wavelength side and at point (E) on the short wavelength side of the 2nd Bragg condition for a grating length of 19.5 μm. At point (B), the maximum radiated power (75%) consists of the upward radiation (15%) and the downward radiation (60%). On the other hand, at point (E), the maximum radiated power (80%) is mostly downward with only a small portion of the upward radiation (< 5%). The reflected power is about 10% at the maximum radiated power. Especially on the long wavelength side of the 2nd Bragg condition, the reflected power can be reduced with a slight decrease of the radiated power by operating at a wavelength further away from the 2nd Bragg condition. In Figure 69(b), the maximum radiated power (close to 90%) occurs at a slightly different wavelength for a grating length of 48.82 μm. As the grating length is increased to 100 μm, the maximum radiated power occurs beyond 1600 nm with a small amount of the power reflected and transmitted (less than 5%) as shown in Figure 69(c).

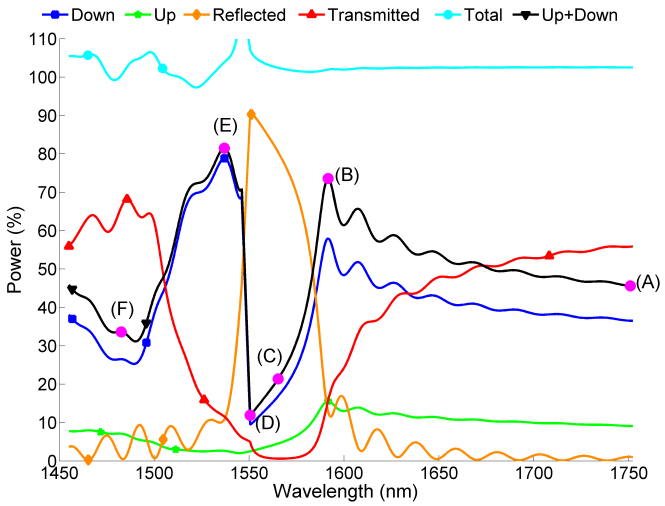
Down
Up
Reflected
Transmitted
Total
Up+Down
Power (%)
Wavelength (nm)
(A)
(B)
(C)
(D)
(E)
(F)

(a)

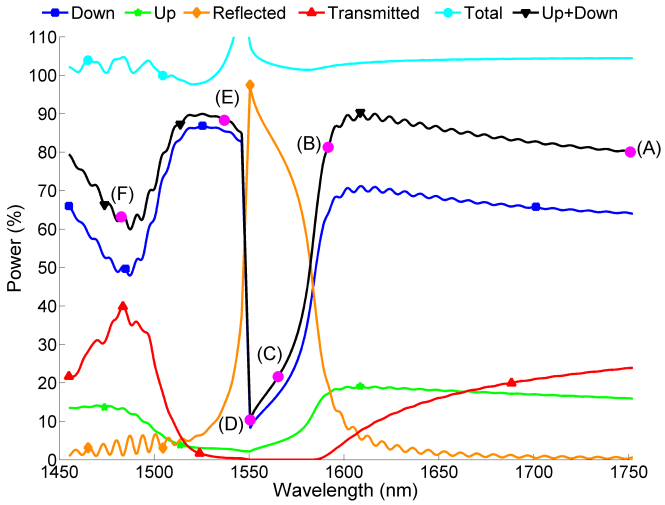
Down
Up
Reflected
Transmitted
Total
Up+Down
Power (%)
Wavelength (nm)
(A)
(B)
(C)
(D)
(E)
(F)

(b)

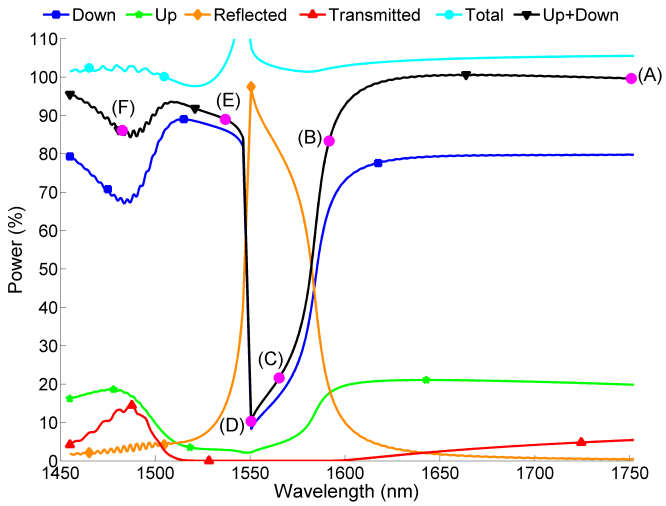

(c)

Figure 69. Plot of the power reflected, transmitted, radiated, and total power for the 5-QW ECS waveguide with a grating length of (a) 19.5 um, (b) 48.82 um and (c) 100 um with a core layer of 150 nm, a liner layer of 25 nm and a cover layer of 230 nm.

Figure 70 shows the intensity distributions in the infinite 5-QW ECS grating at different wavelengths corresponding to points (A) through (F) indicated in Figure 68 and Figure 69. The top horizontal white dashed line indicates the top of the cover layer, the middle white dashed lines indicate a cycle of the grating period and the bottom horizontal line indicates the bottom of the n-side SCH layer of the core layer. Figure 70(a) shows the intensity distribution at the wavelength of 1750 nm which is far away on the long wavelength side from the 2nd Bragg condition. Figure 70(b) shows the intensity distribution at point (B) in Figure 68 where the normalized attenuation begins to increase and shows that the high intensity peaks are located near the center of the ridge and grooves. Figure 70(c) shows the intensity distribution at point (C) in Figure 68 corresponding to the peak of the normalized attenuation at the wavelength of 1565 nm. Figure 70(d) shows the intensity distribution near the 2nd Bragg condition ($\alpha\Lambda \sim 0$) at point (D) in Figure 68 and

shows that the high intensity peaks are located near the boundary between the grating tooth and grating groove. Figure 70(e) shows the intensity distribution at the wavelength of 1537 nm which is point (E) in Figure 68. Figure 70(f) shows the intensity distribution at the wavelength of 1483 nm which is point (F) in Figure 9, where the grating period is far away on the short wavelength side from the 2nd Bragg condition.

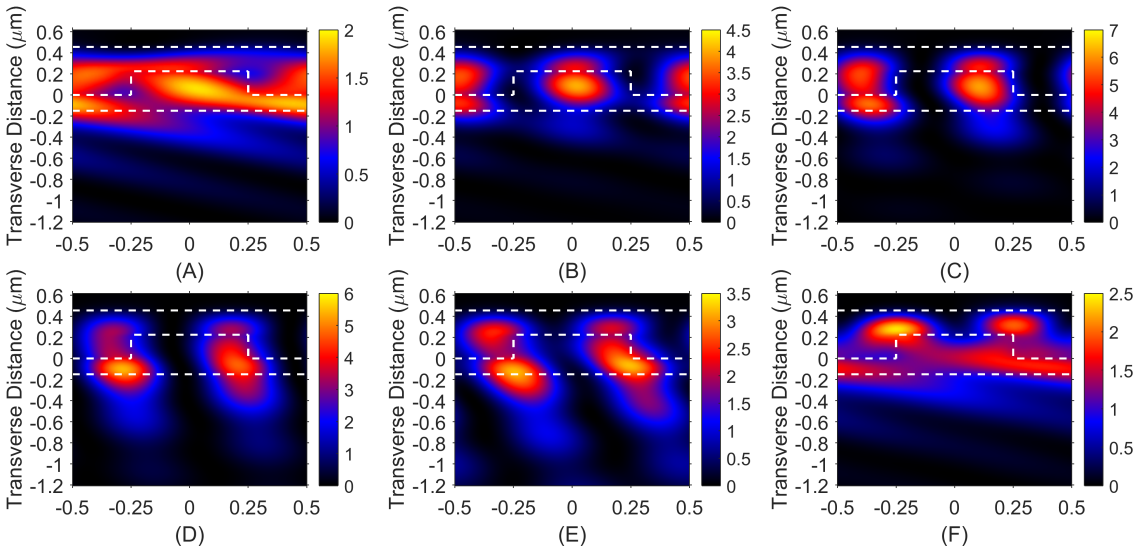

Figure 70. Field distribution in the grating region (a) at 1750 nm, (b) at 1592 nm, (c) at the peak of the normalized attenuation, (d) about 1550 nm, (e) at 1537 nm and (f) at 1483 nm with a core layer of 150 nm, a liner layer of 25 nm and a cover layer of 230 nm.

Commercial Finite-Difference Time-Domain (FDTD) software was used to verify the results of the SMU Floquet Bloch grating software for the structure analyzed in Figures 9, 10 and 11 by colleagues at Oracle [36]. To reduce the FDTD computation time to reasonable values, the 5 QW core layer was approximated by an average index of refraction. Figure 71 shows the calculated fraction of downward radiation, upward radiation, reflected radiation and the transmitted radiation by FDTD. The grating period is 477 nm and the grating length is 19.08 μm. The 2nd Bragg wavelength is 1520 nm for an effective mode

index of 3.19. This FDTD calculation agrees qualitatively with the radiation values calculated by the SMU Floquet Bloch software. In particular, the power radiated down is many times larger than the power radiated up by both methods. The quantitative values from the FDTD software are likely off mainly because the larger grid choices required to obtain numerical results in reasonable times.

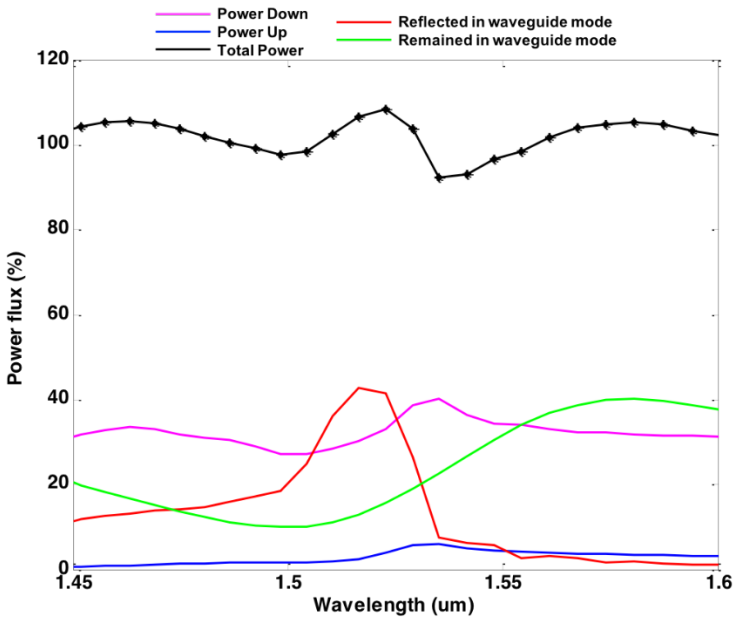

Figure 71. FDTD simulation of the power radiated down, radiated up, reflected and remained in waveguide mode with grating period of 477nm in a length of 19.08 μm. (Figure courtesy of Jin Yao, Oracle)

Figure 72 shows the pulse propagation from the unperturbed transition waveguide to the ECS grating waveguide calculated by using FDTD for the structure associated with Figures 9, 10, 11 and 12. The red arrow shown in Figure 72 indicates the direction of the light propagation.

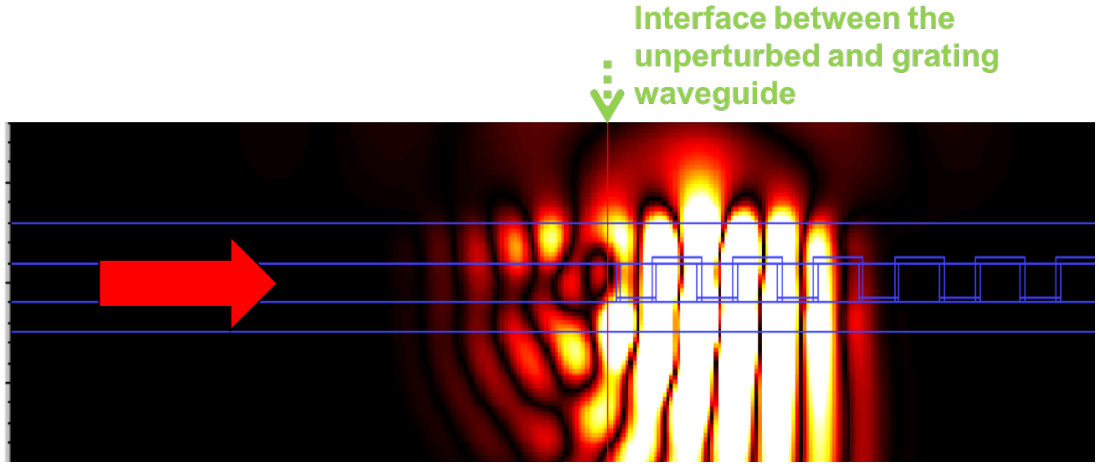

Figure 72. Pulse propagation from the unperturbed waveguide to the grating waveguide. (Figure courtesy of Jin Yao, Oracle)

The normalized transverse field intensities calculated by FDTD are captured at the interface between the unperturbed and the grating waveguide (green arrow in Figure 72) with wavelengths varying from 1510 to 1590 nm in Figure 73. The interface is defined at one period into the unperturbed transition waveguide. In Figure 73, x = 0 is the center of the grating and x = - 0.1 μm is the bottom of the 0.2 μm deep grating. The peak of the mode field occurs in the core layer.

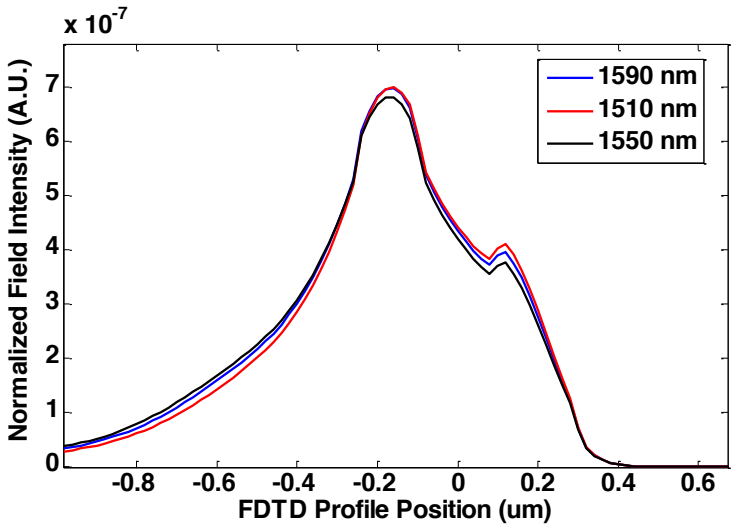

Figure 73. Field intensity at the interface shown in Figure 72 for different wavelengths. (Figure courtesy of Jin Yao, Oracle)

4.1.4. Field Overlaps in the Laser, Transition and Grating Sections

The ECS outcoupler region is integrated with 5-QW laser and radiation losses at the transitions between sections are a concern. In addition to the single transverse mode defined by the epitaxial structure in the x direction, the mode in the laser and transition regions must be confined in the lateral direction. Because of gain-induced index depression in the quantum wells, a lateral effective index difference (Δn) in a range of 0.01 to 0.02 is required in the InGaAsP/InP laser region. (Smaller values of Δn are sufficient to provide lateral guiding in the passive transition and grating regions.)

Figure 74 shows the effective index as the thickness of the p-clad InP layer decreases for the laser structure shown in Table 8. A lateral effective index difference Δn of 0.015 between the ridge and the groove corresponds to a remaining InP p-clad of 0.2 μm. A thin (~150 Å) InGaAsP etch-stop layer is inserted in the InP p-clad layer for ease of ridge fabrication.

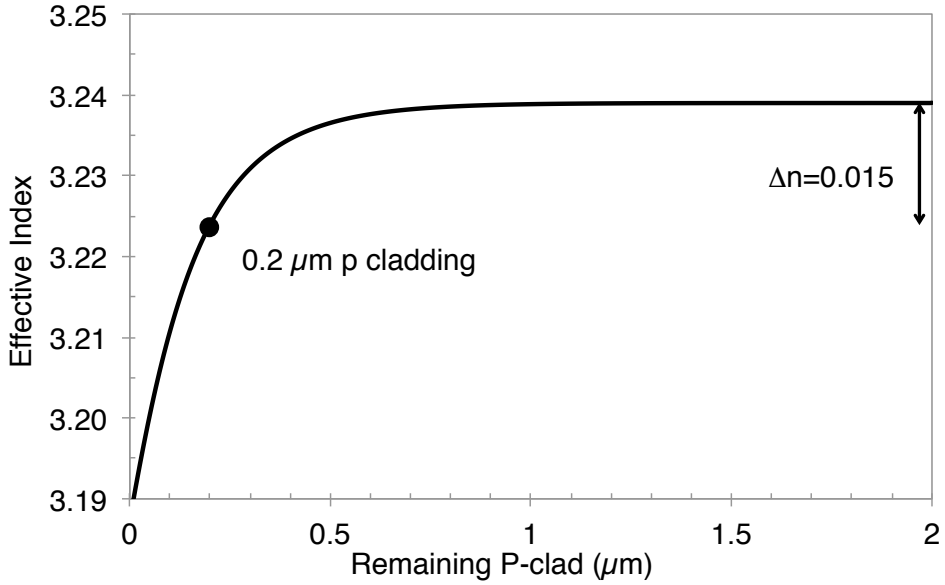

Figure 74. Effective index of the laser section as a function of the remaining p-clad layer.

Figure 75 shows a cross section of the laser section, two transition regions, and the ECS outcoupler grating section. Transition section 2 corresponds to the etch depth that defines the laser ridge to provide a lateral index difference of 0.15. Transition section 3 corresponds to the top of the grating outcoupler. Grating section 4 is the ECS grating outcoupler with a low-index liner and high-index cover layer. The 25-nm SiO_2 liner and the 230-nm amorphous silicon cover layer were determined in the above sections to maximize the radiated power. The short transition regions (< 10 μm) between the laser and grating region decreases losses (and are necessary for some fabrication steps) which results from reflections and radiations at discontinuities between sections.

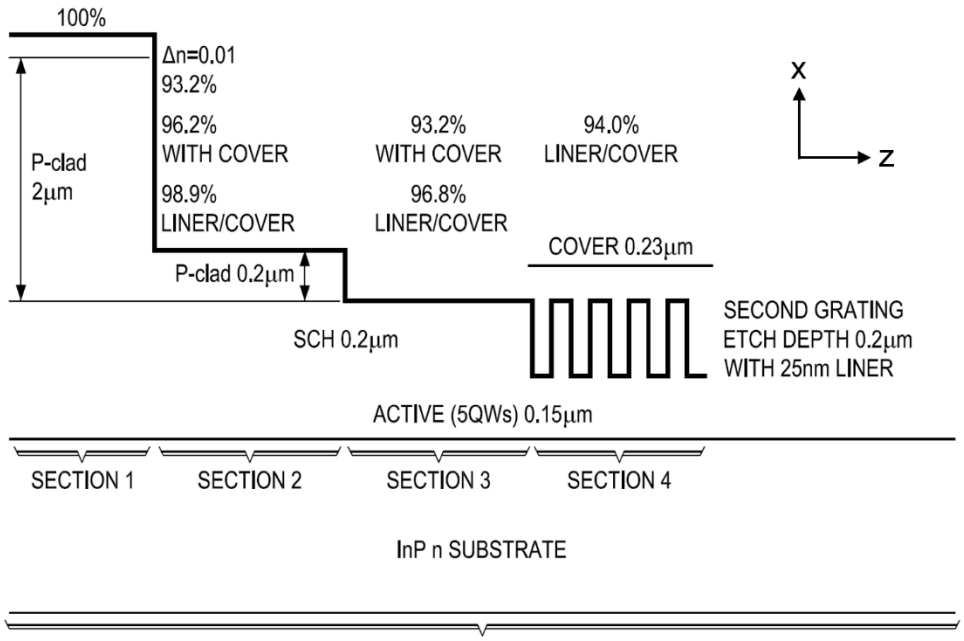

Figure 75. Cross section of laser section 1, transition section 2, transition section 3, and grating section 4 for the 5-QW laser waveguide.

Figure 76 illustrates transverse field intensities and index profiles in the laser gain region, two transition sections and grating region of the ECS laser waveguide of Figure 75. The full width at half power of the field intensity in the laser section 1 is 442 nm. In Figure 76(a), the overlap of the field intensity in laser section 1 to that of the field intensity in transition section 2 is 93% without any liner or cover layer but increases to 99% with the liner and a cover layer present. In Figure 76(b), the overlap of the field intensity in laser section 1 with the field intensity in transition section 3 is 73% without any liner or cover layer but increases to 97% with the liner and a cover layer present. In Figure 76(c), the overlap of the field intensity in laser section 1 with the field intensity in grating section 4 is 94% with a liner and a cover layer present. Without a liner and cover layer, grating section 4 does not a mode, so the overlap in this case would be 0%.

Typically, the overlap integral between the laser gain region and a DBR grating region for commercial semiconductor lasers is in a range of 0.85 to 0.9 [30]. Therefore, the use of a liner and cover layer has applications towards decreasing losses for commercial DBR lasers.

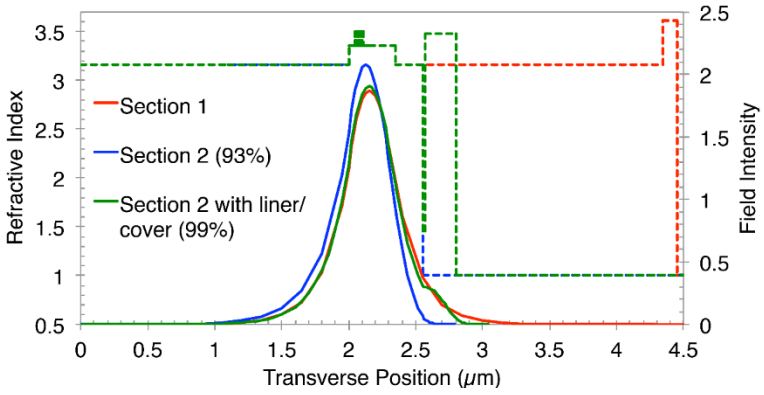

(a)

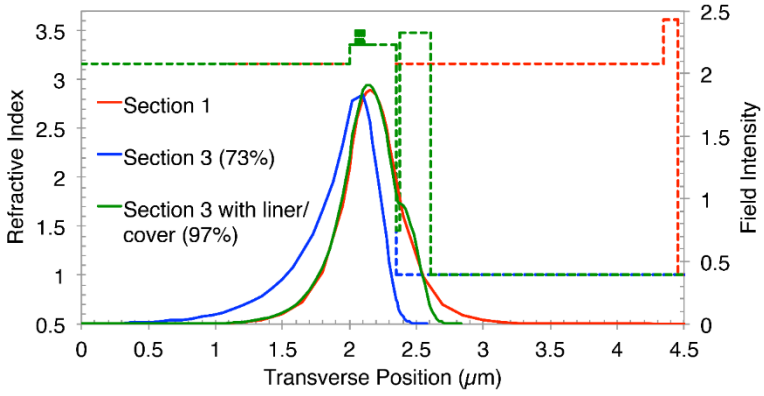

(b)

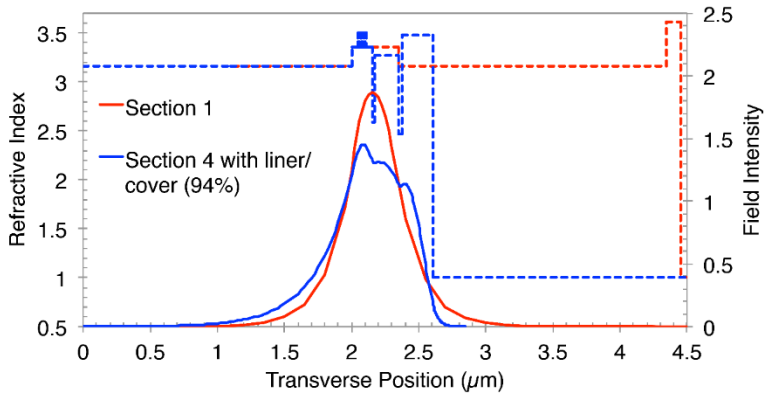

Figure 76. Field and index profiles for (a) laser section 1 and transition section 2, (b) laser section 1 and transition section 3, and (c) laser section 1 and grating section 4.

The 2D field distributions in the x-y plane for a ridge width of 4.5 μm in laser section 1 is shown in Figure 77(a). Figure 77(b) shows the lateral field distribution in x-y plane for a confinement ridge width of 4.5 μm in transition section 3. The surface of transition section 3 has a 25-nm SiO_2 liner and 230-nm amorphous silicon cover layer.

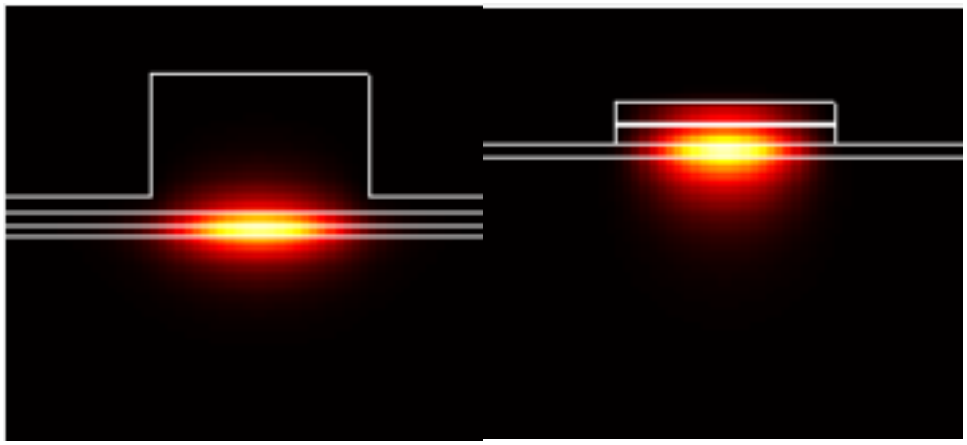

(a) (b)

Figure 77. Lateral field distribution in x-y plane of (a) a 4.5-micron ridge in laser section 1 and (b) a 4.5-micron confinement ridge in transition section 3 deposited by a 25-nm liner and a 230-nm a-Si cover. (Figure courtesy of Jin Yao, Oracle)

Figure 78 shows the theoretical far field with a full width at half power beam divergence of 45.1° for edge-emission of the 5-QW laser waveguide.

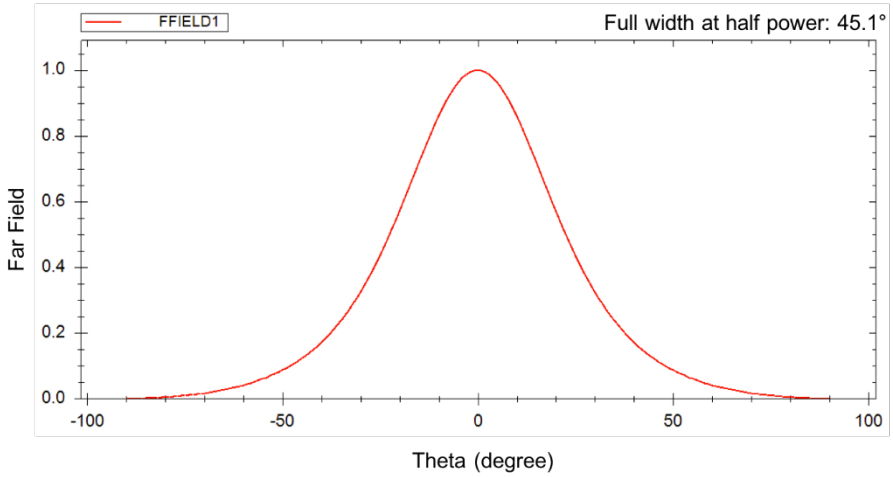

Figure 78. Far field for the optimized 5-QW laser waveguide.

4.1.5. Rear ECS DBR Mirrors

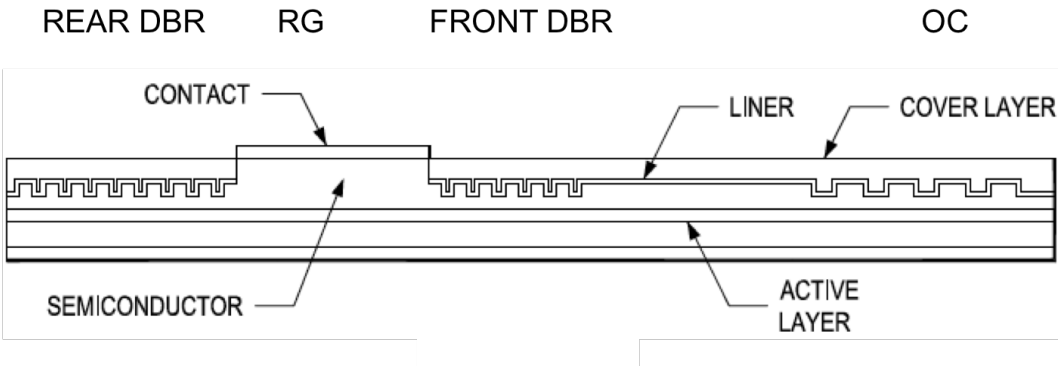

Figure 79. Sketch of DBR laser having the rear and front DBR mirrors and outcoupler deposited by a liner and cover layer.

Figure 79 shows a 5-QW laser with a high-reflect (R > 0.9) rear DBR mirrors and low-reflect (R ~ 0.1) output DBR mirrors followed by an ECS outcoupler. To simplify

fabrication, the thicknesses of the SiO_2 liner and amorphous silicon cover layers for the DBR gratings are assumed to be the same thickness of the liner and cover layer used for the ECS outcoupler grating.

The DBR grating is also assumed to have a 50% duty cycle and a grating depth of 225-nm with a 25-nm liner and 230-nm cover layer. However, because the DBR is a 1st order grating, it cannot be located at the same level as the 2nd order outcoupler because the field intensity overlap is 67.5% as shown in Figure 80. If the top of the 0.2 µm deep DBR grating is positioned at 0.2 µm above the p-SCH layer, the field intensity overlap is increased to 96.2% between the laser section and the InP DBR region as shown in Figure 81.

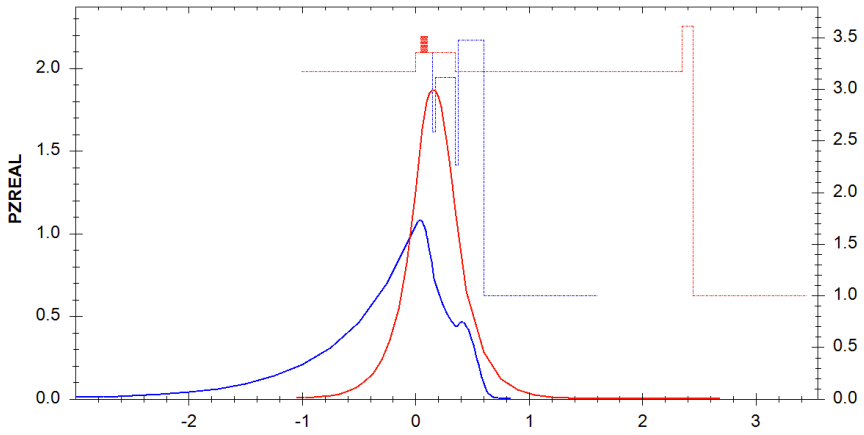

Figure 80. Field intensity and index profile for the laser section and the InGaAsP DBR with the DBR grating located at the same position as the ECS grating.

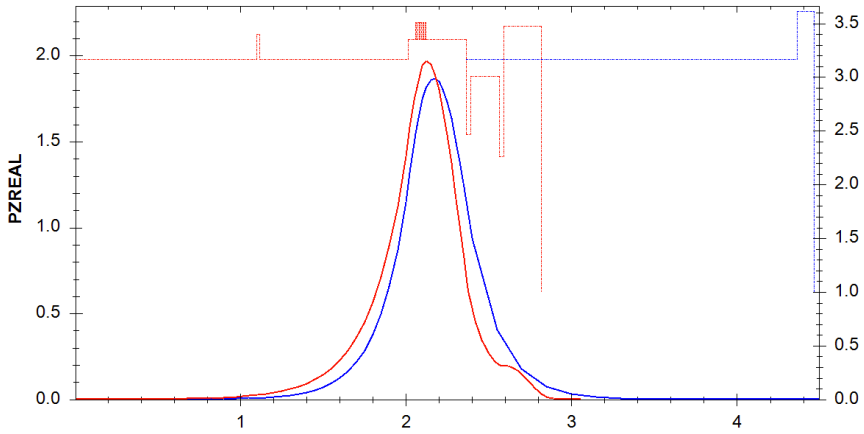

Figure 81. Field intensity and index profile for the laser section and the InP DBR positioned 0.2 μm above the p-SCH layer.

Figure 82 shows the normalized attenuation ($\alpha\Lambda$) and propagation constant ($\beta\Lambda$) as a function of wavelength calculated for the InP ECS DBR grating positioned 0.2 μm above the p-SCH layer. The peak of the normalized attenuation is 0.004 at the operating wavelength of 1550 nm. The plots in Figure 83 shows a maximum reflected power of 77% for a grating length of 80.3 μm for a first-order Bragg period of 241 nm. Longer and shorter DBR grating lengths can provide both high reflect and low reflect DBRs.

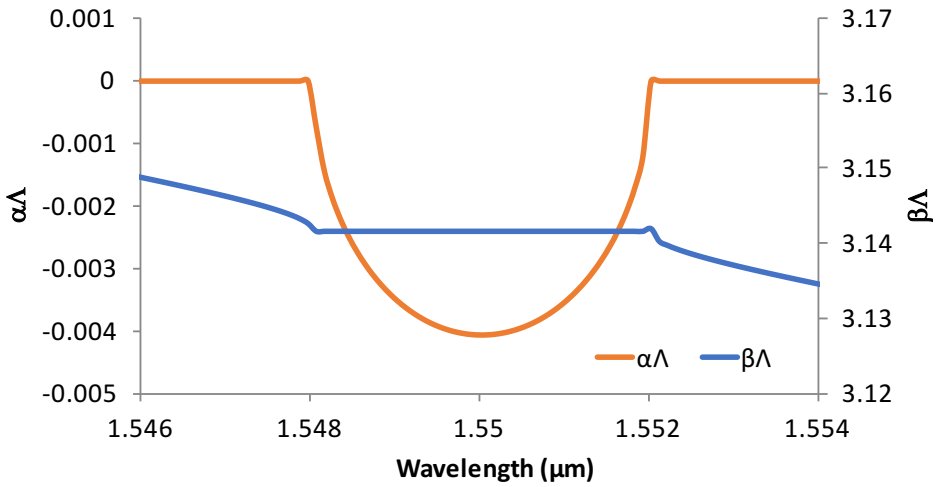

Figure 82. Plot of the real and imaginary part of the propagation constant for the 5-QW ECS DBR grating in InP.

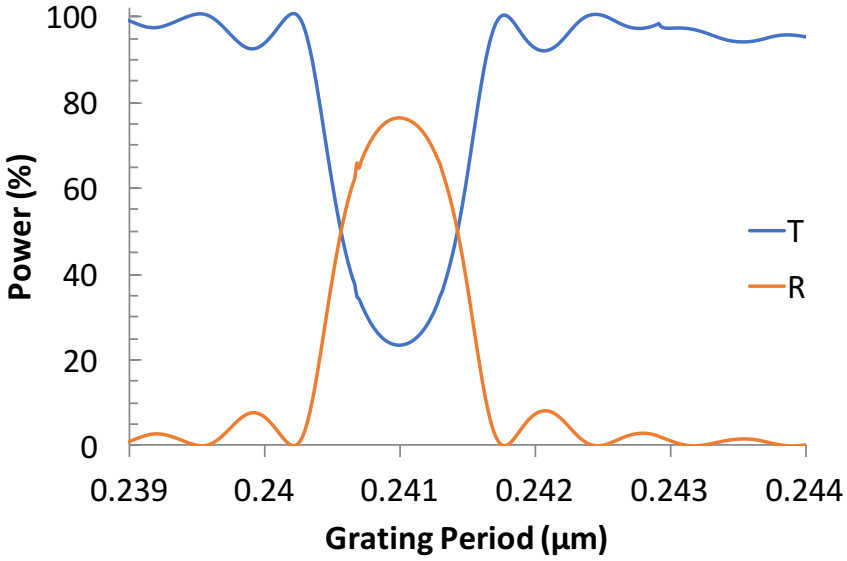

Figure 83. Power reflected and transmitted as a function of the grating period for the 5-QW ECS DBR grating in InP.

4.1.6. Summary

The thickness of a core, liner and cover layer for the 5-QW waveguide grating are chosen by considering the power radiation from the ECS outcoupler. Depending on the length of the grating outcoupler, the operating wavelength should be 50 to 100 nm away from the 2^{nd} Bragg to maximize the total radiated power and minimize the reflected power. The maximum attenuation does not correspond to the maximum radiated power, since reflected light can contribute significantly to the attenuation. The location of the 1^{st} order ECS DBR grating is located at a higher position than the 2^{nd} order ECS outcouler grating.

4.2. Other Configurations of the Liner and Cover Layers

4.2.1. Half Thickness of the Liner on Sidewalls

Depending on the SiO_2 deposition process used to form a continuous liner layer over the grating structure, the SiO_2 deposited on the grating sidewalls might be thinner than that of SiO_2 deposited at the top and bottom of the grating tooth as illustrated in Figure 84. Calculations assume the SiO_2 thickness on the sidewall to be *s* and the SiO_2 thickness at the top and bottom of the grating tooth to be *d*. Except for the liner thickness, the refractive index and thickness of each layer are the same as the final 5-QW ECS waveguide structure discussed in previous sections. Since the conformal liner thickness was 25 nm, we assume that *d* is 25 nm and *s* is 12 nm.

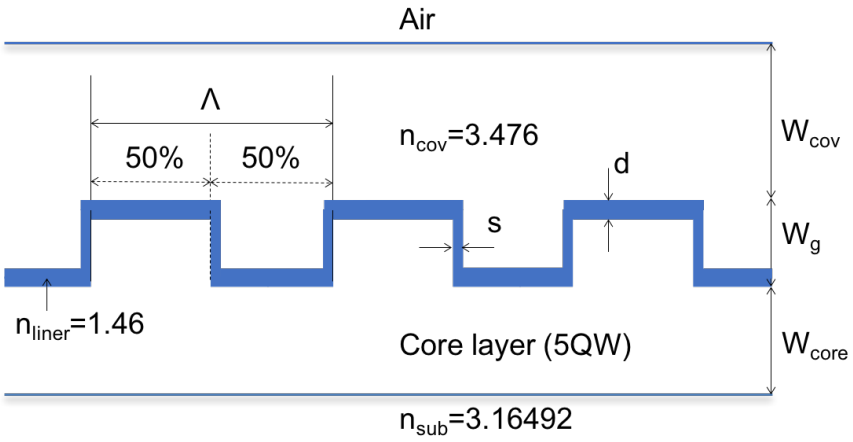

Figure 84. Sketch of a liner deposited at the top and bottom of a grating with a thickness of *d* and deposited on the sidewall of the grating with a thickness of *s*.

The plots in Figure 85 show the fraction of the incident power radiated down (P_{do}), the incident power radiated up (P_{up}), the incident power reflected (R), the incident power transmitted (T), the incident power radiated both upwards and downwards ($P_{do}+P_{up}$) and the sum of the incident power reflected, transmitted and radiated as a function of the wavelength. The grating length is 19.356 μm with 50% duty cycle. The 2nd Bragg grating period is 483.9 nm corresponding to a wavelength of 1550 nm. The maximum radiated power is 69.4% and the reflected power is less than 5% at the wavelength of 1580.4 nm, which is a reduction of ~ 5% from 73.6% power radiated with a 25-nm conformal liner layer for the same grating length,

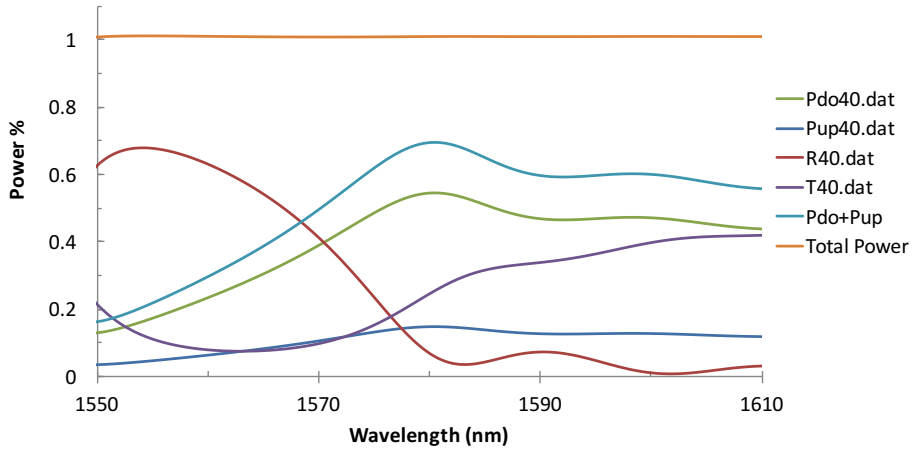

Figure 85. The power reflected, transmitted and radiated for the 5-QW grating outcoupler with a nonuniform liner thickness.

4.2.2. Different Amorphous Si cover Layer Configurations

4.2.2.1 A Non-Planar Conformal Cover Layer of 90 nm

The grating structure shown in Figure 86 has a continuous and uniform cover layer of 90 nm deposited on a liner layer of 25 nm. Except the thickness of the cover layer, the thickness of each layer and refractive index are the same as the final 5-QW ECS grating coupler in previous sections.

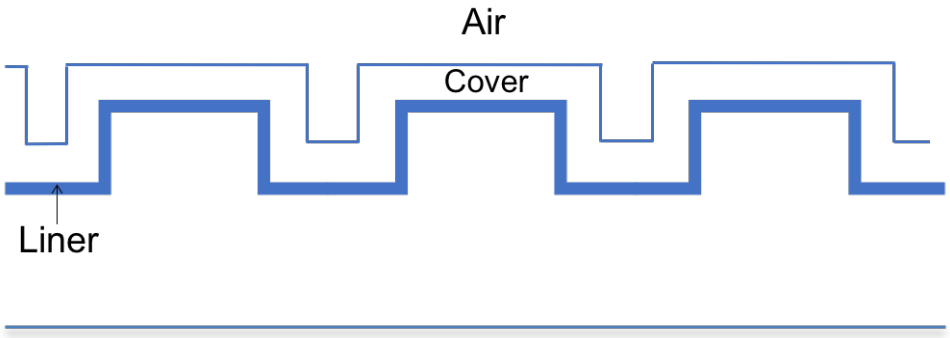

Figure 86. A conformal a-Si cover layer with a thickness of 90 nm.

The plots in Figure 87 show P_{do}, P_{up}, R, T, and the sum of the incident power reflected, transmitted and radiated as a function of the wavelength difference from 1550 nm. A great portion of the incident light is transmitted, and only 6% power of light is radiated upwards and downwards. A grating having this conformal cover layer of 90 nm is not an efficient outcoupler.

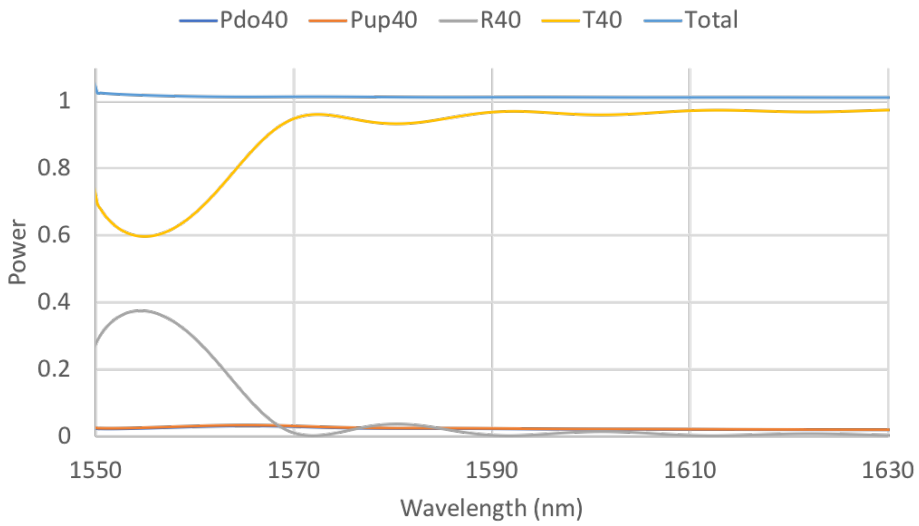

Figure 87. Power spectrum for a conformal a-Si cover layer with a thickness of 90 nm.

4.2.2.2 A Non-Planar Tooth Cover Layer of 230 nm

The grating structure shown in Figure 88 has amorphous silicon fills in the groove and deposits on the top of the tooth. The depth of the groove is 225 nm and the thickness of the amorphous silicon layer at the top of the tooth is 230 nm. The thickness and refractive index of each layer are the same as the final 5-QW ECS grating outcoupler considered above.

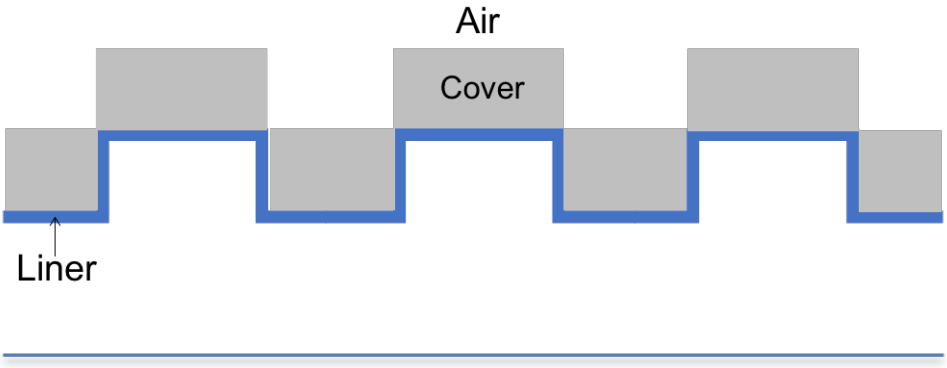

Figure 88. Sketch for a non-planar a-Si cover of 230 nm.

The plots in Figure 89 show P_{do}, P_{up}, R, T and the sum of the incident power reflected, transmitted and radiated as a function of the wavelength difference from 1550 nm. The maximum radiated power ($P_{do}+P_{up}$) is only 26.6%. This grating structure with this cover layer is not an efficient outcoupler.

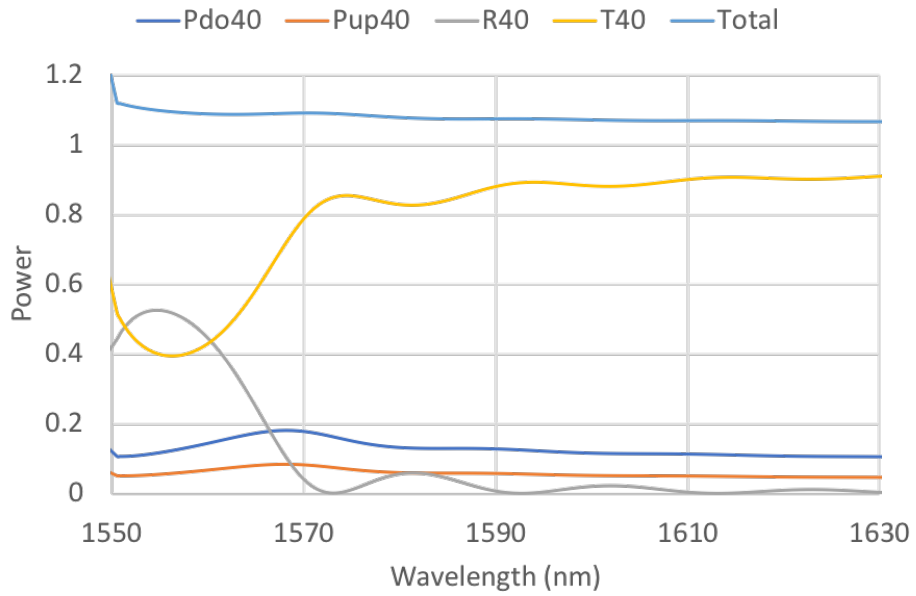

Figure 89. Power spectrum for a case of a non-planar cover with a thickness of 230 nm.

4.2.2.3 A Non-Planar, Thick Continuous Thick Cover Layer

The grating structure shown in Figure 90 has a continuous amorphous silicon (a-Si) cover layer deposited on a liner layer of 25 nm. The thickness of a-Si at the top of the tooth is 230 nm, and a-Si in the groove is 335 nm thick. Except for the thickness of the cover layer, the refractive index and thickness of each layer are the same as the final 5-QW ECS grating outcoupler considered above.

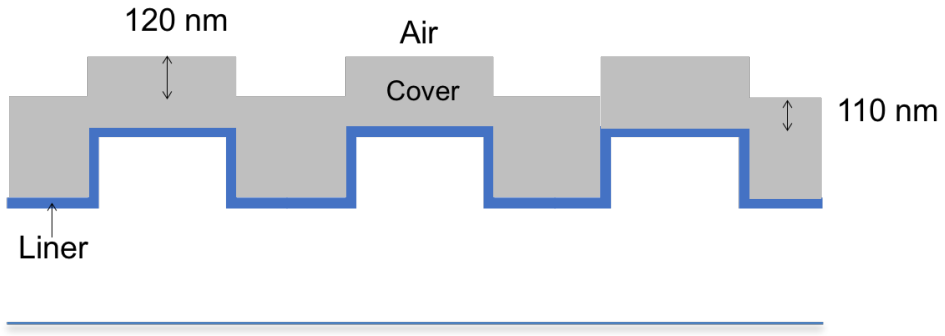

Figure 90. Sketch of a grating with a continuous, thick, non-planar a-Si cover layer.

The plots in Figure 91 show P_{do}, P_{up}, R, T and the sum of the incident power reflected, transmitted and radiated as a function of the wavelength difference from 1550 nm. The total power approaching 140% shows the error of the Floquet-Bloch approach around 1550 nm. However, the maximum radiated power is enhanced to 87% (67% P_{do} and 20% P_{up}) with a low reflected power (10%) at the wavelength of 1583 nm. Therefore, this grating cover configuration needs additional consideration.

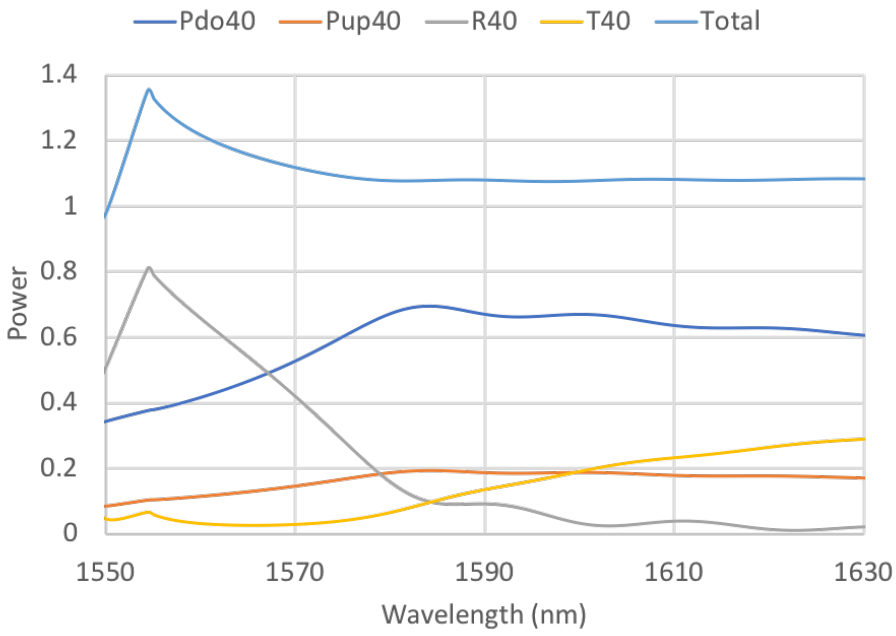

Figure 91. Power spectrum for a grating with a continuous thick cover layer.

4.3. 5-QW InP Outcoupler without ECS

In this section we compare an the final 5-QW ECS grating outcoupler to a standard 5-QW grating outcoupler. As discussed in the previous section, the grating in section 4 of Figure 75 without a high-index liner and low-index cover layer results in the waveguide being cutoff, so a conventional grating outcoupler is placed in transition section 2 of Figure 75 where the top of the grating is located at the surface of the 200-nm p-clad InP layer. The overlap integral of fields between the laser section and the conventional outcoupler is 81%, noticeably less than the overlap integral of fields between the laser section and the ECS coutcoupler of 94%.

Figure 92 shows the normalized reciprocal wavelength (Λ/λ_0) as a function of the normalized propagation constant ((β-K)/K) and the normalized attenuation ($\alpha\Lambda$) for an infinite standard grating outcoupler. The 2nd Bragg period is 484.9 nm at a wavelength of

1550 nm. The normalized attenuation coefficient for the typical outcoupler is 0.005 compared to 0.008 for the ECS outcoupler.

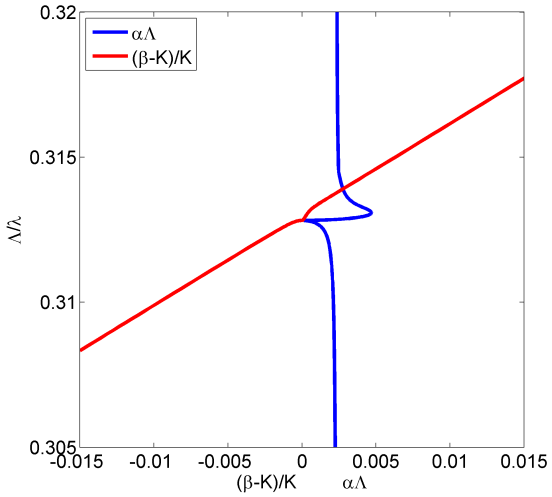

Figure 92. Plot of the normalized reciprocal wavelength as a function of the normalized attenuation and normalized propagation constant for the case with the standard grating outcoupler.

Figure 93 shows the power spectrum of the conventional grating outcoupler for a length of 19.5 μm at the operating wavelength of 1550 nm. The maximum radiated power is only 18% (6% P_{do} and 12% P_{up}) and over 80% of the incident power is transmitted. On the other hand, the maximum radiated power is 82% (79% P_{do} and 3% P_{up}) for the ECS outcoupler for the same grating length.

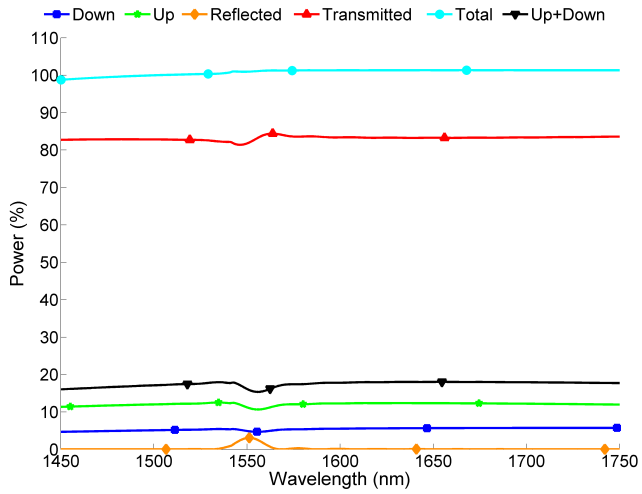

Figure 93. Plot of the power reflected, transmitted and radiated for a 5 QW conventional grating outcoupler with a grating length of 19.5 μm.

4.4. Loss Calculation

In this section, the doping profile for the final 5-QW laser/ECS grating structure is analyzed to obtain an internal modal loss below 2 cm^{-1}. High doping concentrations increase internal losses but reduce series resistance. The internal modal loss is related to the imaginary part of the effective index (the *WZI*) parameter in WAVEGUIDE III) and the wavelength of light

$$\alpha_m = WZI \cdot (4\pi/\lambda_0) \cdot 10^4 \qquad (49)$$

where the wavelength has units of micrometer, and the power loss shown above is in cm^{-1}.

Table 11. Initial baseline doping profile of each epitaxial layer.

Layer	Composition	Thickness (μm)
Air		--
Cap	InGaAs (1E19 doped)	0.100
Cap	InGaAsP (1E18 doped)	0.010
P-clad	InP (1E18 doped)	1.5
P-clad	InP (1E17 doped)	0.5
Space for grating	$In_{0.74}Ga_{0.26}As_{0.5}P_{0.5}$	0.2
SCH	$In_{0.74}Ga_{0.26}As_{0.5}P_{0.5}$	0.044
4x barriers	$In_{0.74}Ga_{0.26}As_{0.5}P_{0.5}$	0.008
5x QWs	$In_{0.74}Ga_{0.26}As_{0.81}P_{0.19}$	0.006
SCH	$In_{0.74}Ga_{0.26}As_{0.5}P_{0.5}$	0.044
N-clad	InP (1E18 doped)	2
N substrate	InP	--

Table 11 lists the initial baseline doping concentration of each epitaxial layer. The QWs, barriers, SCH (and the liner and cover layers for the outcoupler grating) are undoped. In this initial doping profile, the 100-nm InGaAsP cap layer is p-doped 10^{19} cm^{-3}, the 10-nm InGaAs cap layer and 1.5-μm p-clad layer are both p-doped 10^{18} cm^{-3}, the 0.5-μm p-clad layer is lightly p-doped 10^{17} cm^{-3}, and the whole n-clad layer is n-doped 10^{18} cm^{-3}. The field intensity and the index profile for structure in Table 11 are shown in Figure 94. The field is confined in the core layer and the confinement factor (Γ) of each layer is also indicated in Figure 94. The modal loss is 1.654 cm^{-1} and the 5-QW confinement factor is 5.09%. The lightly doped thickness of the 0.5 μm p-clad layer is near the SCH layer and the more highly doped 1.5 μm thick p-clad layer is near the p-contact cap layers.

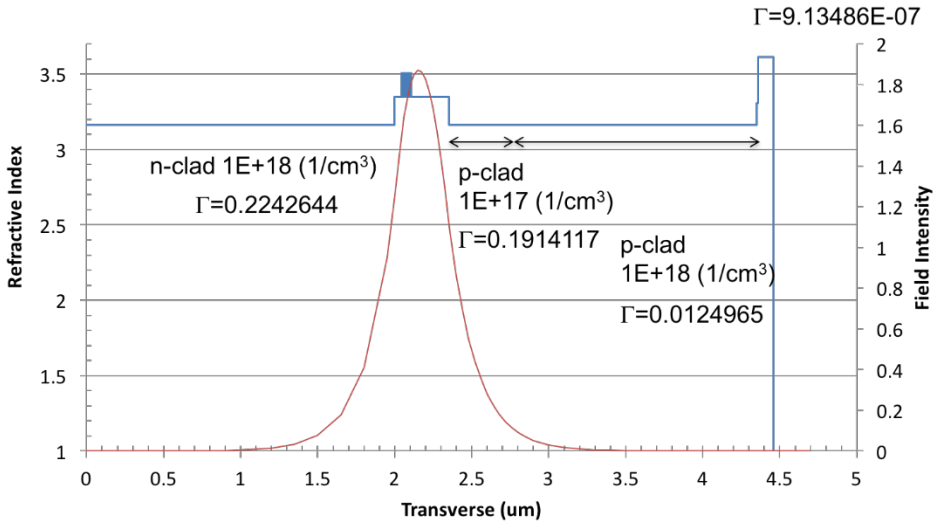

Figure 94. Field intensity and index profile for the baseline doping profile.

Figure 95 shows the modal loss as a function of the lightly doped (10^{17} cm^{-3}) p-clad thickness and the highly doped (10^{18} cm^{-3}) p-clad thickness. The sum of the lightly doped and highly doped thicknesses is 2 µm. The modal loss decreases as the light doped p-clad thickness increases up to 0.5 µm. Beyond 0.5 µm of the light doped p-clad, the modal loss isn't changed.

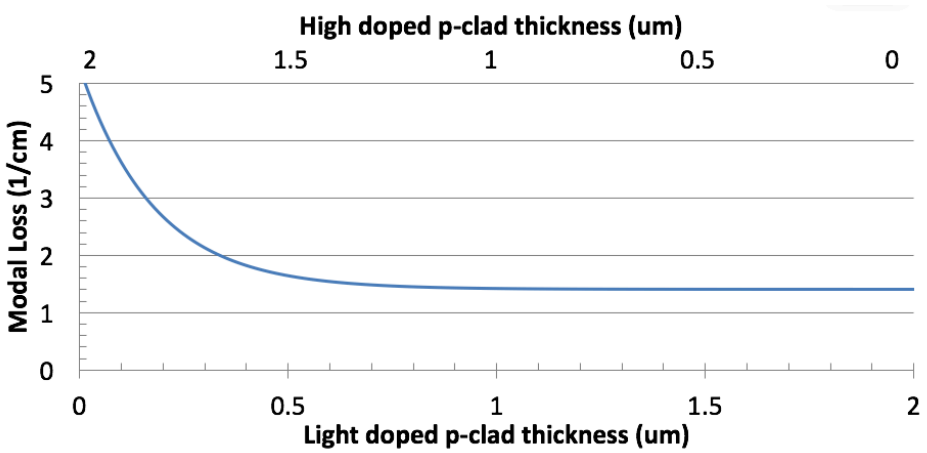

Figure 95. Modal loss as a function of the lightly doped p-clad thickness for the baseline doping profile.

A second doping profile, illustrated in Figure 96, has a lightly doped p-clad of 0.5 µm and 10 graded layers between the lightly and highly doped p-clad layer. These 10 graded layers are gradually doped from 10^{17} to 10^{18} cm^{-3} and the total thickness varies from 0.5 to 1.5 µm as shown in Figure 97. The maximum modal loss is 1.49 cm^{-1} where the total graded thickness is 0.5 µm.

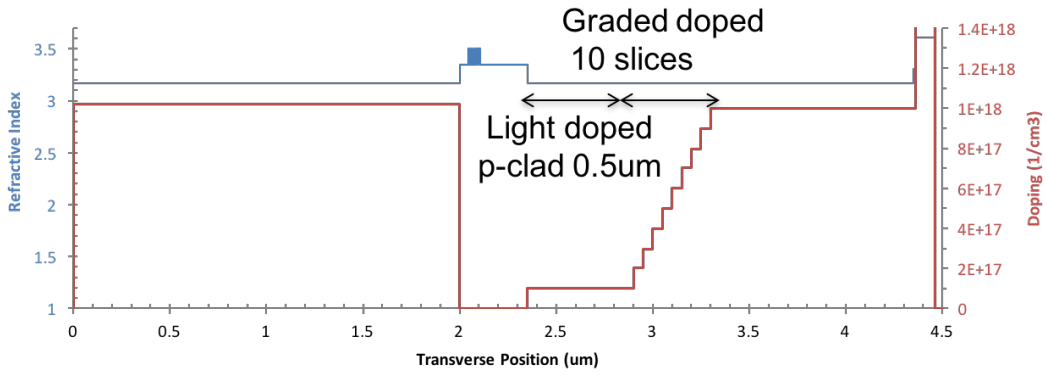

Figure 96. Refractive index and doping profile for the second p-doping profile.

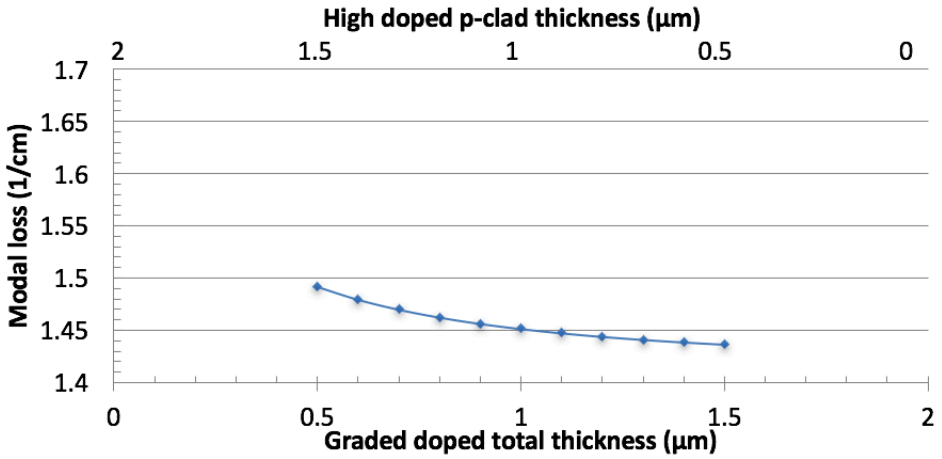

Figure 97. Modal loss as a function of the graded doped thickness for the second p-doping profile.

A third doping profile shown in Figure 98 varies the thickness of the uniform highly and lightly doped p-clad layers by varying the position of a 0.5 µm graded doping layer. The total thickness of the p-clad layer is fixed. As shown in Figure 99, the internal modal loss decreases as the light doped p-clad layer increases. Beyond the lightly doped p-clad layer thickness of 0.5 µm, the modal loss is constant (1.4 cm^{-1}).

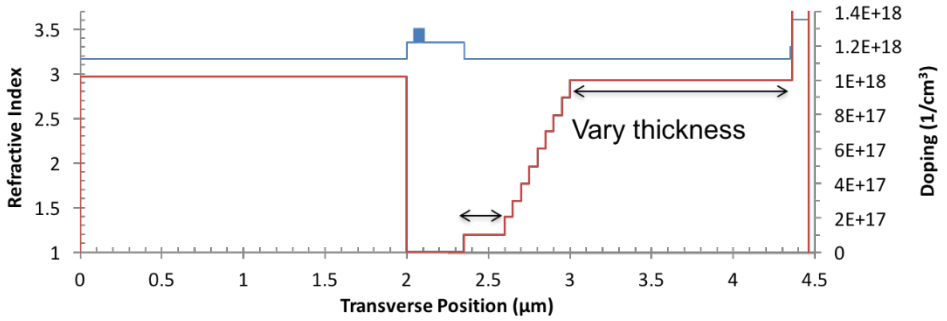

Figure 98. Refractive index and doping profile for the third p-doping profile.

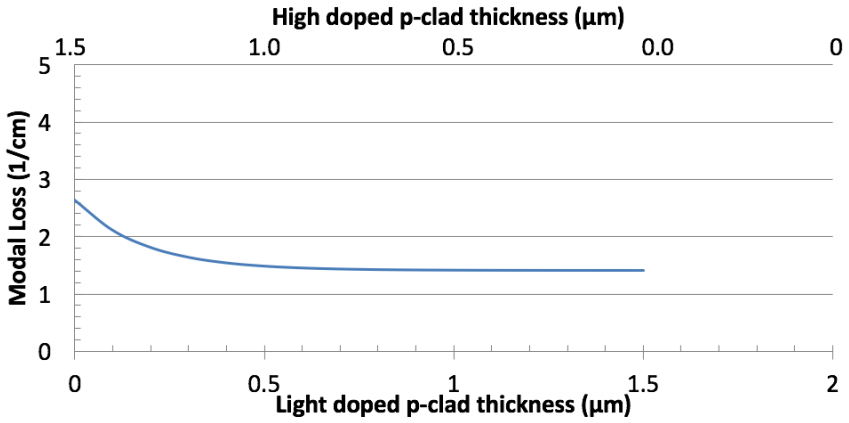

Figure 99. Modal loss as a function of the light doped p-clad thickness for the third p-doping profile.

As illustrated in Figure 100, a fourth doping profile varies the medium doped ($5x10^{17}$ cm^{-3}) and highly doped (10^{18} cm^{-3}) p-clad layer and fixes the thickness of the light doped p-clad layer at 0.2 µm. As the medium doped layer thickness increases, the modal loss is reduced. Beyond the medium doped layer of 0.7 µm, the modal loss is constant at 1.714 (cm^{-1}) as shown in Figure 101.

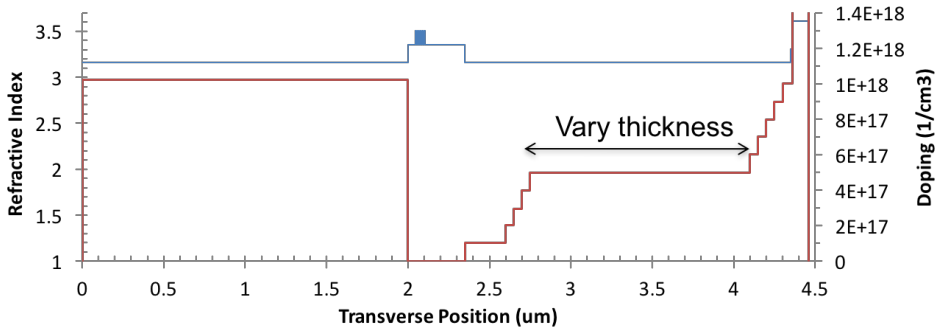

Figure 100. Refractive index and doping profile for the fourth p-doping profile.

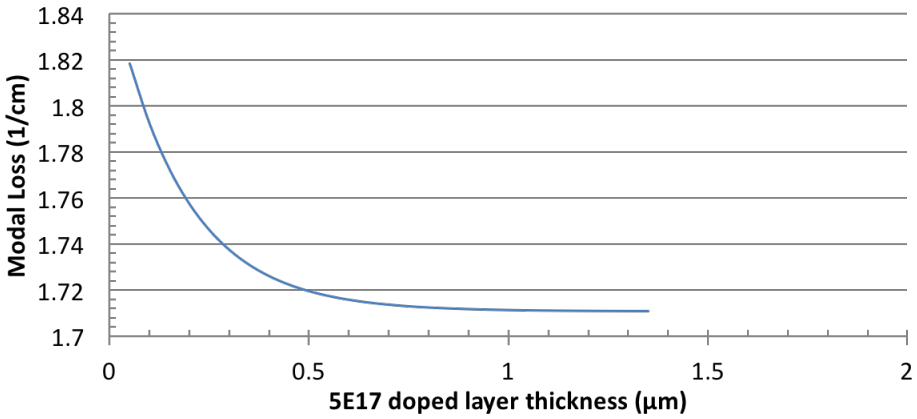

Figure 101. Modal loss as a function of the medium p-doped thickness for the fourth p-doping profile.

From the above considerations, the fourth p-doping profile is chosen as the best tradeoff between internal losses, series resistance and reduced electron-hole recombination in the p-cladding layers.

The n-side doping considers graded n-doped layers positioned adjacent to the undoped n-side SCH layer as shown in Figure 102. The graded doping range is from ($5x10^{17}$) to 10^{18} cm^{-3} within the thickness of 0.5 µm, which results in a modal loss of 1.37 cm^{-1}. As indicated in Figure 103, the modal loss is reduced as the graded n-doped layers are replaced by a constant n-doped ($5x10^{17}$) layer. Since low modal loss is a tradeoff with series resistance, the graded doping profile is chosen. Table 12 tabulates the final epitaxial layers and doping profiles for the 5-QW laser outcoupler.

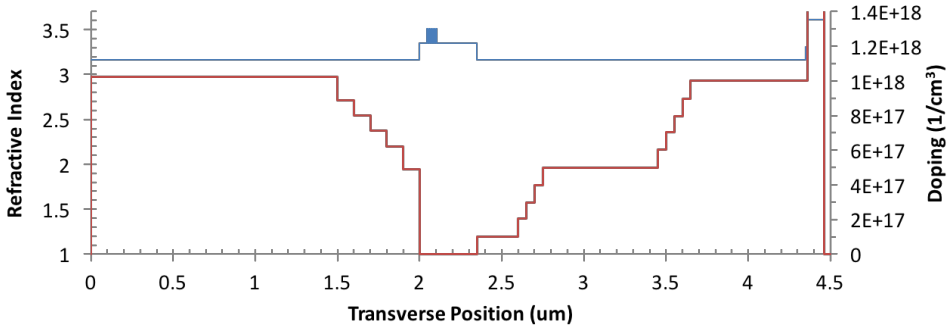

Figure 102. Refractive index and doping profile for the fifth doping profile.

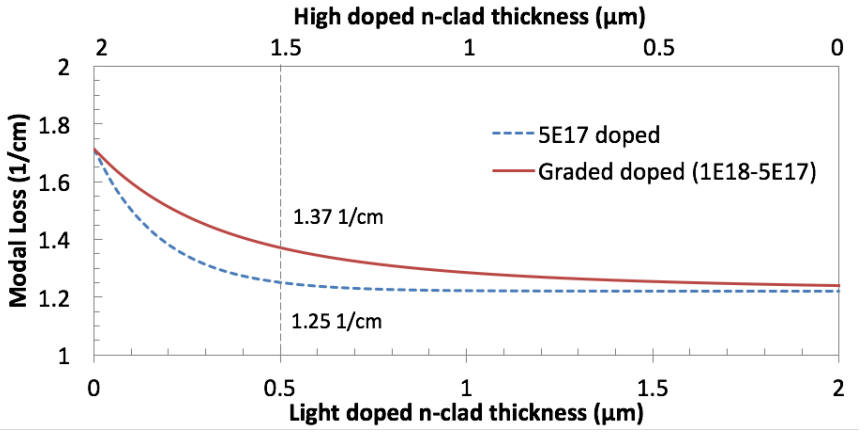

Figure 103. Modal loss as a function of the light doped n-clad thickness for the fifth doping profile.

Table 12. Final epitaxial structure for a 5-QW laser outcoupler.

Layer	Material	PL (nm)	Strain	x	y	Thickness (um)	Level (From substrate to the surface) (/cm^3)	Type
23	InGaAs					0.1000	> 1E+19	P+
22	InGaAsP	1300				0.0100	1.0E+18	P
21	InP					0.7000	1.0E+18	P
20	InP					0.3000	5E+17-1E+18	P
19	InP					0.5000	5.0E+17	P
18	InP					0.3000	1E+17-5E+17	P
17	InGaAsP	1300				0.0150	1.0E+17	P
16	InP					0.2000	1.0E+17	P
15	In(1-x)Ga(x)As(y)P(1-y)		-0.2%	0.260	0.500	0.2440	-	UID
14	In(1-x)Ga(x)As(y)P(1-y)		0.8%	0.260	0.810	0.0060	-	UID
13	In(1-x)Ga(x)As(y)P(1-y)		-0.2%	0.260	0.500	0.0080	-	UID
12	In(1-x)Ga(x)As(y)P(1-y)		0.8%	0.260	0.810	0.0060	-	UID
11	In(1-x)Ga(x)As(y)P(1-y)		-0.2%	0.260	0.500	0.0080	-	UID
10	In(1-x)Ga(x)As(y)P(1-y)		0.8%	0.260	0.810	0.0060	-	UID
9	In(1-x)Ga(x)As(y)P(1-y)		-0.2%	0.260	0.500	0.0080	-	UID
8	In(1-x)Ga(x)As(y)P(1-y)		0.8%	0.260	0.810	0.0060	-	UID
7	In(1-x)Ga(x)As(y)P(1-y)		-0.2%	0.260	0.500	0.0080	-	UID
6	In(1-x)Ga(x)As(y)P(1-y)		0.8%	0.260	0.810	0.0060	-	UID
5	In(1-x)Ga(x)As(y)P(1-y)		-0.2%	0.260	0.500	0.0440	-	UID
4	InP					0.5000	1E+18-5E+17	N
3	InP					0.4000	1.0E+18	N
2	InGaAsP	1300				0.0150	1.0E+18	N
1	InP					1.1000	1.0E+18	N
InP n substrate 1.0E+18 or greater								

4.5. Broad-Area and Ridge-Guide Laser Characterization

1550nm 5-QW broad-area lasers grown to the specifications in Table 12 were fabricated to determine the initial performance. The cap layers, InGaAs and InGaAsP, were etched to form a laser stripe 100 μm wide. The p-metals were deposited on the stripe for the contact. On the n-side, the wafer section was thinned to about 125 μm followed by an n-metal deposition. The wafer piece was then cleaved into various lengths of laser stripes which are 250, 500, 750 and 1000 μm long.

The threshold current density, maximum optical power, and L-I slope were extracted from the Light-Current-Voltage (LIV) measurements. All the broad-area laser stripes are measured with current pulse width of 2 μs and a 0.2% duty cycle at 20 °C.

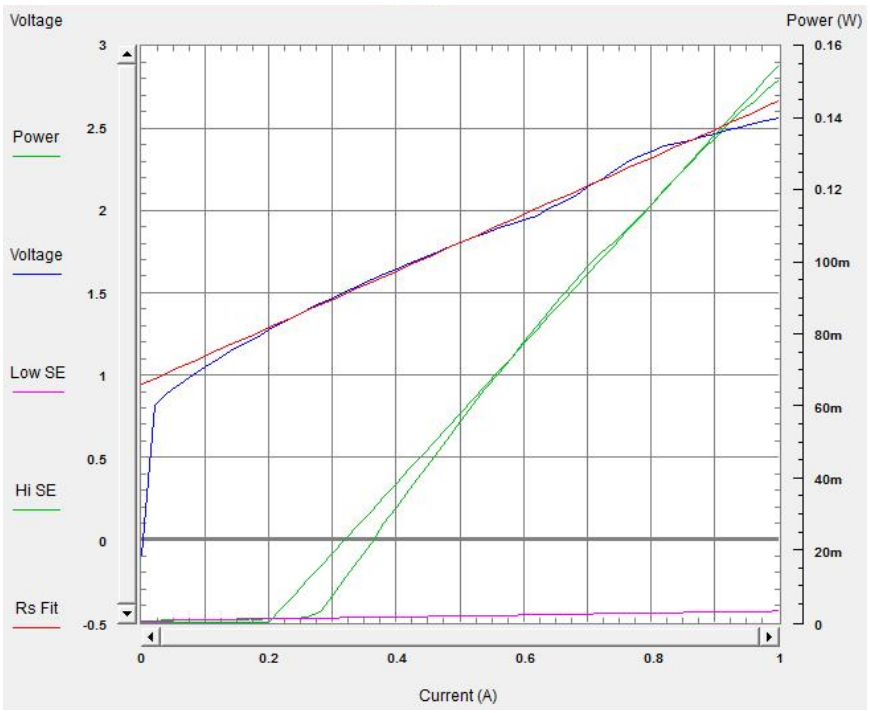

Figure 104. LIV curves for a BA device with a 250-µm length.

Both edge facets of the board-area laser stripe emit light, but light is detected only at one edge facet of the broad-area stripe. Figure 104 shows the LIV curves for a 250 µm long device as the current is applied from 0 to 1 A. The threshold current is 255 mA which corresponds to a threshold current density of 1020 A/cm^2 (length is 250 µm and the width is 100 µm). The maximum optical power is 150.7 mW at a current of 1 A. The slope is 0.1937 W/A. According to the slope of the IV curve, the series resistance of this device is 1.722 Ω.

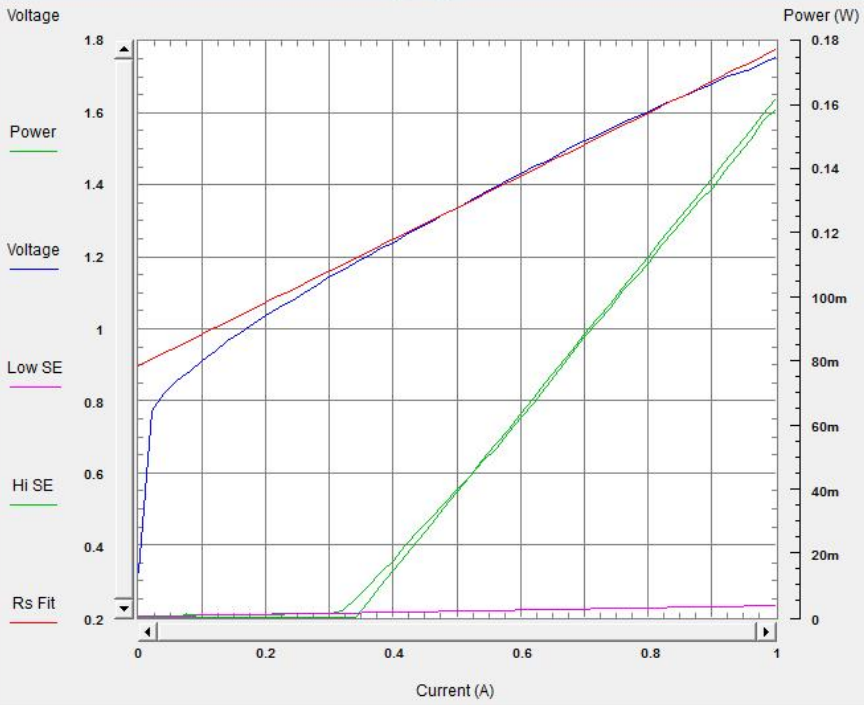

Figure 105. LIV curves for a BA device with a length of 500 µm.

Figure 105 shows the LIV curves for the broad-area laser with 500 µm in length. The threshold current is 310 mA which corresponds to a the threshold current density of 620 A/cm^2. Furthermore, the maximum optical power is 158.9 mW at a current of 1 A. The slope of the L-I curve is 0.2456 W/A, and the series resistance of this device is 0.8788 Ω.

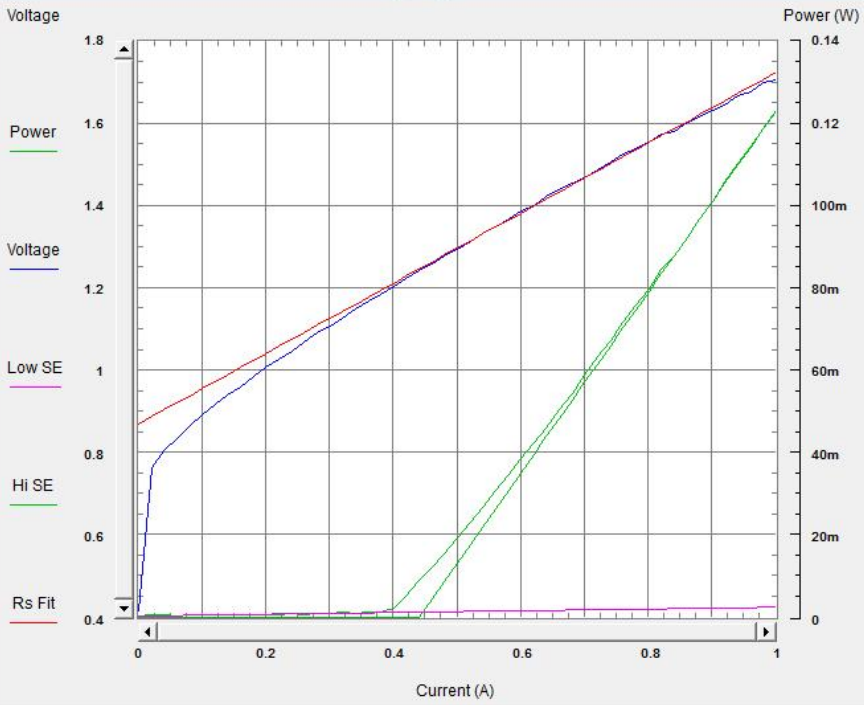

Figure 106. LIV curves for a BA device with a length of 750 µm.

The curves in Figure 106 show the LIV characteristics for the broad-area laser having a length of 750 µm. The threshold current is 375 mA, corresponding to a threshold current density of 500 A/cm^2. The maximum optical power 122.9 mW at a current of 1 A. The slope of the LI curve is 0.2199 W/A. According to the slope of the IV curve, the series resistance of this device is 0.854 Ω.

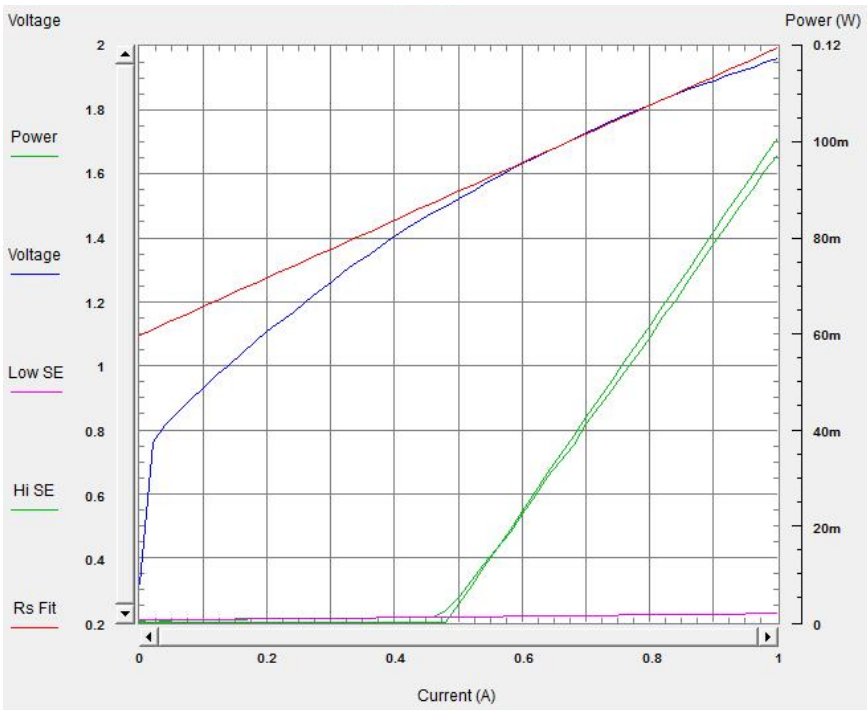

Figure 107. LIV curves for a BA device with a length of 1000 µm.

Figure 107 shows the LIV curves for a broad-area laser with a length of 1 millimeter. The threshold current is 463 mA which corresponds to a threshold current density of 463 A/cm^2. The maximum optical power is 97.45 mW at a current of 1 A. The slope of the LI curve is 0.1914 W/A, and the series resistance of this device is 0.8988 Ω.

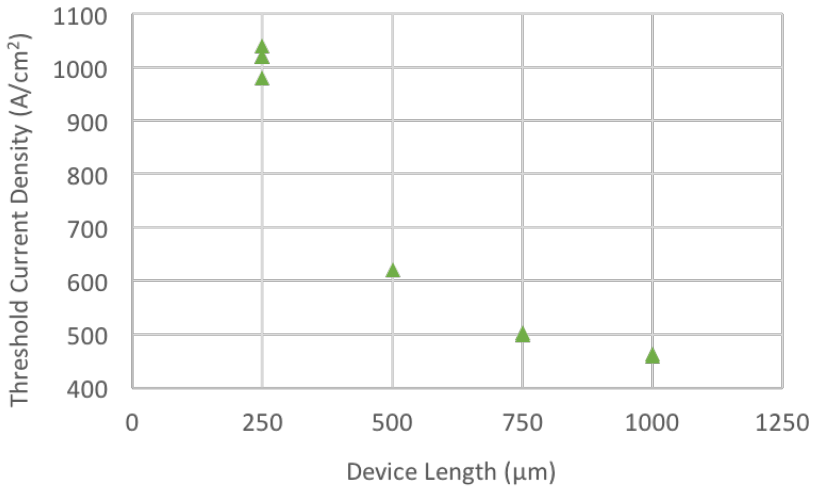

Figure 108. Threshold current density as a function of the length of the BA laser stripe.

Figure 108 shows the threshold current density as a function of the length for the 5-QW board-area lasers and shows a dramatic reduction with increasing device length.

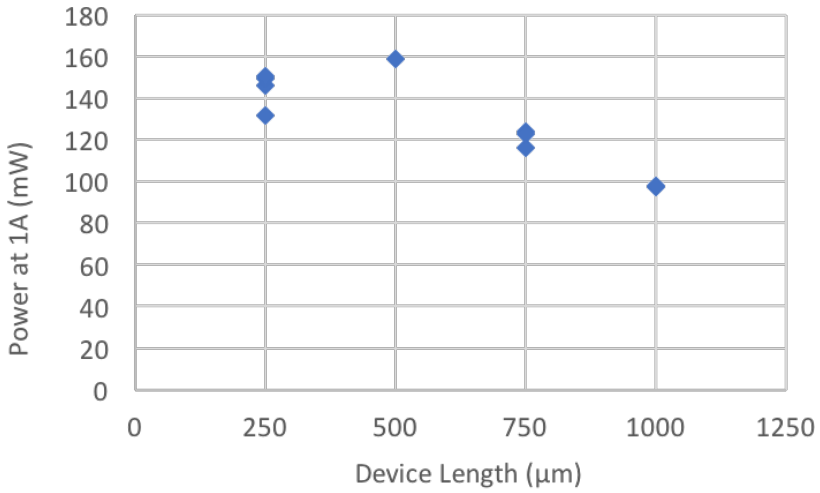

Figure 109. Maximum optical power as a function of the length for the BA laser stripe.

The plot in Figure 109 shows the optical power as a function of the length for the 5-QW board-area lasers at an applied current of 1 A. The maximum optical power occurs for a length near 500 µm.

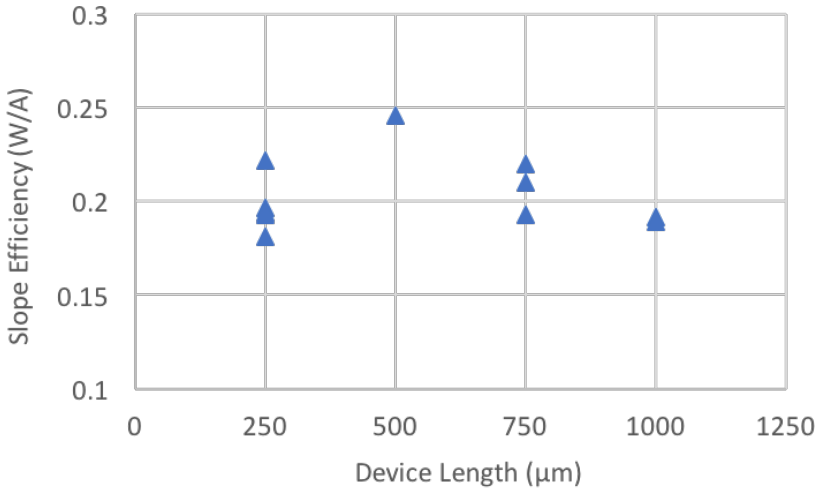

Figure 110. L-I slope as a function of the length of the BA laser stripe.

Figure 110 shows the slope of the LI curve as a function of the broad-area laser length for the 5-QW structure. The maximum slope efficiency is 0.2456 W/A when the length of the broad area laser is 500 µm.

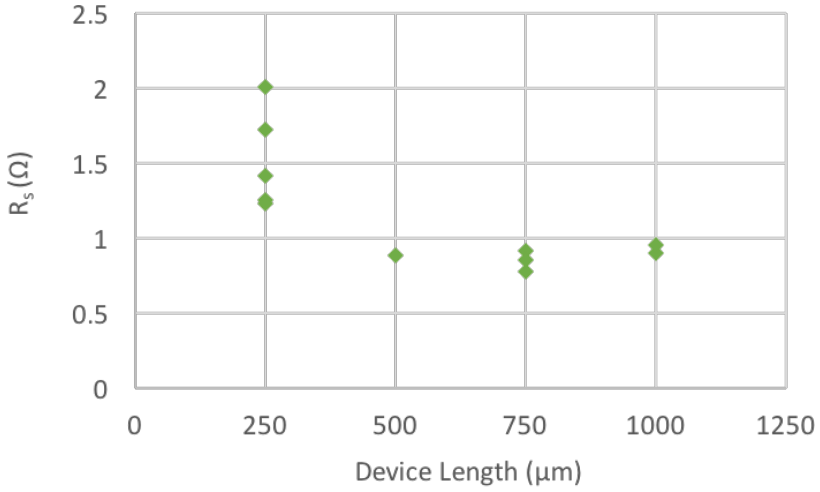

Figure 111. Series resistance as a function of the length of the BA laser.

Figure 111 shows the series resistance as a function of length for the 5-QW broad area lasers. The series resistance is below 1 Ω for lengths of 500 μm and longer. Figure 112 shows the plot of light intensity as a function of the wavelength for the 5-QW BA lasers.

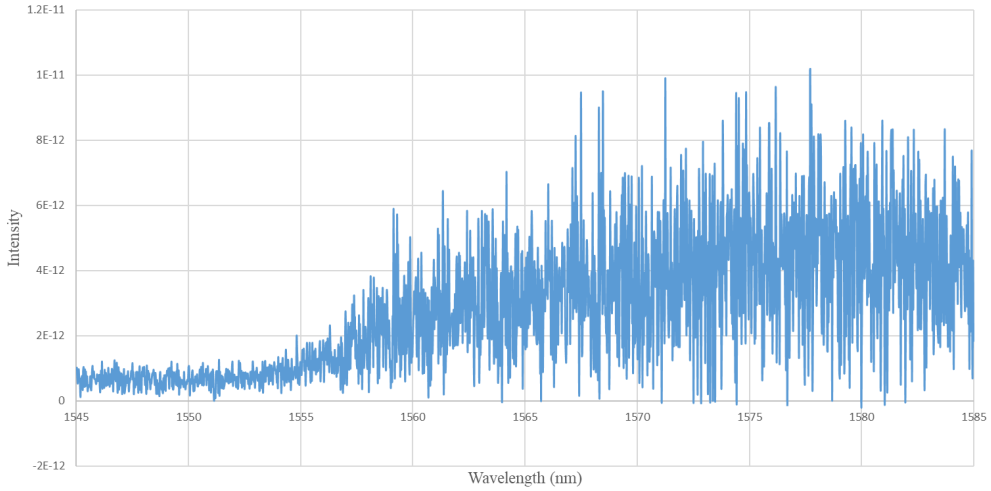

Figure 112. Linear plot of light intensity as a function of wavelength for the 5-QW BA lasers.

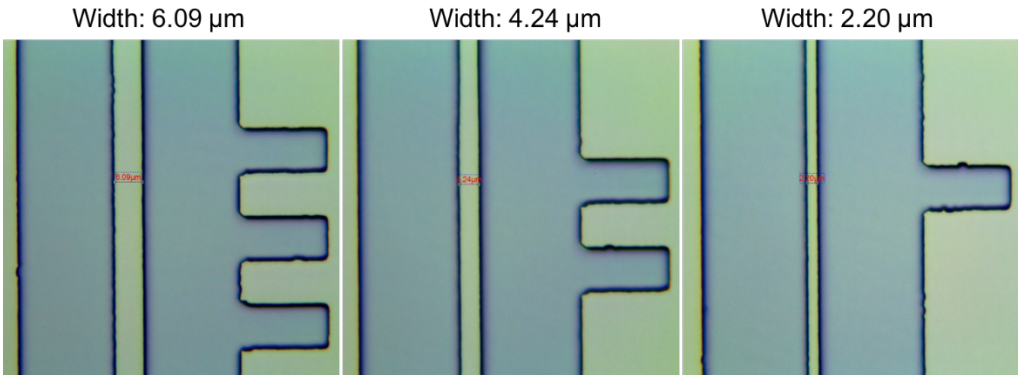

Figure 113. Different ridge widths after etching.

The 1550 nm 5-QW laser material was also fabricated into ridge-guide lasers. The layers above layer 17 in Table 12 are etched off to achieve a lateral index of 0.015 in the gain region as illustrated in Figure 74. The mask layout has 3 different ridge widths: 2.2, 4.24, and 6.09 µm as shown in Figure 113.

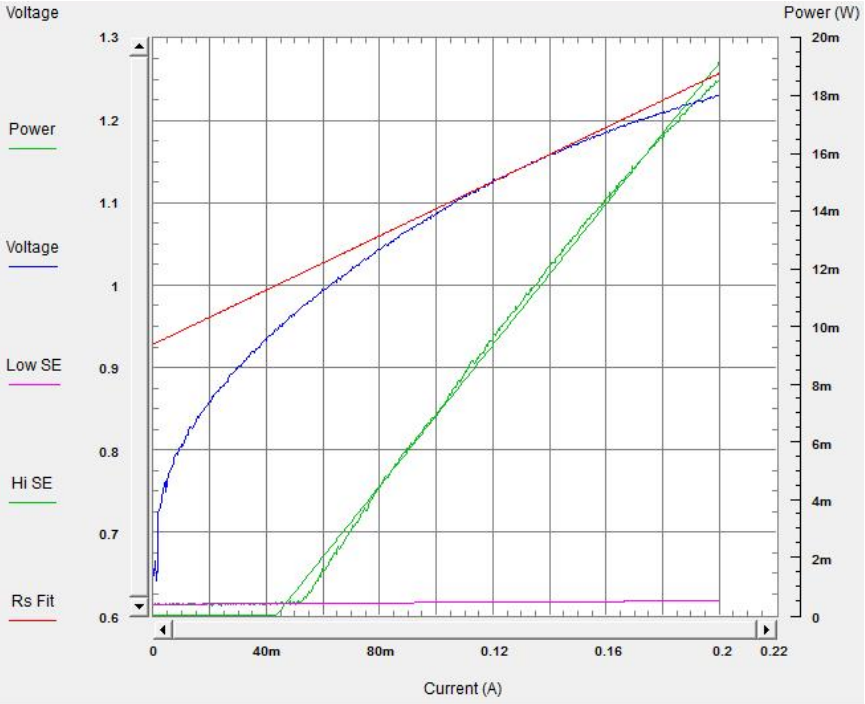

Figure 114. LIV curves for a RG laser with a width of 6.09 µm and a length of 1.5 mm.

The RG lasers were cleaved into lengths of 1 and 1.5 mm and measured at the bar level with a current with a pulse width of 2 µs and 0.1% duty cycle at 25 °C. Figure 114 shows the LIV curves for a 6.09-µm wide and 1.5-mm long laser ridge and shows a maximum optical power of 18.6 mW at 0.2 A. The slope of the LI curve is 0.1224 W/A and the series resistance is 1.645 Ω. Figure 115 (a) through (c) shows the series resistance, the threshold current density, and the slope of the LI curve as a function of the area which

is defined by the width and length of a ridge stripe. The larger area (longer length) ridge lasers generally have better performance.

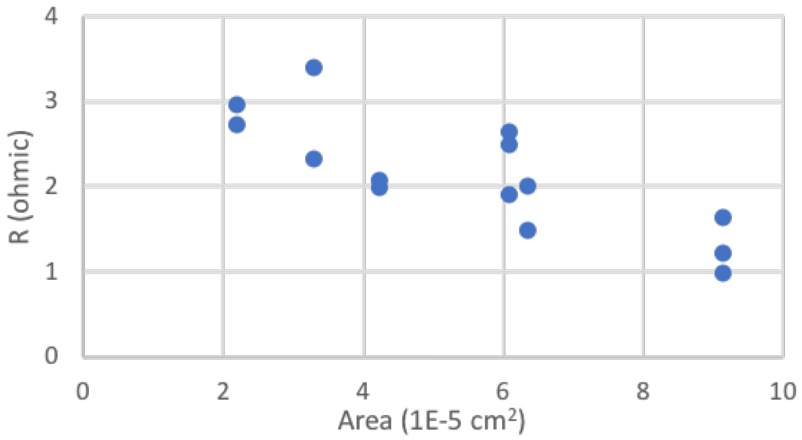

(a)

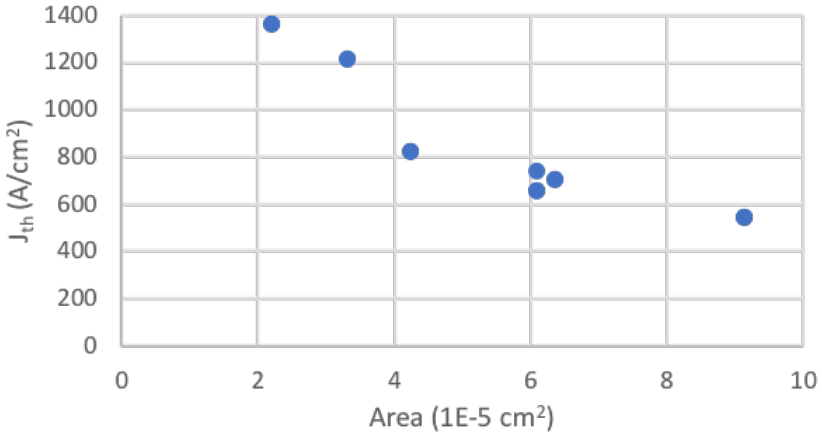

(b)

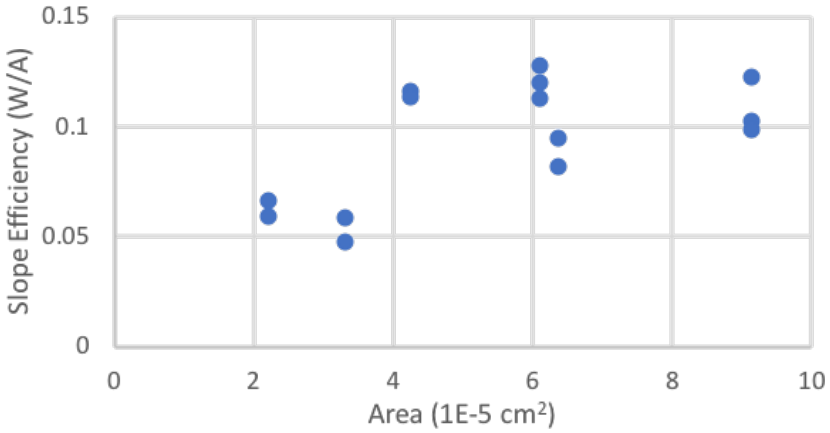

(c)

Figure 115. (a) Series resistance, (b) threshold current density, and (c) slope efficiency as a function of area for a RG laser.

4.6. InP and InGaAsP Grating Pattern

Prototype ECS gratings for outcouplers and DBRs were fabricated by e-beam writing at the UW Washington Nanofabrication Facility (WNF). The gratings were etched by inductively coupled plasma (ICP) etching using silicon nitride as a hard mask. Figure 116 and Figure 117 demonstrate the quality of the curved grating and flat grating in InGaAsP. WNF also deposited conformal thin silicon dioxide coatings over the gratings as shown in Figure 118. The SiO_2 sidewall is uniform and about half the thickness of the top coating.

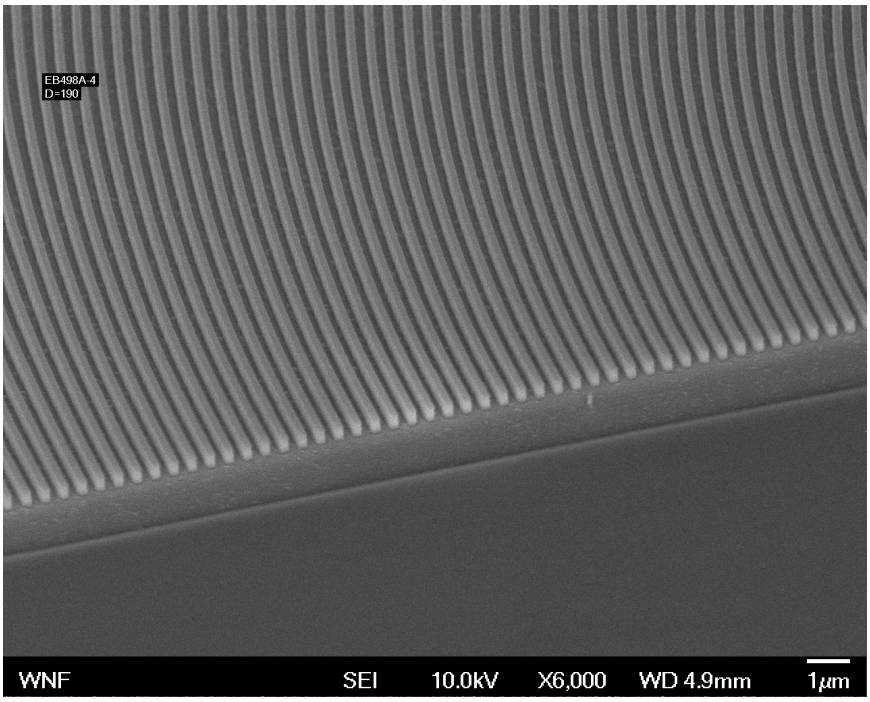

Figure 116. Curved, tapered grating etched in InGaAsP which increases the lateral spot size from ~5 μm in the ridge guide region to ~10 μm in the outcoupler region.

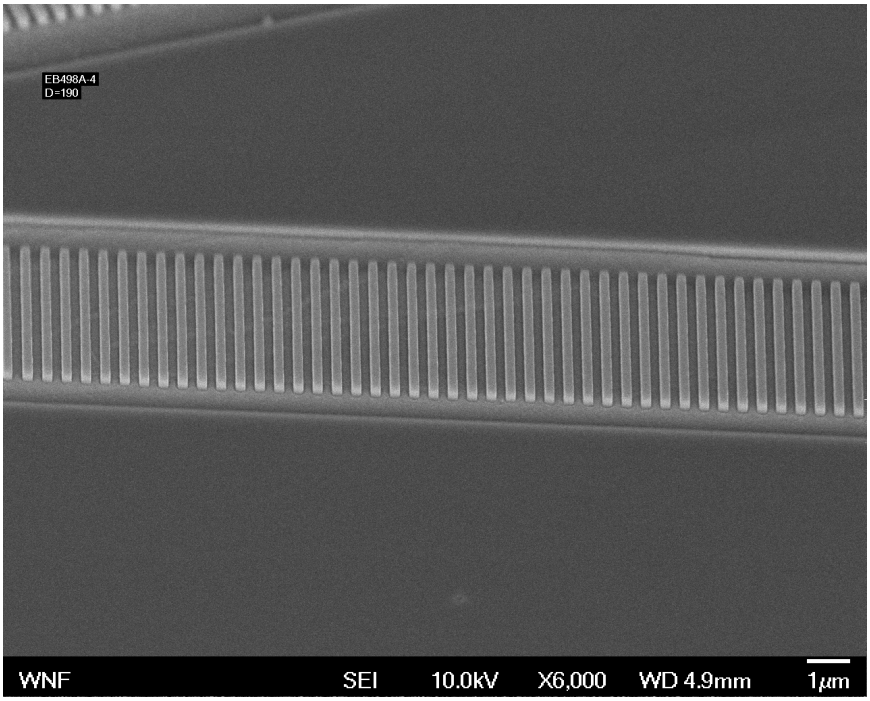

(a)

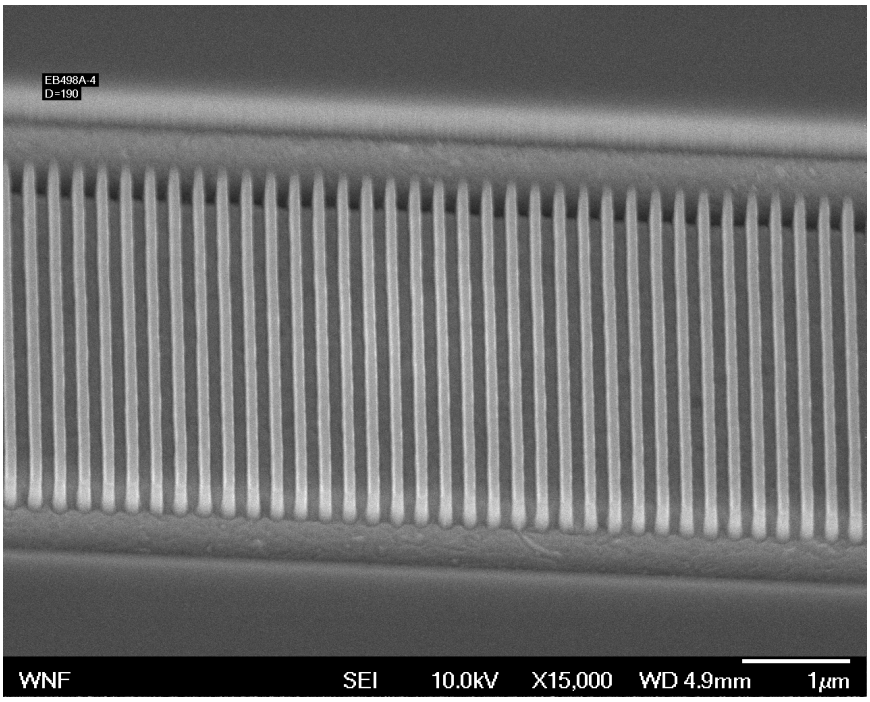

(b)

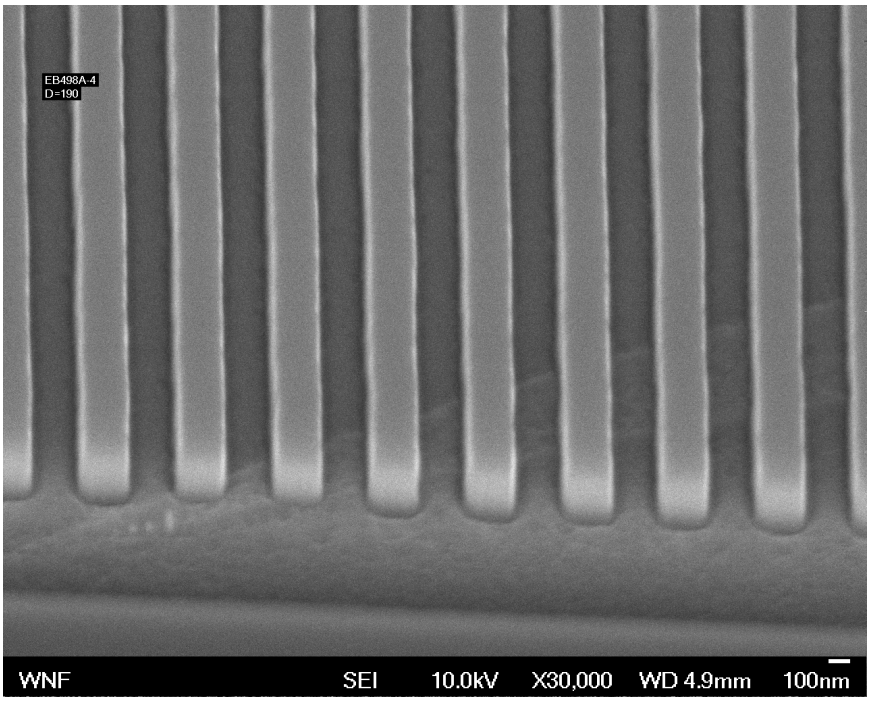

(c)

Figure 117. SEM micrographs of planar DBR gratings etched in InGaAsP at different magnifications.

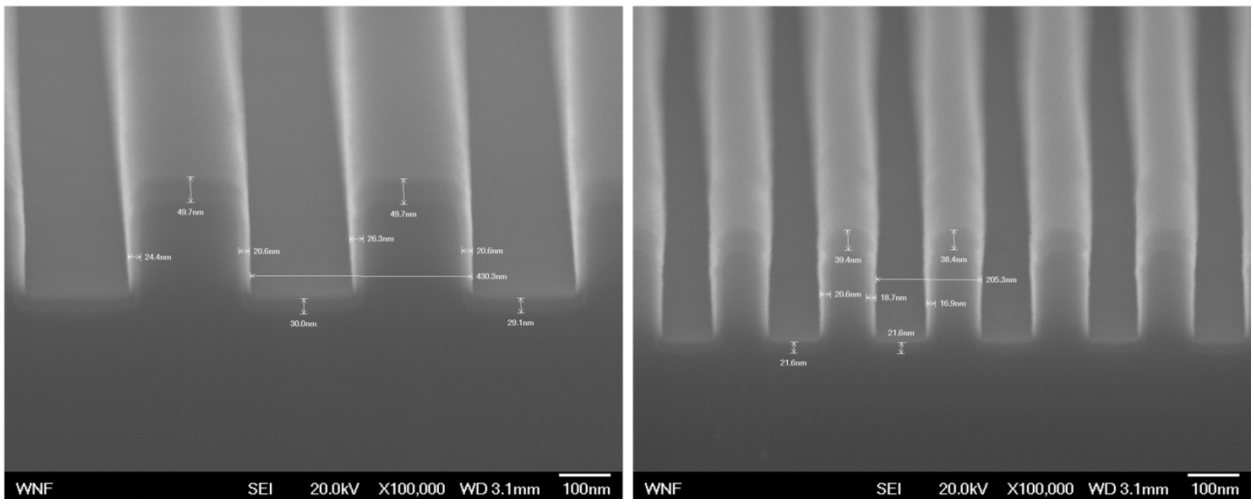

Figure 118. SEM micrograph of a conformal SiO_2 cover layer over a grating.

4.7. Conclusion

In this chapter, we have determined the epitaxial layers and doping profiles for an integrated ECS outcoupler and 5-QW ridge guide DBR laser. The location and length of the ECS DBR and ECS outcoupler were determined to maximize outcoupled light. The ECS outcoupling performance was compared with a conventional outcoupler. The low-index liner and high-index cover layer deposited on the grating also minimizes both reflections and radiation losses at interfaces between the laser section, transition sections and the grating section. Other configurations of the SiO_2 liner and a-Si cover layer on grating were also considered. The method used to determine the doping profile for the 5-QW laser structure was discussed. Experimental results of the BA and RG lasers were presented.

Chapter 5

CONCLUSIONS AND FUTURE WORK

Addition of a thin, low-index liner layer over a surface grating combined with a high-index layer can result in short, efficient couplers for III-V waveguides with performance similar to grating couplers in silicon photonic waveguides. The same low-index liner and high index cover layer can also minimize reflections at transitions between sections of photonic integrated circuits or between a laser region and a DBR or grating coupler region.

To demonstrate these advantages, a two-dimensional grating with a uniform period and a uniform duty cycle has been analyzed. Adding a tapered region to laterally expand the width of the ECS coupler (Figure 30) along with tailoring the duty cycle and period of the coupler in the manner described in [2] increases the coupling efficiency to fibers and many other optical elements.

To maximize outcoupling and minimize back reflections, the grating period of the out coupler should be chosen to provide a 15 to 150 nm shift from the wavelength that corresponds to the exact second Bragg condition.

A detailed design of such an ECS grating integrated with a 9-QW and 5-QW laser structure emitting at a wavelength near 1550 nm has been presented. Both designs allow outcoupling of greater than 70% of the emitted light in a distance of ~ 20 μm in a single

pass, which is a reduction of outcoupler grating length in such III-V waveguides by a factor of 50 or more compared to conventional grating outcouplers.

We have validated the SMU grating software based on the Floquet-Bloch approach by comparing our results on grating couplers in silicon photonics waveguides to those published using the eigenmode expansion method [2], [37], [38], along with comparing our results on ECS gratings to the results using commercial FDTD software for InP based ECS grating couplers.

The ECS method has applications to second-order grating couplers in silicon photonics waveguides and glass waveguides in addition to the type of compound semiconductor waveguides that are used for semiconductor lasers and other photonic integrated components.

The ECS approach also allows designing a second-order grating that has near 100% reflection with insignificant outcoupling. Such a grating can provide equivalent performance at twice the grating period as a first order DBR grating, allowing the holographic fabrication of low-loss reflective gratings to laser wavelengths below 400 nm from the previous limit of about 800 nm.

Some of the work described in this thesis is included in a patent filed in [39]. A patent describing the integration of a short laser section with both an electroabsorption modulator (EAM) and an ECS outcoupler grating has been issued [40]. Such a device promises a low cost, low energy per bit optical source capable of modulation rates beyond 100 Gbps for broad-bandwidth telecommunication systems [41], data and server farms, and high performance computers.

Further work related to ECS gratings includes experimental demonstrations of ECS gratings integrated with lasers and with lasers and modulators. Such work is currently in progress at SMU.

Additional further work will explore the ECS and other grating designs to obtain grating characteristics such as extremely narrow or extremely wide reflectivity and outcoupler spectrums. Although the results have not been included in this thesis, initial work on ECS gratings with duty cycles other than 50% show promising characteristics.

APPENDIX

A1. Mask Design for an ECS Tapered Grating Outcoupler with a DBR Laser

The photo mask is designed for the fabrication at SMU, the E-Beam grating process at UW, and also accommodate Oracle to align to their silicon photonic circuit. The layout should meet the requirement of both Oracle and UW. There are total 10 masks needed to be done for ECS laser devices. Figure 119 shows a unit of the ECS laser device. There is a long DBR grating on the back side of the laser ridge to reflect 90% of light and a taper outcoupler at the front to couple the light out of the surface. One side of the channel is etched down to the substrate to make the n-contact on the same surface as the p-contact.

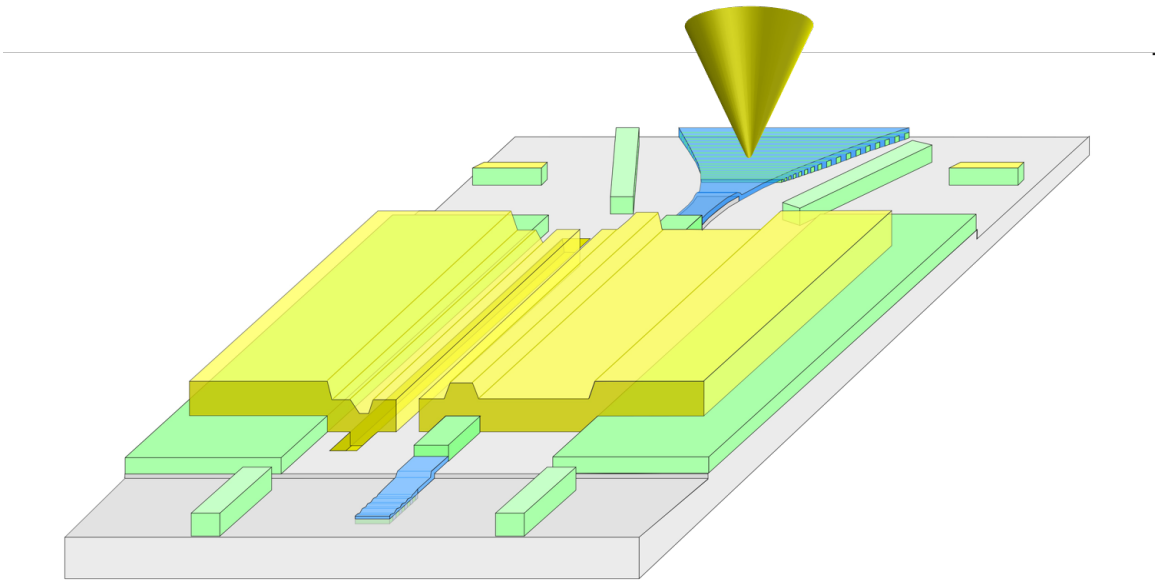

Figure 119. Integrating of an ECS tapered grating outcoupler with a ridge guide laser followed by a DBR grating.

The first mask is to define laser ridges, the location of DBR and outcoupler gratings, and alignment marks for SMU, UW and Oracle. As shown in Figure 120(a), mask 1 defines a ridge guide laser with the width of 5.5 µm and the various lengths of 300, 400, 500, 600, 700, and 800 µm, a window of 400 µm long for the DBR grating process and a window of 80 µm long for the outcoupler grating process. The pitch of each device is 250 µm. As shown in Figure 120(b), the SMU cross alignment mark set in every 3 mm is for the fabrication done at SMU, the L shape of alignment mark set is for the grating fabrication done at UW, and a small cross and a set of bar alignment marks are for the alignment purpose as Oracle group align our chip to their silicon circuit.

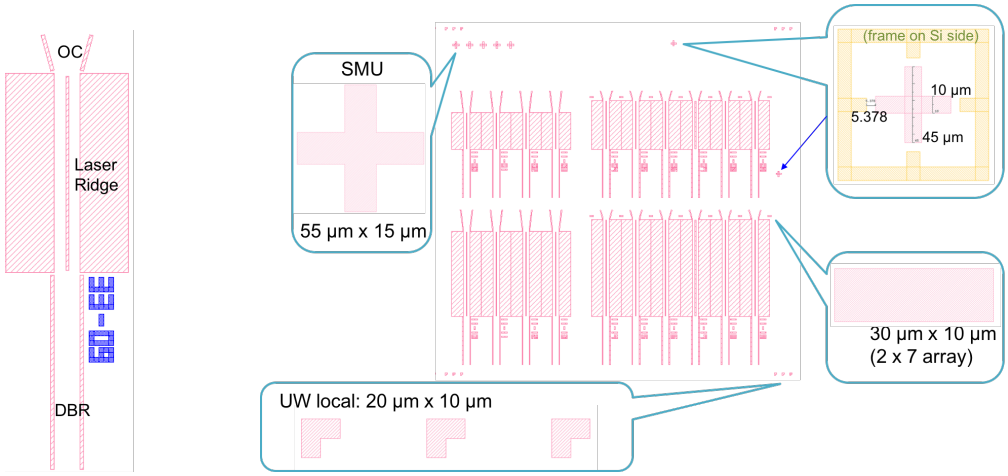

(a) (b)

Figure 120. (a) An unit of the ECS laser and (b) alignment marks surrounding devices.

The 2nd mask layout is to define the outcoupler level. Since the level of outcoupler gratings is not as same as the level of laser ridges defined in mask 1, we need to etch down to reach where the outcoupler level should be. In Figure 121, the slash trapezoids open

windows to etch down to where the outcoupler grating would be. Once this level is done, the wafer sections are ready to send to UW for the grating fabrication of DBRs and outcouplers.

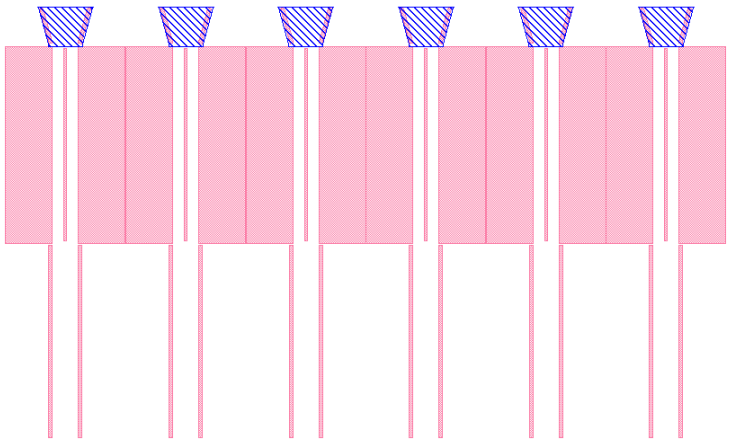

Figure 121. Mask 2 layout to define the outcoupler level.

The blue features shown in Figure 122 is the grating patterns for outcouplers and DBRs. The fan features with 6 different grating lengths and widths are the 2nd order Bragg gratings to couple the light out of the surface from the laser ridge. The blue grating ridges on the back of laser ridges are the 1st order Bragg gratings to 90% reflect the light with the narrow bandwidth of frequency.

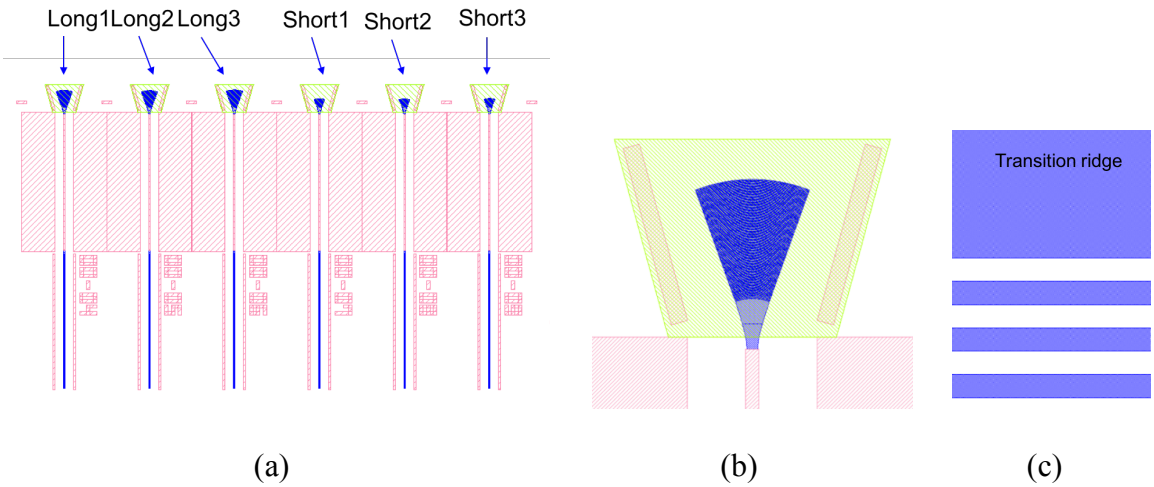

(a) (b) (c)

Figure 122. (a) The grating mask for DBRs and outcouplers, (b) the outcoupler grating pattern and (c) the DBR grating pattern.

Once the gratins are fabricated, the thin silicon dioxide and amorphous silicon are deposited on the wafer sections. The blue patterns in Figure 123 is to protect the oxide and amorphous silicon layers on the gratings then the rest of oxide and amorphous silicon are etched.

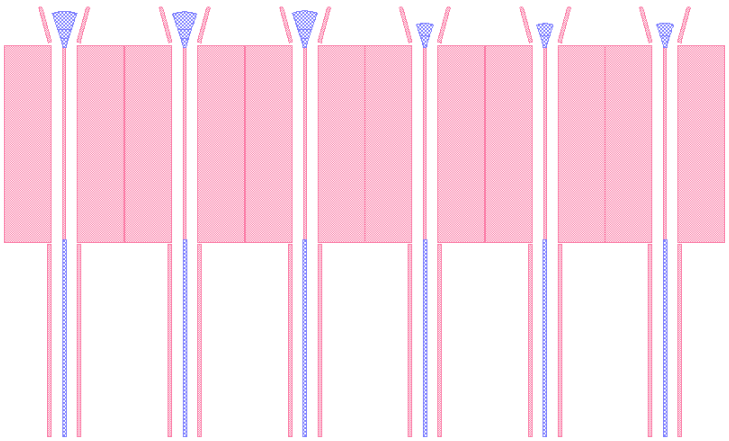

Figure 123. Mask 3 to etch oxide and amorphous silicon.

The next level is to pattern the n-well which is the blue slash rectangle shown in Figure 124. The n-well is etched down to the substrate to make n-contact on the top surface of the wafer as same as the p-contact. The dimensions of the n-well are 15 μm wide and 10 μm longer than laser ridges.

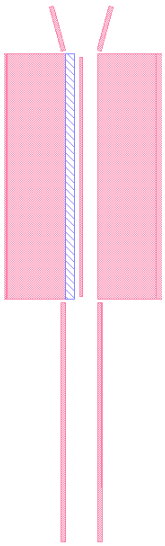

Figure 124. Mask 4 to etch n-well for contact

Once n-wells are etched through the substrate, the nitride is deposited for the passivation. The next step is to etch the nitride only on the top of n-well. In Figure 125(b) the green rectangular feature, the nitride opening window, is within the feature of the n-well.

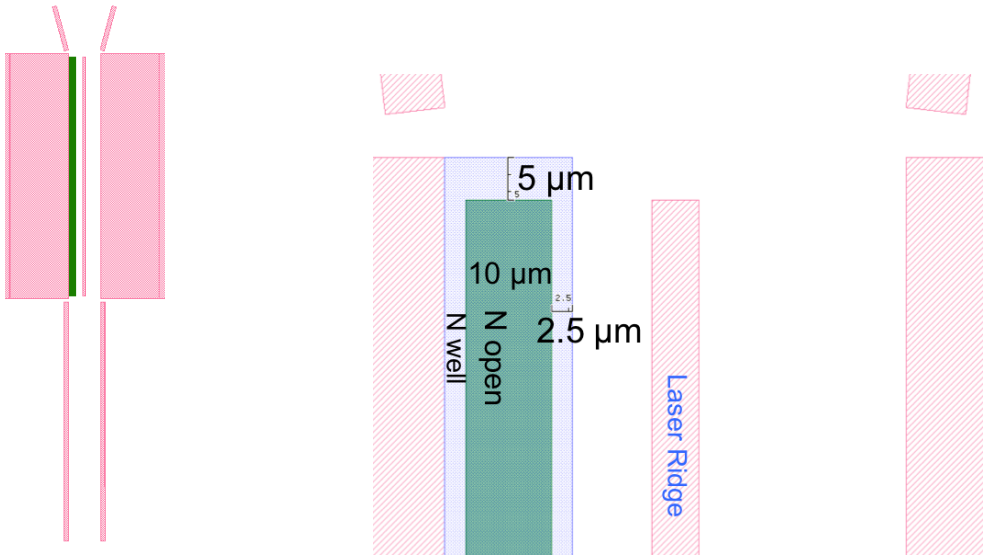

(a) (b)

Figure 125. (a)Mask 5 to open nitride for contact and (b) a close-up to view the n-opening window within the n-well.

The nitride on the top of laser ridges is also needed to be removed for the p-contact. The self-align process is to protect anywhere except the top of laser ridges as the slash black rectangle in Figure 126 then we etch the nitride on the top of that.

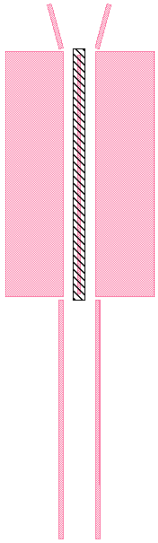

Figure 126. Mask 6 for self-align.

As the nitride within n-wells and on the top of p side of laser ridges, it is ready to define the contact pads as the crossover blocks in Figure 127.

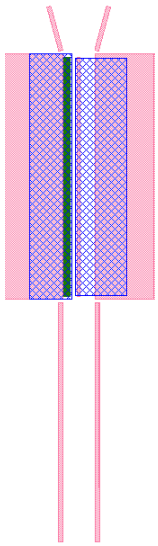

Figure 127. Mask 7 to deposit both p and n metals.

Since the alignment marks for Oracle group have to be metalized to improve their alignments on the silicon circuit side, the slash features shown in Figure 128 are the pattern is metalized.

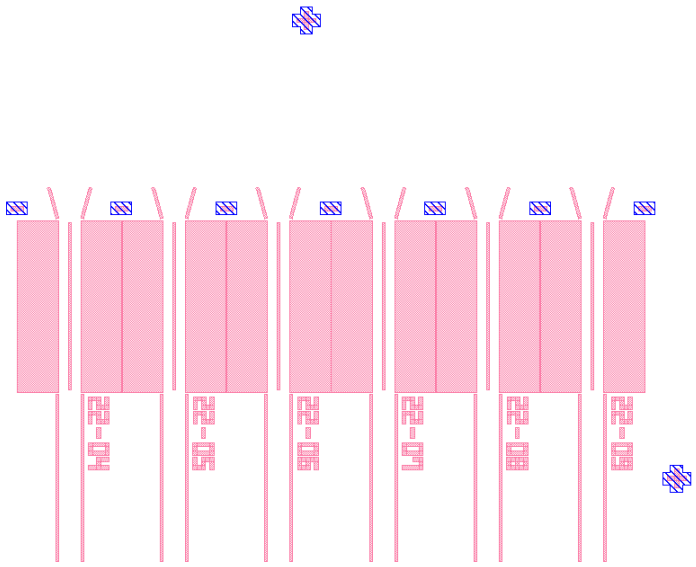

Figure 128. Mask 8 to metalize alignment marks.

The next mask level is to define the plating pads within both n and p contacts and electroplate several μm of Au on it as the orange blocks in Figure 129.

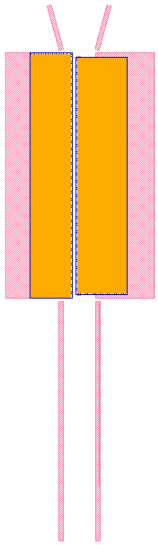

Figure 129. Mask 9 to electroplate Au on both p and n metals for contacts

The backside of outcoupler gratings is etched and deposited metals as reflectors to improve the upward coupling efficiency as shown in Figure 130.

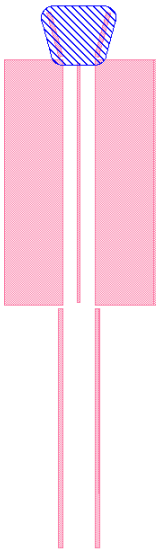

Figure 130. Mask 10 for the reflector on the back.

A2. Enhanced Coupling Strength Grating Patent

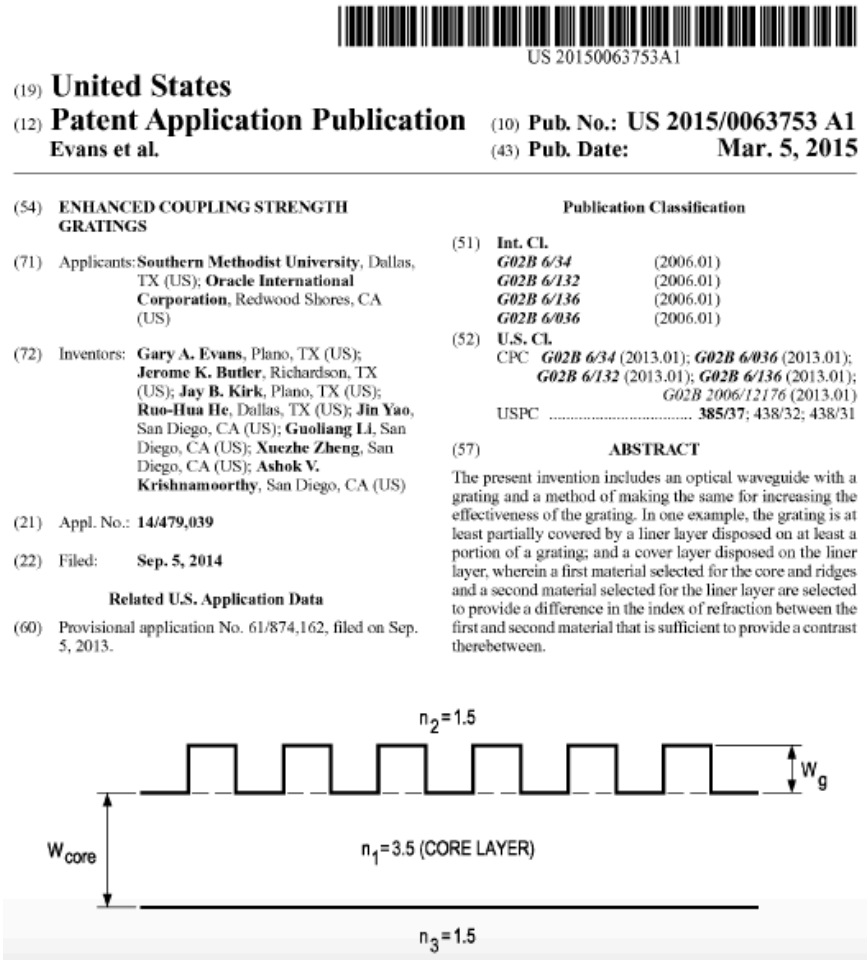

US 20150063753A1

(19) **United States**

(12) **Patent Application Publication**
Evans et al.

(10) **Pub. No.: US 2015/0063753 A1**
(43) **Pub. Date: Mar. 5, 2015**

(54) **ENHANCED COUPLING STRENGTH GRATINGS**

(71) Applicants: **Southern Methodist University**, Dallas, TX (US); **Oracle International Corporation**, Redwood Shores, CA (US)

(72) Inventors: **Gary A. Evans**, Plano, TX (US); **Jerome K. Butler**, Richardson, TX (US); **Jay B. Kirk**, Plano, TX (US); **Ruo-Hua He**, Dallas, TX (US); **Jin Yao**, San Diego, CA (US); **Guoliang Li**, San Diego, CA (US); **Xuezhe Zheng**, San Diego, CA (US); **Ashok V. Krishnamoorthy**, San Diego, CA (US)

(21) Appl. No.: **14/479,039**

(22) Filed: **Sep. 5, 2014**

Related U.S. Application Data

(60) Provisional application No. 61/874,162, filed on Sep. 5, 2013.

Publication Classification

(51) **Int. Cl.**

G02B 6/34	(2006.01)
G02B 6/132	(2006.01)
G02B 6/136	(2006.01)
G02B 6/036	(2006.01)

(52) **U.S. Cl.**
CPC ***G02B 6/34*** (2013.01); ***G02B 6/036*** (2013.01); ***G02B 6/132*** (2013.01); ***G02B 6/136*** (2013.01); *G02B 2006/12176* (2013.01)
USPC **385/37**; 438/32; 438/31

(57) **ABSTRACT**

The present invention includes an optical waveguide with a grating and a method of making the same for increasing the effectiveness of the grating. In one example, the grating is at least partially covered by a liner layer disposed on at least a portion of a grating; and a cover layer disposed on the liner layer, wherein a first material selected for the core and ridges and a second material selected for the liner layer are selected to provide a difference in the index of refraction between the first and second material that is sufficient to provide a contrast therebetween.

Figure 131. Cover page of enhanced coupling strength grating patent.

REFERENCES

[1] G. A. Evans, J. K. Butler, R.-H. He, J. B. Kirk, J. Yao, Z. Zheng and A. Krishnamoorthy, "Enhanced Coupling Strength Gratings for Couplers in III-V Compound Dielectric Waveguides," *Journal of Lightwave Technology,* vol. 35, no. 11, p. 2234, 2017.

[2] D. Taillaert, P. Bienstman and R. Baets, "Compact efficient broadband grating coupler for silicon-on-insulator waveguides," *Optics Letters,* vol. 29, no. 23, pp. 2749-2751, 1 Dec. 2004.

[3] B. G. Streetman and S. K. Banerjee, Solid State Electronic Devices, Pearson Education, Inc., 2005.

[4] R. Michalzik, VCSELs: Fundamental, Technology and Applications of Vertial-Cavity Surface-Emitting Lasers, Springer.

[5] S. Nakamura, "The Roles of Structural Imperfections in InGaN-Based Blue Light-Emitting Diodes and Laser Diodes," Science, 1998.

[6] G. Scamarcio, F. Capasso, C. Sirtori, J. Faist, A. L. Hutchinson, D. L. Sivco and A. Y. Cho, "High-Power Infrared (8-micrometer wavelength) superlattice lasers," Science, 1997.

[7] J. Faist, F. Capasso, D. L. Sivco, C. Sirtori, A. L. Hutchinson and A. Y. Cho, "Quantum Cascade Laser," Science, 1994.

[8] R. Q. Yang, C. J. Hill, K. Mansour, Y. Qiu, A. Soibel, R. E. Muller and P. M. Echternach, "Distributed Feedback Mid-IR Interband Cascade Lasers at Thermoelectric Cooler Temperatures," *IEEE Journal of Selected Topics in Quantum Electronics,* vol. 13, no. 5, p. 1074, 2007.

[9] E. Selcuk, Guided and deterministic self organization of quantum dots, Nano Letters, 2009.

[10] A. E. Siegman, Lasers, Sausalito, CA, USA: University Science Books, 1986.

[11] G. P. Agrawal and N. K. Dutta, Semiconductor Lasers, Norwell, Massachusetts, USA: Kluwer Academic, 2001.

[12] M. Eichhorn, Laser Physics, Springer, 2014.

[13] T. Numai, Fundamentals of Semiconductor Lasers, Springer, 2015.

[14] G. A. Evans and J. M. Hammer, Surface Emitting Semiconductor Lasers and Arrays, New York, NY, USA: Academic, 1993.

[15] H. Kressel and J. K. Butler, Semiconductor Lasers and Heterojunction LEDs, New York, NY, USA: Academic, 1977.

[16] I. Hayashi and M. B. Panish, "GaAs-Al(x)Ga(1-x)As Double Heterostructure Injection Lasers," *Journal of Applied Physics,* vol. 42, no. 150, 1971.

[17] K. S. Mobarhan, "Test and characterization of laser diodes: determination of principal parameters," Newport, Irvine, CA, USA.

[18] A. Yariv and P. Yeh, Photonics: Optical Electronics in Modern Communications, 6th ed., London, U.K.: Oxford Univ. Press, 2007.

[19] H. A. Haus, W. P. Huange, S. Kawakami and N. A. Whitaker, "Coupled Mode Theory of Optical Waveguides," *Journal of Lightwave Technology,* Vols. LT-5, pp. 16-23, 1987.

[20] J. Huang, K. Liu, J. Butler, N.-H. Sun and G. A. Evans, "First-Order Grating Coupling Coefficients in Asymmetric Three-Layer Waveguides for Transverse Electric Modes," *Journal of Lightwave Technology,* vol. 35, no. 11, p. 2200, 2017.

[21] L. A. Coldren and S. W. Corzine, Diode Lasers and Photonic Integrated Circuits, New York, NY, USA: Wiley, 1995.

[22] P. Monk, Finite Element Methods for Maxwell's Equations, Oxford University Press, 2003.

[23] G. Hadjicostas, J. Butler, G. A. Evans, N. W. Carlson and R. Amantea, "A Numerical Investigation of Wave Interactions in Dielectric Waveguides with Periodic Surface Corrugations," *IEEE Journal of Quantum Electronics,* vol. 26, no. 5, pp. 893-902, May 1990.

[24] J. K. Butler, N. H. Sun, G. A. Evans, L. Pang and P. Congdon, "Grating Assisted Coupling of Light Between Semiconductor and Glass Waveguides," *Journal of Lightwave Technology,* vol. 16, no. 6, pp. 1038-1048, June 1998.

[25] J. K. Butler, W. E. Ferguson, G. A. Evans, P. Stabile and A. Rosen, "A Boundary Element Technique Applied to the Analysis of Waveguides with Periodic Surface Corrugations," *IEEE Journal of Quantum Electronics,* vol. 28, no. 7, pp. 1701-1709, July 1992.

[26] J. E. Bowers and A. Y. Liu, "A Comparison of Four Approaches to Photonic Integration," *OSA,* 2017.

[27] J. E. Bowers and S. Srinivasan, "Optical Integration and Silicon Photonics," *J. Opt.,* vol. 18, pp. 31-32, 2016.

[28] G. Morthier and P. Vankwikelberge, Handbook of Distributed Feedback Laser Diodes, Artech House, Inc., 1997.

[29] C. Elachi, G. Evans and C. Yeh, "Transversely Bounded DFB Lasers," *JOSA,* vol. 65, no. 4, April 1975.

[30] M. Achtenhagen, N. V. Amarasinghe and G. A. Evans, "High-power distributed Bragg reflector lasers operating at 1065 nm," *IEEE Electron. Lett.,* vol. 43, no. 14, pp. 757-759, 5 Jul. 2007.

[31] T. Hiratani, D. Inoue, T. Tomiyasu, Y. Atsuji, K. Fukuda, T. Amemiya, N. Nishiyama and S. Arai, "Room-temperature continuous-wave operation of membrane distributed-reflector laser," *Appl. Phys. Express,* vol. 8, no. 11, p. Art. no. 112701, 2015.

[32] F. V. Laere, G. Roelkens, M. Ayre, J. Schrauwen, D. Taillaert, D. V. Thourhout, T. F. Krauss and R. Baets, "Compact and Highly Efficient Grating Couplers Between Optical Fiber and Nanophotonic Waveguides," *Journal of Lightwave Technology,* vol. 25, no. 1, p. 151, 2007.

[33] "INNOVA FreD," Coherent, [Online]. Available: https://www.coherent.com/lasers/laser/ion-lasers/innova-fred.

[34] S. R. Selmic, G. A. Evans, T. M. Chou, J. B. Kirk, J. N. Walpole, J. P. Donnelly, C. T. Harris and L. J. Missaggia, "Single frequency 1550-nm AlGaInAs-InP tapered high-power laser with a distributed bragg reflector," *IEEE Photon. Technol. Lett.,* vol. 14, no. 7, pp. 890-892, Jul. 2002.

[35] "WAVEGUIDE program," SMU Photonics Group, [Online]. Available: http://lyle.smu.edu/ee/smuphotonics/.

[36] A. Taflove and S. Hagness, Computational Electrodynamics: The Finite-Difference Time-Domain Method, 3rd edition ed., Boston, MA: Artech House, 2005.

[37] D. Taillaert, W. Bogaerts, P. Bienstman, T. F. Krauss and R. Baets, *IEEE J. Quantum Electron.,* vol. 38, no. 949, 2002.

[38] P. Bienstman and R. Baets, *Opt. Quantum Electron. ,* vol. 33, no. 327, 2001.

[39] R. H. Johnson and G. A. Evans, "Temperature Insensitive Integrated Electro-Absorption Modulator and Laser". United States Patent 9762025, 12 September 2016.

[40] G. A. Evans, J. K. Butler, J. B. Kirk, R.-H. He, J. Yao, G. Li, X. Zheng and A. V. Krishnamoorthy, "Enhanced Coupling Strength of Gratings". United States Patent 38453, 5 September 2013.

[41] J. Piprek, Y.-J. Chiu, S.-Z. Zhang, J. E. Bowers, C. Prott and H. Hillmer, "High-Efficiency MQW Electroabsorption Modulators," *Electrochemical Society,* Vols. 2002-4, pp. 139-149, 2002.